SINGLE MOLECULE STUDIES OF NUCLEOSOME INHERITANCE

A Dissertation

Presented to the Faculty of the Graduate School

of Cornell University

In Partial Fulfillment of the Requirements for the Degree of

Doctor of Philosophy

by

Lucy Donato Brennan

August 2017

SINGLE MOLECULE STUDIES OF EPIGENETIC INHERITANCE

Lucy Donato Brennan, Ph. D.

Cornell University 2017

Eukaryotic gene expression is tightly coupled to the spatial organization and modification of nucleosomes. During DNA replication, parental nucleosomes are partitioned approximately equally between the nascent DNA strands where they serve as a template for modification of nascent histones. Replication fork progression is tightly coupled to the deposition of nascent histones behind the replication fork, however the deposition of parental nucleosomes is poorly understood. Reconstitution of eukaryotic replication will be essential to dissecting the underlying mechanisms responsible for the coordination of replication and re-chromatinization of the genome. Pairing *in vitro* approaches with single-cell manipulation has the potential to contextualize the *in vitro* findings with in the complexities of the cellular environment. Here I present three distinct projects that lay the foundation towards the goal of ascertaining the fundamental mechanisms the drive chromatin replication and epigenetic inheritance. First is the characterization of the a passive-nucleosome transfer mechanism in the context of a simplified replication system. Second, the preliminary experiments aimed at characterizing the eukaryotic replicative helicase and reconstituting the eukaryotic replisome. Finally, a single-cell injection technique used to study asymmetric cell division in the *C. elegans* embryo.

BIOGRAPHICAL SKETCH

Lucy Brennan was born on February 7th, 1989 in Corvallis, Oregon to Tom and Geralyn Brennan. She has a younger brother, Jack Brennan who is pursuing a career in plant breeding and genetics. Lucy completed her Bachelors of Science at University of California, Santa Cruz in 2011 with a degree in molecular, cellular, and developmental biology and a minor in physics. She was mentored as an undergraduate by Professor John Tampkun at UCSC and during the summer by Professor Joe Beckman at Oregon State University. Her undergraduate research at UCSC focused on the functionality of the ATP-dependent chromatin remodeler *Brahma* (BRM) in drosophila melanogaster utilizing RNA interference to probe the interactions between the BRM protein and the ISWI chromatin remodeler. At OSU, Lucy participated in an HHMI undergraduate summer research program where she studied the progression of Lou Gherig's disease in a mouse model. Since entering Cornell, Lucy has participated in several educational outreach programs, most notably the Cornell Prison Education Program. For the past six years she has dedicated the vast majority of her time to single molecule studies of DNA replication and epigenetic inheritance in Michelle Wang's lab. Outside of the lab, Lucy has run a small ceramics studio for undergraduates on the Cornell campus.

For Weston

ACKNOWLEDGMENTS

Thank you to my dear friend Hannah Ratner for being a pillar of support and love. And to my family for instilling resilience and confidence in me since I was a child.

I have had several excellent mentors through-out my education, most notably Professor John Tamkun my undergraduate advisor and mentor. I would not be the researcher that I am without his encouragement both in and outside of the lab. I hope to one day emulate his commitment to research, teaching, and most importantly mentoring.

Thank you to the Wang lab for being my home for the last six years.
Thanks especially to James, Bob, and Bo for teaching me the ins and outs of optical trapping and showing me endless patience and willingness to explain to me even the most technical details of an instrument or experiment. A huge thanks to the rest of the lab for being supportive, critical, motivational, and everything one could hope for in lab mates.

And finally, thank you to Michelle Wang for being a pillar of motivation and for pushing me well outside of my comfort zone, driving my growth as a researcher and individual.

TABLE OF CONTENTS

LIST OF FIGURES

LIST OF TABLES

CHAPTER 1

CHROMATIN DYNAMICS DURING DNA REPLICATION

Chromatin organization along the genome

The positioning and modification state of nucleosomes regulates both the accessibility of the DNA, the recruitment of transcription factors, and the higher order organization of the genome[1,2]. Maintenance of the chromatin landscape is critical for preserving cellular identity and function. At the same time, dynamic changes to chromatin domains are known to occur during cellular differentiation[3], thus indicating the need for flexibility within epigenetic inheritance pathways. Defects in epigenetic maintenance have been linked to numerous diseases including heart disease, arthritis, Alzheimer's disease, and cancer[4,5]. This underscores the fine line that these processes must walk between establishing and maintaining proper cellular function or driving cellular toxicity and oncogenesis. A careful balance between de novo formation of new chromatin domains and maintenance of those domains must be struck within a cell to mediate cellular differentiation and maintenance of proper function while still enabling cellular responses to changing environmental conditions.

The eukaryotic genome is highly organized to fit into the nucleus and yet remain accessible for gene transcription and DNA repair. In general, there are two types of chromatin: euchromatin and heterochromatin, which were first

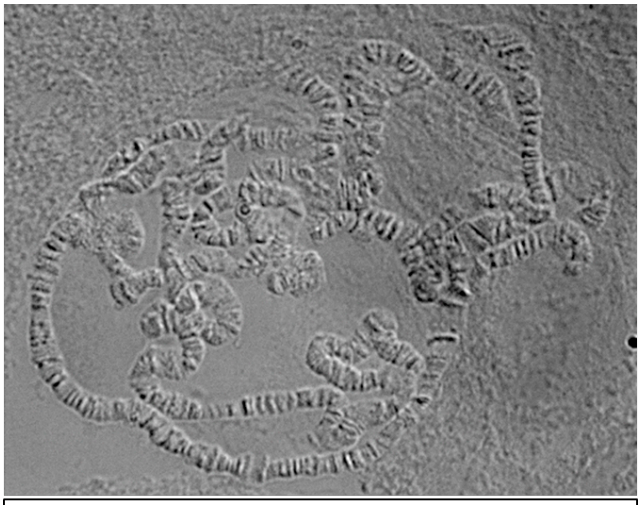

Figure 1.1 *Drosophila* polytene chromosome spread. Dark bands are heterochromatic regions, lighter bands between the dark bands are euchromatin.

characterized through cytological analysis of chromosomes (Figure 1.1)[6-8]. Heterochromatin was characterized as the very dense and intensely stained regions that appeared in karyotypes and chromosome spreads. Euchromatin was observed as lightly stained and open chromatin. Analysis of immunostained chromosome spreads in conjunction with genome-wide chromatin immunoprecipitation studies showed that active transcription occurred in euchromatic regions where as heterochromatin was generally transcriptionally silent[7]. Each region contains histone modifications that are at least partially used to differentiate each domain[1]. Heterochromatin is generally marked by H3K27 and K3K9 methylation and an absence of acetylation. Methyl marks have been shown to directly recruit protein complexes, such as Polycomb-repressive complexes and HP1, which act as a scaffold for further compaction and organization. Euchromatic regions are much more dynamic and fluid in their histone modification code, but in general enhancers tend to have H3K4 methylation and the gene body is marked with H3K36 methylation and various acetylation marks. These marks participate in the recruitment of transcription machinery and chromatin remodelers that facilitate active gene transcription.

There are two major events that participate in defining the chromatin landscape within the cell; transcription and replication. The transcriptional activity of a gene helps to mediate the formation of nucleosome depleted regions and formation of a more accessible chromatin state at actively expressed genes[9]. Conversely, the formation of heterochromatin in intergeneic regions or actively repressed genes is equally important for genome organization and suppression of aberrant transcription[10-12]. Although less is

known about the initial formation of hetrochromatin domains, their maintenance is thought be controlled through the binding of repressive complexes that act to exclude transcription machinery from accessing the underlying DNA[13]. The feedback mechanisms between histone chaperone, remodelers, and modifiers and the transcription machinery has been extensively reviewed[14-16]. In general it is thought that transcription plays a primary role in the establishment and reinforcement of active chromatin domains, where the major changes to chromatin structure are specific to enhancer and promoter regions along the genome.

Interestingly, the replication landscape is correlated with the transcriptional landscape, both spatially and temporally (Figure 1.2). Replication origins are more abundant in euchromatic regions and are preferentially found at gene regulatory regions where nucleosome occupancy is low [17-21]. These origins have also been characterized as early-replicating and tend to progress quickly along the DNA[20,22-24]. Within heterochromatic regions, replication origins are few and far-between and tend to initiate late in S-phase[18,20,25]. Characterization of replication passage through heterochromatic regions shows a slower progression rate and in extreme cases a higher propensity for replication fork stalling and collapse[25-27]. These global characteristics of DNA replication indicate a direct relationship between chromatin organization and DNA replications and allude to the possibility for differential replisome progression depending on the local chromatin environment[21].

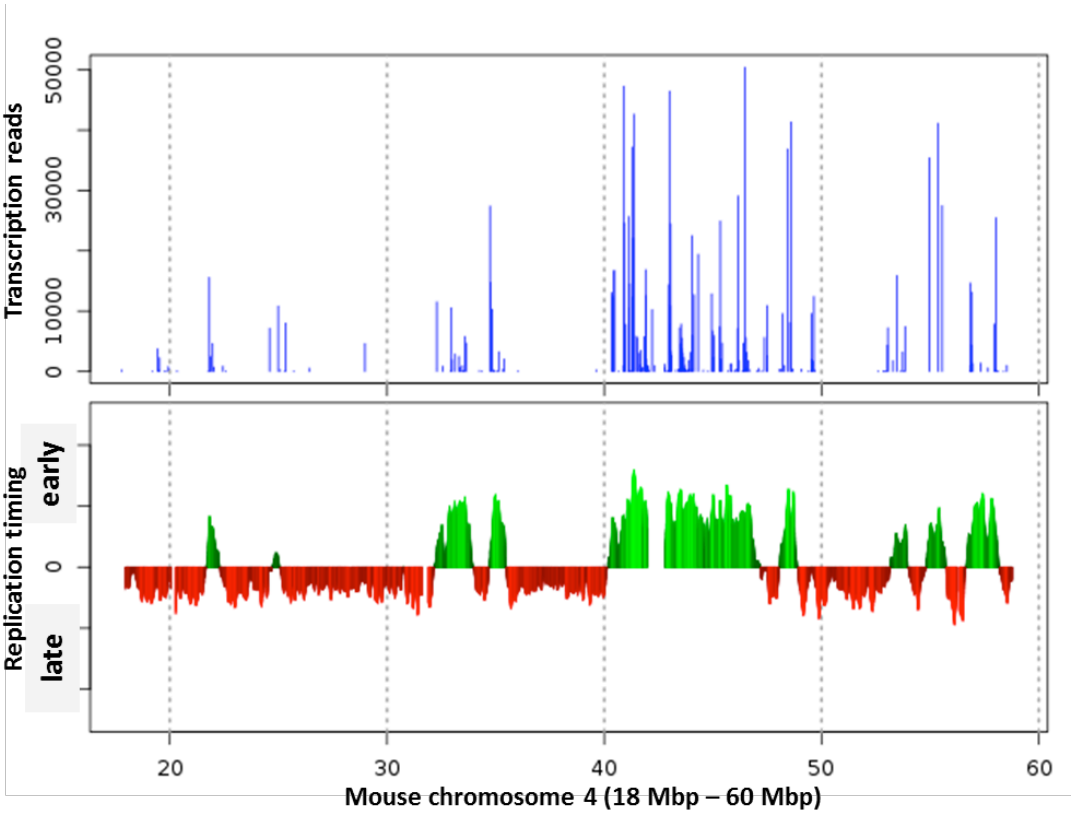

Figure 1.2 An example from genome-wide ChIP studies showing transcriptional reads (top, ref. 23) and replication timing (bottom, ref. 24) from mouse chromosome 4. Data visualized on www.replicationdomain.com created by David Gilbert's lab at Florida State University.

Regardless of chromatin environment, the replication machinery must gain access to the underlying DNA in order to duplicate the genome, which requires the splitting the parental DNA and the subsequent copying of each strand to yield two daughter chromosomes. Therefore the replication process is considered far more disruptive, than transcription, and conducive for genome-wide resetting of chromatin domains. How cells maintain their identity through many cell cycles is thus at odds with a complete reset to the epigenetic landscape. Modified nucleosomes that mediate downstream protein recruitment and chromatin organization have been shown to be

maintained in the vicinity of their original position through several rounds of cell division[28,29]. In this way the parental histone modifications can act to nucleate the reformation of the proper local chromatin environment through the recruitment of histone modifying enzymes[29-32]. Early experiments on nucleosome (or Nu-body) segregation during S-phase relied on sedimentation analysis of heavy-isotope labelled histones incorporated through only one round of DNA replication. From these studies it was immediately clear that nucleosomes were dispersed approximately evenly between the two daughter strands, in what was described as a random distribution of nucleosomes occurring the rapidly behind the progressing replication fork[33-37]. Attempts to determine if parental and nascent histones were organized in an alternating manner using the same isotope-labelling method were inconclusive but definitely indicated that new and old histones were intermingled along the DNA[34,36,37].

These early experiments provided a solid foundation upon which further study has been built and have been further validated by recent work utilizing more sophisticated assays. However, the question still remains: how are parental histones transferred to the daughter DNA during S-phase in such a way that they can facilitate the reestablishment of properly positioned chromatin domains along the genome? What possible mechanisms underlie parental nucleosome inheritance? The rest of this chapter will focus on recent work aiming to address these outstanding questions and the final chapter will provide a brief perspective of the field novel outstanding questions within it.

Chaperoning histones at the replication fork

The current mechanism for parental histone inheritance depends on the action of many different histone chaperones and remodelers working at the replication fork to simultaneously deposit nascent and parental histones[38,39]. Immediately in front of the replisome, histone chaperones may play a role in destabilizing the nucleosome through the removal of H2A-H2B dimers[40,41]. Positive supercoiling generated by the replisome may also play a role in nucleosome destabilization and perhaps mediate histone-chaperone interactions[40,42]. The freed histones are then shuttled from their position ahead of the fork to a new position along the nascent DNA. How and through what intermediates the parental histones are transferred remains an open-ended question. Once the histones are deposited on the newly synthesized DNA chromatin remodelers properly space the nucleosome with respect to neighboring bound proteins and histone modifying enzymes are recruited to reinstate domains of modifications on the nascent histones[29,43]. Concurrent with the transfer of parental nucleosomes is the deposition of nascent histones, which are marked by extensive H3 and H4 acetylation[44,45]. Nascent histone deposition is primarily driven by the histone chaperones Asf1 and Caf1, which are also proposed to mediate parental histone transfer[46-51]. How these two pathways are coordinated and whether they are differentiable is an active area of inquiry in the field. To address these questions, investigators sought to identify histone chaperones and remodelers that interact with components of the replisome and to characterize the histone content of nucleosomes deposited on the nascent DNA.

Determining the extent to which the parental histones intermingle with nascent

histones following replication fork passage, can clarify the fundamental unit of nucleosome inheritance and provide intuition regarding which histone chaperones may mediate the transfer of that heritable unit. By differentially labelling parental and nascent histones, either through heavy isotope incorporation or epitope tags, the histone composition of nucleosome on nascent DNA can be determined. From such experiments, it has been shown that the H3/H4 tetramer is composed of either parental histones or nascent histones but rarely both[52-55]. In contrast, old and new H2A and H2B were found at approximately a 1:1 ratio within nucleosome following S-phase[55]. These data indicate that H2A/H2B dimers are more labile whereas the H3/H4 tetrasome remains intact thus defining tetrasome as the heritable unit. Although there is a hint that H2B ubiquitylation has been linked to regions of active gene expression and may be linked to replication dynamics[56], the mechanism for H2A/H2B inheritance is very poorly characterized perhaps because these histones are much more dynamic, making any sort of tracking studies exceedingly difficult. The primary focus of nucleosome inheritance has been on H3/H4 chaperones at the replication fork because these histones not only contain the bulk of histone modifications but also are considered the heritable unit. Extensive analysis of histone chaperones that act in a replication-dependent manner have focused on three primary candidates; FACT, Asf-1, and Caf-1. Each of these complexes has been found to associate with component of the replication machinery making them logical intermediates for transferring parental histones (Figure 1.3).

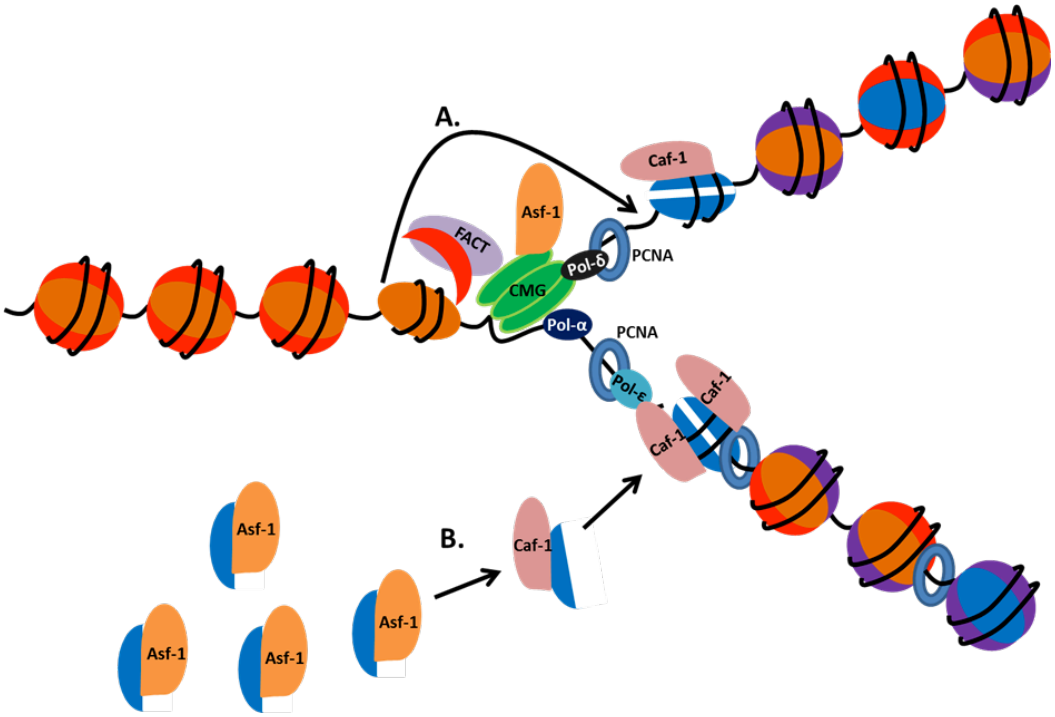

Figure 1.3 General summary of potential histone deposition and transfer at the replication fork. **(A)** Transfer of parental H3/H4 dimers (orange) from ahead of the fork to the nascent DNA behind via an unknown pathway, possibily through an Asf-1/ Mcm2 bound intermediate. FACT may act at the fork to remove or capture parental H2A/H2B dimers (red) **(B)** Nascent histones (H3/H4-blue, H2A/H2B-purple) travel through a chaperone pathway, primarily through Asf-1 to Caf-1 and then deposition on the nascent DNA.

The FACT complex was first characterized in the context of transcription[57] where it Facilitaes Chromatin Transcription via its ability to evict H2A-H2B dimers and loosen histone-DNA interactions for easier polymerase transit. The FACT complex was shown to associate with both Mcm-4[41], RPA[58], and polymerase- alpha[59]. Such interactions as well as further in vitro work have placed FACT at the replication fork where it has been found to mediate replication origin reorganization and initiation and as well as modulate replisome speed[41,60-62]. Conditional knockout of the SSRP1 subunit of the FACT complex resulted in a slow progression through S-phase but had no

impact on nucleosome reassembly on the nascent DNA[62]. In purified systems FACT stimulated helicase unwinding of nucleosomal DNA[41] as well as full replication of chromatin substrates[60,61]. These results may be consistent with the biochemical function of FACT as a H2A/H2B chaperone, although it is also capable of binding to H3/H4 histones; whether it does so at the replication fork is unknown[63]. The current understanding is that FACT acts to help loosen nucleosome structure ahead of the replisome by interacting with the H2A/H2B dimer, staying in the immediate vicinity of the fork through its interactions with the Mcm helicase and pol-a (Figure 1.3). This loosening of the histones ahead of the replication fork would help expedite replisome passage and displacement of the H3/H4 tetramer, perhaps through some other mechanism.

The histone chaperone Caf-1 has been shown to play a major role in replication progression and chromatin reformation on the nascent DNA; initially through fractionation of cell extracts and biochemical analysis of the ability of these fractions to assemble chromatin[64-66]. In vivo analysis of the role for Caf-1 during S-phase show that depletion of Caf-1 slows progression through S-phase but does not completely inhibit the replication process[47]. Furthermore, Caf-1 depletion leads to a measurable, although not complete, derepression of silent chromatin indicating that histone modifications can be inherited in the absence of Caf-1 but recruitment of histone modifying enzymes is inhibitited thus limiting the reestablishment of complete silencing[67,68]. Biochemical analysis indicates that two Caf1 proteins are required for the deposition of a H3/H4 tetramer, as Caf1 has been shown to preferentially bind

H3/H4 dimers rather than tetramer, and the subsequent association of two Caf-1-H3-H4 complexes with DNA drives the formation of a H3/H4 tetramer[50,69]. Fluorescent localization studies have placed Caf-1 at replication forks in vivo most likely mediated through the interaction of Caf-1 and PCNA[70-72]. Such localization places Caf-1 at an optimal position to act as in intermediate for H3/H4 deposition (Figure 1.3). In vivo studies have postulated a histone transfer mechanism where displaced H3/H4 subunits are captured by Caf1. However, the binding stoichiometry of Caf-1 to H3/H4 is at odds with the in vivo data indicating that the H3/H4 tetramer is inherited as a unit through S-phase, a crucial aspect that has yet to be reconciled with the biochemical data.

However, Caf-1 dimerization to facilitate the formation of an H3/H4 tetramer is likely an essential aspect of nascent histone deposition, a process that converges with parental histone transfer along the daughter DNA strands (Figure 1.3). During S-phase histones are rapidly overexpressed in preparation for the doubling of the DNA content in the cell[73]. These histones are sequestered by histone chaperones, primarily Asf1, presumably to prevent their random deposition on to the nascent DNA[51]. Asf1 plays a major role in controlling the deposition of nascent histones from the nucleoplasm by assembling a H3/H4 dimer, then passing it to Caf1 for deposition[74,75]. The localization of Asf-1 to the replication fork, through interactions with the CMG helicase and the clamp-loader RFC, make Asf-1 an attractive candidate for parental histone transfer[49,76-78], although the majority of the biochemical data point to Asf-1 primarily mediating nascent histone deposition (Figure 1.3). The interaction between Asf-1 and H3/H4

occludes the dimer interface of the H3/H4 tetramer and Asf-1 has been shown to have tetrasome splitting activity[79]; an activity at odds with the inheritance of an intact H3/H4 tetramer. Although there is some evidence that Asf-1 can be isolated in a complex with parental H3/H4 histones, but only under conditions of replicative stress perhaps alluding to the primary function of Asf-1 as acting as a reservoir for free histones[49]. In vivo studies in yeast lacking Asf1, or greatly overexpressing the histones, found that the replisome has a higher propensity for stalling under these conditions[49]. Stalling of the replisome suggests that the chromatin ahead of the fork has become an insurmountable barrier for the helicase, which lead the investigators to postulate that Asf1 plays a direct role in disrupting nucleosomes ahead of the fork. Thus, when Asf1 is lacking or completely saturated with nascent histones, it is unable to aid in parental nucleosome eviction. However, an alternative interpretation is possible in which it is not the disruption of the nucleosomes ahead of the fork that facilitates replisome progression but rather the deposition of nucleosome behind the fork. Perhaps when the nascent DNA is saturated with histones in an uncontrolled manner, the parental histones ahead of the fork cannot be transferred and therefore remain stably bound to the DNA thus becoming a significant barrier for the replicative helicase.

Coordination of nucleosome deposition with replication fork progression

It is clear that the replisome is sensitive to the surrounding chromatin environment indicating a direct coordination between replication fork progression and chromatin dynamics. The requirement of histone chaperones at the replication fork indicates that

the replisome acts as a central hub for chromatin disruption and formation. For the replication fork to proceed forward the transfer of parental nucleosome must be coordinated with the synthesis for nascent DNA and the deposition of nascent histones from a soluble pool. The coordination of DNA synthesis, nucleosome transfer, and histone deposition have been alluded to through in vivo analysis of replisome speed in the absence of histone chaperones[47,49,62] and the general observation that replication proceeds more slowly through regions of dense chromatin[17]. The specific manner of coordination at the replication fork remains to be determined although specific aspects of replication fork organization have been elucidated, providing insight into possible pathways for generating said organization.

Attempts to elucidate the transfer mechanism for parental histones started with the careful examination of replication fork organization. Ahead of the replication fork approximately 300 bp of naked DNA was observed and there is indication that the nucleosome immediately ahead of the fork is destabilized possibly by FACT or by supercoiling generated by the replisome generated[40,80]. These observations suggest a mechanism for parental histone transfer that acts at a distance from the fork, independent of physical interaction between the replisome and histones. Behind the replication fork, there is a region of naked DNA between 200 and 600 bp in length[40,80-82]. In vitro reconstitution of DNA replication utilizing whole cell extracts or purified bacteriophage replisomes provided further evidence that histones are efficiently inherited during DNA replication and seemed to indicate that the replisome may come into direct contact with the nucleosome ahead of the fork[83,84]. The simplified

replisomes used to reconstitute nucleosome inheritance in vitro indicated that this process does not necessarily rely on the complex mélange of proteins present within the cell. Most notable, results from both of these systems indicated that the nucleosomes may undergo a direct transfer mechanism where the parental nucleosomes remained associated with DNA through replication fork passage[83,84].

Almost all of the studies to date indicate that generation of sufficient nascent DNA on both daughter strands is an essential component for the reformation of chromatin behind the replication fork[40,49,80,82,83]. Due to the anti-parallel nature of DNA, each daughter strand undergoes differential synthesis reactions where the leading strand is synthesized continuously and the lagging strand is generated in short Okazaki fragments[85]. The asymmetry in DNA synthesis prompts consideration for differential segregation of histones, possibly mediated by both DNA synthesis and a strand specific recruitment of histone chaperones via interaction with the DNA polymerases or processivity

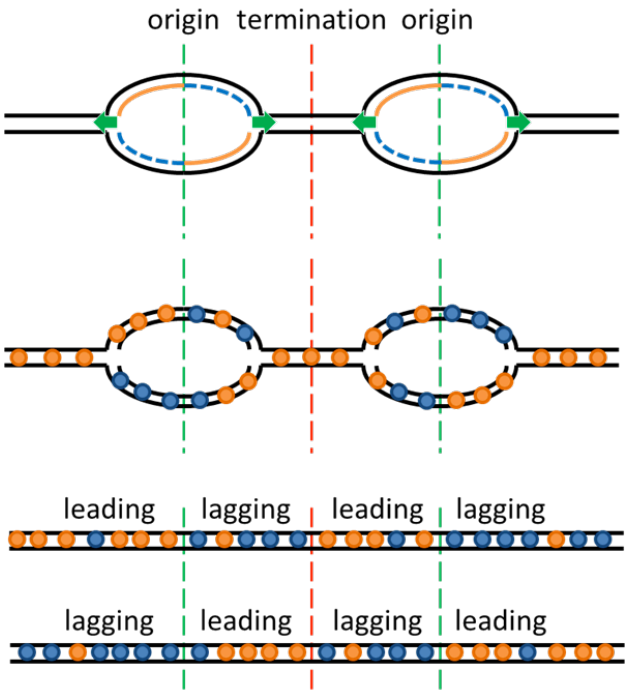

Figure 1.4 Schematic of the nucleosome landscape following replication, assuming there is a bias of parental nucleosomes (orange circles) to the leading strand (orange line, top panel) which would then drive nascent histones (blue circles) to the lagging strand (blue dotted line, top panel).

factors (Figure 1.4). For example, PCNA, RFC, pol-alpha and RPA are all replication proteins that are enriched on the lagging strand and also known to interact with Asf-1, Caf-1 and FACT[58,59,71,72,76,86]. On the leading strand, perhaps the continuous synthesis of DNA provides ample room for deposition of histones and minimal conflicts with DNA processing machinery found almost exclusively along the lagging strand.

Although strand specific nucleosome content has not been carefully examined to date, studies on Okazaki fragment synthesis in yeast have produced data suggesting that nucleosome spacing behind the replication fork can directly impact Okazaki fragment length[87]. In yeast depleted of ligase1 unligated Okazaki fragment lengths were found to strongly correlate with nucleosome repeat length across the genome[87]. Combining paired-end sequencing with the purification of unligated Okazaki fragment lengths, subtle changes to fragment length with respect to nucleosome depleted regions or depletion of histone chaperones and remodelers could be monitored[43,87]. Caf-1 depletion resulted in the loss in correlation between nucleosome repeat Okazaki fragment lengths providing a direct measure of nucleosome organization along the lagging strand[43]. Interestingly in this study, depletion of Asf-1 had little effect on Okazaki fragment size, indicating that Caf-1 is the major factor dictating nucleosome spacing. Following the deposition of histones along the nascent DNA, chromatin remodelers fine-tune their spacing possibly facilitating further deposition by making space behind the replication fork. To this end, the deletion of both the Isw1 and Cdh1 remodelers completely abolished nucleosome-correlated Okazaki fragment periodicity[43]. However, the positioning of nucleosomes around a transcription factor

binding site was only slightly perturbed in the *isw1/chd1* deletion indicating that the binding of a transcription factor could act to drive nucleosome phasing even in the absence of remodelers. Furthermore, the nucleosome immediately surrounding a transcription factor binding site were still positioned properly when Caf-1 was deleted although the periodicity quickly decayed outside of the +2 nucleosome [43]. This alludes to a chaperone and remodeler free mechanism for nucleosome deposition that is significantly impacted by transcription factor re-binding[88,89] to the nascent DNA in concert with sequence specific nucleosome association[90,91]. In this case, Caf-1 may help to control the deposition of nucleosomes in an ordered manner behind the replication fork where nucleosome remodelers then fine-tune their position in to a well ordered array, however the initial transfer of parental nucleosomes and deposition of nascent histones can proceed independently of these chaperones.

A chaperone-independent pathway for nucleosome transfer and deposition is clearly possible, although the relatively disordered arrangement of the placed nucleosomes would slow DNA replication possibly by saturating the DNA immediately behind the replication fork or by competing with replication proteins for access to the nascent DNA. Theoretical studies support this sort of model, where a "replication-guided" nucleosome deposition pathway would result in a more disordered chromatin structure[92]. Furthermore, recent studies of in vitro chromatin replication reconstituted with only purified proteins showed that chromatin chaperones and remodelers were dispensable for complete replication and reformation of chromatin behind the fork[60,61]. Only the FACT complex has an appreciable impact on replication fork progression,

where it was necessary to attain in vivo replication rates along a chromatin template. Reactions in the absence of FACT managed to completely replication through a chromatin template albeit at a slightly slower rate[60], consistent with the model where FACT primarily facilitates the loosening of histone-DNA interactions ahead of the fork rather than assisting in the deposition of histones along the nascent DNA.

Current mechanistic models for nucleosome inheritance rely on histone chaperones to collect the tetrasome core that is displaced ahead of the fork and shuttle it to the nascent DNA behind the fork. However, there is abundant data suggesting the existence of a chaperone-independent pathway for nucleosome transfer and deposition. The chaperoning of nascent histones from the cytosol to the nascent DNA is a clearly defined pathway for nascent histone deposition but the extent to which that pathway converges with parental histone transfer is unclear. Parental histones are found approximately 400 bp from their original positions[14], thus maintaining the overall spatial template for histone modification domains. Histone chaperones, in conjunction with remodelers, most likely coordinate to maintain a nucleosome free region of DNA behind the replication fork and to fine-tune nucleosome spacing along the nascent DNA. The mechanism underlying a chaperone-independent nucleosome transfer model would be difficult to elucidate in vivo, however the outcome of such a mechanism can be hypothesized based on previous observational studies. Competition between nascent histone deposition and paternal histone transfer would dictate how nucleosomes are partitioned between the two strands and could potentially be predicted via the kinetics of each of the enzymes involved. Such a mechanism would

be extremely sensitive to chaperone and nascent histone concentrations as well as replication fork speed and chromatin environment, as has been shown previously.

Each of the following chapters contains distinct projects undertaken in Michelle Wang's lab. First, the single molecule study of nucleosome inheritance during DNA replication. Second, the preliminary single molecule studies on the eukaryotic replisome are summarized. Third, single-cell injections of *C. elegans* embryos is shown to be a viable single-cell manipulation technique and used to study the initial polarization of the *C. elegans* embryo.

REFERENCES

1. Bannister, A.J. & Kouzarides, T. Regulation of chromatin by histone modifications. *Cell Res* **21**, 381-95 (2011).
2. Kouzarides, T. Chromatin modifications and their function. *Cell* **128**, 693-705 (2007).
3. Li, X.Y., Harrison, M.M., Villalta, J.E., Kaplan, T. & Eisen, M.B. Establishment of regions of genomic activity during the Drosophila maternal to zygotic transition. *Elife* **3**(2014).
4. Portela, A. & Esteller, M. Epigenetic modifications and human disease. *Nat Biotechnol* **28**, 1057-68 (2010).
5. Wang, G.G., Allis, C.D. & Chi, P. Chromatin remodeling and cancer, Part I: Covalent histone modifications. *Trends Mol Med* **13**, 363-72 (2007).
6. Allis, C.D. & Jenuwein, T. The molecular hallmarks of epigenetic control. *Nat Rev Genet* **17**, 487-500 (2016).
7. Wang, J., Jia, S.T. & Jia, S. New Insights into the Regulation of Heterochromatin. *Trends Genet* **32**, 284-94 (2016).
8. Brown, S.W. Heterochromatin. *Science* **151**, 417-25 (1966).
9. Jiang, C. & Pugh, B.F. Nucleosome positioning and gene regulation: advances through genomics. *Nat Rev Genet* **10**, 161-72 (2009).
10. Boivin, A. & Dura, J.M. In vivo chromatin accessibility correlates with gene silencing in Drosophila. *Genetics* **150**, 1539-49 (1998).
11. Whitehouse, I., Rando, O.J., Delrow, J. & Tsukiyama, T. Chromatin remodelling at promoters suppresses antisense transcription. *Nature* **450**, 1031-5 (2007).
12. Hiragami-Hamada, K. et al. The molecular basis for stability of heterochromatin-mediated silencing in mammals. *Epigenetics Chromatin* **2**, 14 (2009).
13. Horn, P.J. & Peterson, C.L. Heterochromatin assembly: a new twist on an old model. *Chromosome Res* **14**, 83-94 (2006).
14. Radman-Livaja, M. & Rando, O.J. Nucleosome positioning: how is it established, and why does it matter? *Dev Biol* **339**, 258-66 (2010).
15. Venkatesh, S. & Workman, J.L. Histone exchange, chromatin structure and the regulation of transcription. *Nat Rev Mol Cell Biol* **16**, 178-89 (2015).
16. Henikoff, S. Nucleosome destabilization in the epigenetic regulation of gene expression. *Nat Rev Genet* **9**, 15-26 (2008).
17. Soriano, I., Morafraile, E.C., Vazquez, E., Antequera, F. & Segurado, M. Different nucleosomal architectures at early and late replicating origins in Saccharomyces cerevisiae. *BMC Genomics* **15**, 791 (2014).
18. Pope, B.D. et al. Topologically associating domains are stable units of replication-timing regulation. *Nature* **515**, 402-5 (2014).
19. Pourkarimi, E., Bellush, J.M. & Whitehouse, I. Spatiotemporal coupling and decoupling of gene transcription with DNA replication origins during embryogenesis in C. elegans. *Elife* **5**(2016).

20. Hansen, R.S. et al. Sequencing newly replicated DNA reveals widespread plasticity in human replication timing. *Proc Natl Acad Sci U S A* **107**, 139-44 (2010).
21. Cadoret, J.C. et al. Genome-wide studies highlight indirect links between human replication origins and gene regulation. *Proc Natl Acad Sci U S A* **105**, 15837-42 (2008).
22. Conti, C. et al. Replication fork velocities at adjacent replication origins are coordinately modified during DNA replication in human cells. *Mol Biol Cell* **18**, 3059-67 (2007).
23. Hiratani, I. et al. Genome-wide dynamics of replication timing revealed by in vitro models of mouse embryogenesis. *Genome Res* **20**, 155-69 (2010).
24. Takebayashi, S. et al. Murine esBAF chromatin remodeling complex subunits BAF250a and Brg1 are necessary to maintain and reprogram pluripotency-specific replication timing of select replication domains. *Epigenetics Chromatin* **6**, 42 (2013).
25. Su, T.T. Heterochromatin replication: better late than ever. *Curr Biol* **20**, R1018-20 (2010).
26. Donley, N. & Thayer, M.J. DNA replication timing, genome stability and cancer: late and/or delayed DNA replication timing is associated with increased genomic instability. *Semin Cancer Biol* **23**, 80-9 (2013).
27. De, S. & Michor, F. DNA replication timing and long-range DNA interactions predict mutational landscapes of cancer genomes. *Nat Biotechnol* **29**, 1103-8 (2011).
28. Gaydos, L.J., Wang, W. & Strome, S. Gene repression. H3K27me and PRC2 transmit a memory of repression across generations and during development. *Science* **345**, 1515-8 (2014).
29. Alabert, C. et al. Two distinct modes for propagation of histone PTMs across the cell cycle. *Genes Dev* **29**, 585-90 (2015).
30. Aagaard, L. et al. Functional mammalian homologues of the Drosophila PEV-modifier Su(var)3-9 encode centromere-associated proteins which complex with the heterochromatin component M31. *EMBO J* **18**, 1923-38 (1999).
31. Hansen, K.H. et al. A model for transmission of the H3K27me3 epigenetic mark. *Nat Cell Biol* **10**, 1291-300 (2008).
32. Margueron, R. et al. Role of the polycomb protein EED in the propagation of repressive histone marks. *Nature* **461**, 762-7 (2009).
33. Weintraub, H. Cooperative alignment of nu bodies during chromosome replication in the presence of cycloheximide. *Cell* **9**, 419-22 (1976).
34. Seale, R.L. Studies on the mode of segregation of histone nu bodies during replication in HeLa cells. *Cell* **9**, 423-9 (1976).
35. Jackson, V., Granner, D.K. & Chalkley, R. Deposition of histones onto replicating chromosomes. *Proc Natl Acad Sci U S A* **72**, 4440-4 (1975).
36. Annunziato, A.T. The Fork in the Road: Histone Partitioning During DNA Replication. *Genes (Basel)* **6**, 353-71 (2015).
37. Russev, G. & Hancock, R. Assembly of new histones into nucleosomes and their distribution in replicating chromatin. *Proc Natl Acad Sci U S A* **79**, 3143-

7 (1982).
38. Burgess, R.J. & Zhang, Z. Histone chaperones in nucleosome assembly and human disease. *Nat Struct Mol Biol* **20**, 14-22 (2013).
39. Alabert, C. & Groth, A. Chromatin replication and epigenome maintenance. *Nat Rev Mol Cell Biol* **13**, 153-67 (2012).
40. Gasser, R., Koller, T. & Sogo, J.M. The stability of nucleosomes at the replication fork. *J Mol Biol* **258**, 224-39 (1996).
41. Tan, B.C., Chien, C.T., Hirose, S. & Lee, S.C. Functional cooperation between FACT and MCM helicase facilitates initiation of chromatin DNA replication. *EMBO J* **25**, 3975-85 (2006).
42. Gilbert, N. & Allan, J. Supercoiling in DNA and chromatin. *Curr Opin Genet Dev* **25**, 15-21 (2014).
43. Yadav, T. & Whitehouse, I. Replication-Coupled Nucleosome Assembly and Positioning by ATP-Dependent Chromatin-Remodeling Enzymes. *Cell Rep* (2016).
44. Sobel, R.E., Cook, R.G., Perry, C.A., Annunziato, A.T. & Allis, C.D. Conservation of deposition-related acetylation sites in newly synthesized histones H3 and H4. *Proc Natl Acad Sci U S A* **92**, 1237-41 (1995).
45. Loyola, A., Bonaldi, T., Roche, D., Imhof, A. & Almouzni, G. PTMs on H3 variants before chromatin assembly potentiate their final epigenetic state. *Mol Cell* **24**, 309-16 (2006).
46. Jasencakova, Z. et al. Replication stress interferes with histone recycling and predeposition marking of new histones. *Mol Cell* **37**, 736-43 (2010).
47. Hoek, M. & Stillman, B. Chromatin assembly factor 1 is essential and couples chromatin assembly to DNA replication in vivo. *Proc Natl Acad Sci U S A* **100**, 12183-8 (2003).
48. Li, Q. et al. Acetylation of histone H3 lysine 56 regulates replication-coupled nucleosome assembly. *Cell* **134**, 244-55 (2008).
49. Groth, A. et al. Regulation of replication fork progression through histone supply and demand. *Science* **318**, 1928-31 (2007).
50. Winkler, D.D., Zhou, H., Dar, M.A., Zhang, Z. & Luger, K. Yeast CAF-1 assembles histone (H3-H4)2 tetramers prior to DNA deposition. *Nucleic Acids Res* **40**, 10139-49 (2012).
51. Tyler, J.K. et al. The RCAF complex mediates chromatin assembly during DNA replication and repair. *Nature* **402**, 555-60 (1999).
52. Jackson, V. Deposition of newly synthesized histones: hybrid nucleosomes are not tandemly arranged on daughter DNA strands. *Biochemistry* **27**, 2109-20 (1988).
53. Leffak, I.M., Grainger, R. & Weintraub, H. Conservative assembly and segregation of nucleosomal histones. *Cell* **12**, 837-45 (1977).
54. Prior, C.P., Cantor, C.R., Johnson, E.M. & Allfrey, V.G. Incorporation of exogenous pyrene-labeled histone into Physarum chromatin: a system for studying changes in nucleosomes assembled in vivo. *Cell* **20**, 597-608 (1980).
55. Xu, M. et al. Partitioning of histone H3-H4 tetramers during DNA rpelication-dependent chromatin assembly. *Science* **328**(2010).

56. Trujillo, K.M. & Osley, M.A. A role for H2B ubiquitylation in DNA replication. *Mol Cell* **48**, 734-46 (2012).
57. Orphanides, G., LeRoy, G., Chang, C.H., Luse, D.S. & Reinberg, D. FACT, a factor that facilitates transcript elongation through nucleosomes. *Cell* **92**, 105-16 (1998).
58. VanDemark, A.P. et al. The structure of the yFACT Pob3-M domain, its interaction with the DNA replication factor RPA, and a potential role in nucleosome deposition. *Mol Cell* **22**, 363-74 (2006).
59. Wittmeyer, J., Joss, L. & Formosa, T. Spt16 and Pob3 of Saccharomyces cerevisiae form an essential, abundant heterodimer that is nuclear, chromatin-associated, and copurifies with DNA polymerase alpha. *Biochemistry* **38**, 8961-71 (1999).
60. Yeeles, J.T., Janska, A., Early, A. & Diffley, J.F. How the Eukaryotic Replisome Achieves Rapid and Efficient DNA Replication. *Mol Cell* **65**, 105-116 (2017).
61. Kurat, C.F., Yeeles, J.T., Patel, H., Early, A. & Diffley, J.F. Chromatin Controls DNA Replication Origin Selection, Lagging-Strand Synthesis, and Replication Fork Rates. *Mol Cell* **65**, 117-130 (2017).
62. Abe, T. et al. The histone chaperone facilitates chromatin transcription (FACT) protein maintains normal replication fork rates. *J Biol Chem* **286**, 30504-12 (2011).
63. Bondarenko, M.T. et al. [Structure and function of histone chaperone FACT]. *Mol Biol (Mosk)* **49**, 891-904 (2015).
64. Smith, S. & Stillman, B. Purification and characterization of CAF-I, a human cell factor required for chromatin assembly during DNA replication in vitro. *Cell* **58**, 15-25 (1989).
65. Tsurimoto, T. & Stillman, B. Purification of a cellular replication factor, RF-C, that is required for coordinated synthesis of leading and lagging strands during simian virus 40 DNA replication in vitro. *Mol Cell Biol* **9**, 609-19 (1989).
66. Smith, S. & Stillman, B. Stepwise assembly of chromatin during DNA replication in vitro. *EMBO J* **10**, 971-80 (1991).
67. Enomoto, S., McCune-Zierath, P.D., Gerami-Nejad, M., Sanders, M.A. & Berman, J. RLF2, a subunit of yeast chromatin assembly factor-I, is required for telomeric chromatin function in vivo. *Genes Dev* **11**, 358-70 (1997).
68. Berman, J. & Enomoto, S. Chromatin assembly Factor I contributes to the maintenance but not the establishment of silencing at the silent mating loci. *Molecular Biology of the Cell* **8**, 1859-1859 (1997).
69. Mattiroli, F. et al. DNA-mediated association of two histone-bound complexes of yeast Chromatin Assembly Factor-1 (CAF-1) drives tetrasome assembly in the wake of DNA replication. *Elife* **6**(2017).
70. Krude, T. Chromatin assembly factor 1 (CAF-1) colocalizes with replication foci in HeLa cell nuclei. *Exp Cell Res* **220**, 304-11 (1995).
71. Shibahara, K. & Stillman, B. Replication-dependent marking of DNA by PCNA facilitates CAF-1-coupled inheritance of chromatin. *Cell* **96**, 575-85 (1999).

72. Zhang, K. et al. A DNA binding winged helix domain in CAF-1 functions with PCNA to stabilize CAF-1 at replication forks. *Nucleic Acids Res* **44**, 5083-94 (2016).
73. Marzluff, W.F. & Duronio, R.J. Histone mRNA expression: multiple levels of cell cycle regulation and important developmental consequences. *Curr Opin Cell Biol* **14**, 692-9 (2002).
74. Tyler, J.K. et al. Interaction between the Drosophila CAF-1 and ASF1 chromatin assembly factors. *Mol Cell Biol* **21**, 6574-84 (2001).
75. Liu, W.H., Roemer, S.C., Port, A.M. & Churchill, M.E. CAF-1-induced oligomerization of histones H3/H4 and mutually exclusive interactions with Asf1 guide H3/H4 transitions among histone chaperones and DNA. *Nucleic Acids Res* **40**, 11229-39 (2012).
76. Franco, A.A., Lam, W.M., Burgers, P.M. & Kaufman, P.D. Histone deposition protein Asf1 maintains DNA replisome integrity and interacts with replication factor C. *Genes Dev* **19**, 1365-75 (2005).
77. Richet, N. et al. Structural insight into how the human helicase subunit MCM2 may act as a histone chaperone together with ASF1 at the replication fork. *Nucleic Acids Res* **43**, 1905-17 (2015).
78. Huang, H. et al. A unique binding mode enables MCM2 to chaperone histones H3-H4 at replication forks. *Nat Struct Mol Biol* **22**, 618-26 (2015).
79. English, C.M., Adkins, M.W., Carson, J.J., Churchill, M.E. & Tyler, J.K. Structural basis for the histone chaperone activity of Asf1. *Cell* **127**, 495-508 (2006).
80. Sogo, J.M., Stahl, H., Koller, T. & Knippers, R. Structure of replicating simian virus 40 minichromosomes. The replication fork, core histone segregation and terminal structures. *J Mol Biol* **189**, 189-204 (1986).
81. Herman, T.M., DePamphilis, M.L. & Wassarman, P.M. Structure of chromatin at deoxyribonucleic acid replication forks: location of the first nucleosomes on newly synthesized simian virus 40 deoxyribonucleic acid. *Biochemistry* **20**, 621-30 (1981).
82. Lucchini, R., Wellinger, R.E. & Sogo, J.M. Nucleosome positioning at the replication fork. *EMBO J* **20**, 7294-302 (2001).
83. Randall, S.K. & Kelly, T.J. The fate of parental nucleosomes during SV40 DNA replication. *J Biol Chem* **267**, 14259-65 (1992).
84. Bonne-Andrea, C., Wong, M.L. & Alberts, B.M. In vitro replication through nucleosomes without histone displacement. *Nature* **343**, 719-26 (1990).
85. Leman, A.R. & Noguchi, E. The replication fork: understanding the eukaryotic replication machinery and the challenges to genome duplication. *Genes (Basel)* **4**, 1-32 (2013).
86. Georgescu, R., Langston, L. & O'Donnell, M. A proposal: Evolution of PCNA's role as a marker of newly replicated DNA. *DNA Repair (Amst)* **29**, 4-15 (2015).
87. Smith, D.J. & Whitehouse, I. Intrinsic coupling of lagging-strand synthesis to chromatin assembly. *Nature* **483**, 434-8 (2012).
88. Li, M. et al. Dynamic regulation of transcription factors by nucleosome

remodeling. *Elife* **4**(2015).
89. Ramachandran, S. & Henikoff, S. Transcriptional Regulators Compete with Nucleosomes Post-replication. *Cell* **165**, 580-92 (2016).
90. Lowary, P.T. & Widom, J. New DNA sequence rules for high affinity binding to histone octamer and sequence-directed nucleosome positioning. *J Mol Biol* **276**, 19-42 (1998).
91. Afek, A., Sela, I., Musa-Lempel, N. & Lukatsky, D.B. Nonspecific transcription-factor-DNA binding influences nucleosome occupancy in yeast. *Biophys J* **101**, 2465-75 (2011).
92. Osberg, B., Nuebler, J., Korber, P. & Gerland, U. Replication-guided nucleosome packing and nucleosome breathing expedite the formation of dense arrays. *Nucleic Acids Res* **42**, 13633-45 (2014).

CHAPTER 2

DNA LOOPING MEDIATES NUCLEOSOME TRANSFER

Nature Communication, 2016 Nov 3; 7:13337. Doi: 10.1038/ncomms13337. Brennan, L.D.*, Forties, R.A.*, Patel, S.S., Wang, M.D. *DNA Looping Mediates Nucleosome Transfer*. Adapted with permission from Nature Publishing Group. *Equal contribution

LB, RAF, and MDW designed the experiments and wrote the manuscript. LB and RAF performed the mechanical displacement assay. LB performed the helicase unwinding assays, supplementary single molecule experiments, and competitor DNA bulk replication assay, and purified the histones. RAF performed the bulk replication assay, the initial DNA looping theoretical calculations, and wrote the custom data analysis software. SSP provided the purified T7 gp4' and helped to revise the manuscript. MDW supervised the project.

INTRODUCTION

At the replication fork, a complex interplay of proteins and DNA mediate the faithful duplication of DNA sequence and the subsequent packaging of nascent DNA into chromatin [1,2]. The spatial organization of epigenetic chromatin modifications is maintained throughout multiple rounds of cell division by the inheritance of parental nucleosomes and the ensuing duplication of covalent modifications to nascent nucleosomes [3,4]. Parental nucleosomes must be quickly moved from ahead of the progressing replisome to the newly replicated DNA behind it [4-6], without release of the H3/H4 tetramers into solution [7,8]. Thus the transfer of parental nucleosomes requires stringent temporal and spatial regulation, and must remain reliable within a dynamic cellular environment. This alludes to a simplicity underlying the fundamental transfer mechanism – a means that is permissive of cellular changes and fluctuations, while still preserving the essential nucleosome topography.

Current views suggest that histone chaperones and nucleosome assembly factors act in a coordinated manner at the replication fork to shuttle parental histones and deposit nascent histones to newly replicated DNA [2,9]. However, this theory is only loosely described and neglects the role of DNA itself, the fundamental component of nucleosome organization and dynamics. The complex, dynamic environment within which nucleosome transfer occurs is a challenging setting to define essential roles of the individual components that underlie the transfer mechanism. To examine the role of DNA mechanics and identify the minimum system requirements for successful transfer, we utilized a DNA template with a single nucleosome and incrementally added complexity by first displacing the nucleosome mechanically, then with an isolated replicative helicase, and finally with a simplified replication complex. This process

allowed us to quantify a fundamental aspect of nucleosome transfer and establish a critical role for the physical properties of DNA during chromatin replication.

MATERIALS & METHODS

Protein purification

Histones were purified using hydroxyapatite precipitation from 6 liters of HeLa-S3 cells purchased from the National Cell Culture Center. Nuclei were extracted from one, 6 L, pellet of HeLa-S3 cells in Nuclear Pellet Prep Lysis Buffer (20 mM HEPES pH 7.5, 3 mM $MgCl_2$, 250 mM sucrose, 0.5% (v/v) IGEPAL CA-630 (NP-40) nonionic detergent, 1 tablet/ 50 mL Complete™ protease inhibitor cocktail (Roche), 3 mM 2-mercaptoethanol as described previously [45]. The nuclei pellets were frozen in liquid nitrogen and stored at -80°C. The following day, core histones were purified using a hydroxyapatite (HAP) Bio-gel® HTP gel (Bio-Rad Laboratories) slurry, according to methods by Wolffe and Ura [46] with the omission of MNase digestion prior to fractionation. Aliquots of purified histones were stored in -80°C at a final concentration of 2.7 μM.

Nucleosomes were assembled on the Widom 601 nucleosome positioning element[47] by salt dialysis [48,49]. For the mechanical displacement assay, nucleosomes were assembled on a 764 bp template at a molar ratio of 1.25:1.00 of histone octamer to DNA. For the helicase displacement assay, nucleosomes were assembled on an 896 bp template in the presence of salmon sperm competitor DNA (Life technologies) at a 1.5:1.0:4.0 molar ratio of histone octamer: template DNA: salmon sperm DNA. For the replication gel experiments, nucleosomes were assembled on a 250 bp template at a molar ratio of 1.75:1.00 of histone octamer to DNA.

Wildtype T7 helicase gp4A' was obtained from the Patel Lab where it was purified from *E. coli*, as described previously [50].

DNA template construction

All experiments required the use of forked DNA templates, each of which consist of two arms and a trunk. These templates were prepared by the ligation of DNA adapter oligos to a labelled PCR product. The adapter oligos contained a single-strand DNA region that anneal to one another thus forming a Y-structure DNA template similar to that previously described [51]. For all single molecule experiments, each arm was ~1000 bp. For the mechanical displacement experiments, the trunk consists of either a 784 bp or a 896 bp segment containing the 601 nucleosome positioning sequence ligated to 2.9 kbp downstream DNA at 16ºC for 90 min. This resulted in a total trunk length of 3751 bp and 3883 bp respectively. A second extended DNA trunk of 2930 bp was created in order to determine the effect of DNA sequence on nucleosome transfer (Figure 2.4) and ligated to the 764 bp trunk. The helicase displacement experiments were performed using a template containing the 836 bp segment and the 2987 bp downstream DNA.

For the leading strand replication gel experiments, the initial replication fork consisted of a trunk of a 298 bp dsDNA containing the 601 nucleosome positioning element, a 30 nucleotide flap of ssDNA to facilitate T7 helicase loading to the replication fork [52,53], and a 1189 bp dsDNA leading strand.

Competitor DNA was synthesized by PCR, following a protocol identical to that of the 2.9 kbp downstream DNA segment used in the mechanical displacement experiments.

Mechanical displacement of nucleosome assay

DNA tethers were formed in flow chambers and were unzipped using an optical trap with a loading rate clamp of 10 pN s^{-1} (Figure 2.1, 2.2, 2.4) through the bound protein as described previously [10,54]. Briefly, chambers were first incubated with anti-digoxygenin at 0.2 mg ml^{-1} for 5 min, and then the surface was blocked by incubation with casein at 5 mg ml^{-1} for 5 min. Then DNA templates were flowed into the chamber at 100 pM for 5 min. This was followed by incubation with 500 nm streptavidin-coated microspheres at 4 pM, which bound to the biotin linkers on the DNA template. Finally, chambers were washed with nucleosome unzipping buffer (10 mM Tris pH 8, 1 mM EDTA, 100 mM NaCl, 3% (v/v) glycerol,1.5 mM $MgCl_2$, 1 mM DTT, 0.02% Tween 20, 2 mg mL^{-1} AcBSA (Ambion), and 0.1 mg ml^{-1} Casein). Experiments were performed at room temperature (24°C). For experiments involving competitor DNA, the competitor DNA was diluted in 1x nucleosome unzipping buffer to the specified concentration and then flowed into the single molecule chamber immediately before data acquisition.

The number of DNA base pairs unzipped as at each time point was calculated from the raw force and extension measurements [10]. We then applied an algorithm which defined peaks as a force rise greater than or equal to 20 pN which increased at a rate greater than 3 pN s^{-1}. Nucleosomes were identified as containing peaks separated by less than 65 bp, up to a maximum of three, in accordance with previous work [10]. Individual force peaks separated by more than 65 bp were considered to be tetrasomes as previously described [11,12]. Nucleosome transfer distances were

measured as the distance from the first peak within the 601 nucleosome positioning element to the first peak outside of the defined nucleosome force signature. For a trace to be categorized as having no nucleosome transfer, it must show no detectable force rise significantly above the naked DNA unzipping baseline. Only tethers that were unzipped to the end of the DNA construct were included in the data set to avoid any sampling bias due to nicks in the DNA.

Helicase displacement of nucleosome assay

DNA tethers were prepared as described above, and helicase preparation was similar to that previously described [26]. Briefly, 1.5 nM of the helicase monomer was incubated for up to 20 min in the modified nucleosome unzipping buffer (10 mM Tris pH 8, 1 mM EDTA, 100 mM NaCl, 3% (v/v) glycerol,1.5 mM $MgCl_2$, 1 mM DTT, 0.02% Tween 20, 2 mg mL^{-1} AcBSA (Ambion), 1 mg mL^{-1} Casein, 2 mM dTTP). Magnesium chloride was added to a final concentration of 3 mM immediately before helicase addition to the sample chamber. Experiments were conducted using the following steps. First, approximately 400 bp of dsDNA were mechanically unzipped, at a constant velocity of 200 nm s^{-1} for 2 seconds, to produce a ssDNA loading region for helicase. The tether was held at a constant position for up to 120 s for helicase loading to occur, if loading did not occur within this time frame, the tether was released and a new tether was selected. If the force dropped below 10 pN, owing to helicase loading and initiation of unwinding, the tether was then held at a constant force of 12 pN as the helicase position was tracked.

In order to detect helicase pausing, the dwell time of each trace as a function of the number of base pairs unzipped was calculated, with a bin size of 10 bp. We then defined dwell times of at

least 0.5 s per 10 bp bin as pauses. The end of a pause was defined as dwells less than 0.2 s per 10 bp bin. Pauses separated by more than 30 bp were considered to be spatially distinct events. To determine the nucleosome transfer distance, we measured the number of base pairs between the first pause, which was located within the initial positioned nucleosome element, and the second pause. As was done for the mechanical displacement experiments, only tethers that were unzipping to the end of the DNA construct were included in the data set.

Bulk DNA replication assay

T7 replication assays were performed in 50 µl reaction volumes (or 10 µl reaction volumes for controls which were not exonuclease III digested, as indicated in the main text) containing 40 mM Tris pH 7.5, 10 mM $MgCl_2$,10 mM dithiothreitol, 0.1 mg ml^{-1} AcBSA (Ambion), and 0.6 mM of each of dATP, dCTP, dGTP and dCTP (Roche). DNA templates were added to a final concentration of 10 nM. Replisomes were formed by pre-incubating 1 unit μl^{-1} T7 DNA polymerase (NEB) and 1 µM T7 helicase in reaction buffer on ice for 5 minutes, and then were added to a final concentration of 0.1 unit μl^{-1} T7 DNA polymerase (NEB) and 100 nM T7 helicase and incubated at 37°C for 10 min. Samples were then buffer exchanged into 1X NEBuffer 1 (NEB) using Amicon Ultra-0.5 centrifugal filter units with Ultracel-30 membranes (Millipore). 400 µl 1X NEBuffer 1 was added and samples were centrifuged at 5,000g for 5 min at 4°C four times total. Samples were spun an additional 5 min at 4°C for the final concentration to reduce the retained volume. Each reaction was then digested with 100 units of exonuclease III (NEB) at 37°C for 30 min.

Samples were precipitated by addition of 500 µl solution containing 0.5% linear polyacrylamide, 7% saturated ammonium acetate, and 91% ethanol [55], incubated overnight at -80°C, and centrifuged at 16,000g for 20 min. Samples were then decanted and 500 µl 70% ethanol was added followed by vigorous vortex mixing. This was followed by centrifugation at 16,000g for 10 min. Tubes were then carefully decanted, and dried for 5 min in a vacuum chamber. Pellets were resuspended in 20 µl of alkaline gel buffer (5 mM NaOH, 1 mM EDTA) by vortexing and incubated for 30 min at 37°C. 4 µl alkaline loading buffer (50% glycerol, 30 mM NaOH, 6 mM EDTA) was then added and each sample was heated at 95°C for 5 min to denature the DNA, and then placed on ice. Samples were separated on 1% agarose gels in alkaline gel buffer using electrophoresis at 4.7 V cm^{-1} for 4 hours, and quantified using a Typhoon imager (GE).

Data were then converted from intensity at each position within a gel scan to probability distributions for nucleosome transfer distance. The Cy5 labeled DNA ladder was created using PCR products of 125, 332, 497, 649, 859, 1390 and 1788 bp. We calculated the DNA length corresponding to these ladder positions by fitting the log of ladder band length versus gel position to a quadratic function, and then linearly interpolated between ladders run in different lanes. The intensity was summed within each lane in 25 bp increments to obtain a probability distribution versus DNA length. Transfer distance distributions were obtained by subtracting the measured DNA length from the known initial position of the 601 sequence (1500 bp for the Cy5 labeled strand). Data obtained for naked DNA templates was subtracted from data for nucleosome transfer to account for incomplete digestion by exonuclease III.

For replication reactions run in the presence of competitor DNA (Figure. 2.9), the data were analyzed as described above with the following modifications. The gel scan from each reaction was first background subtracted and then normalized by the total amount of fully replicated DNA before exonuclease digestion. The normalized nucleosome transfer was then calculated by integrating the line scans from 1200 bp to 100 bp (corresponding to 300 -1400 bp transfer distances) and normalizing it by that under 0 ng μL^{-1} competitor DNA condition.

DNA loop formation modeling

The DNA looping probability, or the Jacobson-Stockmayer *J*-factor [56], was calculated for a dsDNA with a persistence length of 50 nm using the worm-like-chain model from Eq. 50 of Shimada and Yamakawa[57]. This formula diverges for DNA lengths longer than 2000 bp, so for long DNA we applied the Daniels approximation[58]. For a given length of DNA, this *J*-factor gives the effective DNA molar concentration of one end of a DNA molecule at its other end under the assumption that the DNA ends are free to adopt any orientation relative to one another. Therefore, the *J*-factor describes the equilibrium constant for forming a DNA loop. To compare with our measured nucleosome transfer distance distribution, the *J*-factor is converted to a probability density function over all possible lengths and then rescaled to the number of traces in each data set. This comparison assumes that the probability of a nucleosome transfer to a destination site is proportional to the equilibrium probability of DNA loop formation that bridges the nucleosome's original position with the destination site. This is a reasonable assumption since in our unzipping configuration, the time scale of a nucleosome transfer (estimated based on the time it takes to unzip through a nucleosome: about 4 s for Figure 2.1 and 0.44 s for Figure

2.5) is much slower than that of the mean first passage time of DNA looping, which is in the order of milliseconds[59].

To determine the effective DNA weight concentration of the available downstream DNA at the nucleosome (C_0), the *J*-factor in molar concentration for a given length of DNA was then integrated over the entire length of the downstream DNA before conversion to a weight concentration. For the 2.9 kbp downstream DNA, this corresponds to C_0 = 100 ng μL^{-1}. In the presence of competitor DNA, a simple competitive binding relation was used to predict the probability of transfer to the downstream DNA as a function of competitor DNA concentration (C): $f = \frac{C_0}{C + C_0}$. This expression does not consider any excluded volume effect which should become substantial at high competitor DNA concentrations. This should occur when the volume explored by a single competitor DNA molecule over its radius of gyration reaches the mean volume available for each competitor DNA molecule in solution. We estimate that for the 2.9 kbp DNA, the excluded volume effect needs to be considered for C > 110 ng μL^{-1}.

Statistical Analysis

To compare the measured transfer distributions with the DNA looping model, we carried out the Pearson's reduced chi-square test to quantitatively determine the goodness of the agreement for the data shown in both Figure 2.1c and Figure 2.2c. Both data sets were binned into 400 bp bins as was the theory curve. In each case, this test yielded a reduced χ^2 value and a corresponding *p*-value. The *p*-value is the probability of observing a difference between the measurements and theory as extreme as what have been measured, assuming the measurements were from the

theoretical distribution. The *p*-values (0.81 for Figure 2.1C and 0.95 for Figure 2.3C) indicate a strong agreement between the measurements and the DNA looping model.

Error bars in Figure 2.6C and Table 2.2 were calculated using Matlab's built-in function, binofit. [phat,pci] = binofit(*x*,*n*) returns a maximum likelihood estimate of the probability of success, phat**,** in a given binomial trial based on the number of successes, *x*, observed in *n* independent trials and the 95% confidence intervals, pci. binofit uses the Clopper-Pearson method to calculate confidence intervals.

RESULTS

Passive nucleosome transfer after mechanical displacement

In a solution with no free histones, a 3.7 kbp dsDNA template, containing a single positioned nucleosome, was mechanically unzipped using an optical trap (Figure. 2.1A). The resulting unzipping force served as a sensitive detector for the presence of the nucleosome, with a force rise above the naked DNA baseline indicating both nucleosome location and composition (Figure 2.1B) [10-15]. During unzipping, the force first followed that of naked DNA, until the fork reached the positioning sequence, and then a dramatic force rise characteristic of a canonical nucleosome [10] occurred, followed by a force drop. As unzipping continued, additional distinct force signatures emerged along the downstream DNA (in front of the moving fork), indicating a re-association of the displaced histone. When the same construct was unzipped in the opposite direction, no force rise occurred until the nucleosome-positioning sequence, illustrating the mono-nucleosome nature of the template (Figure 2.2).

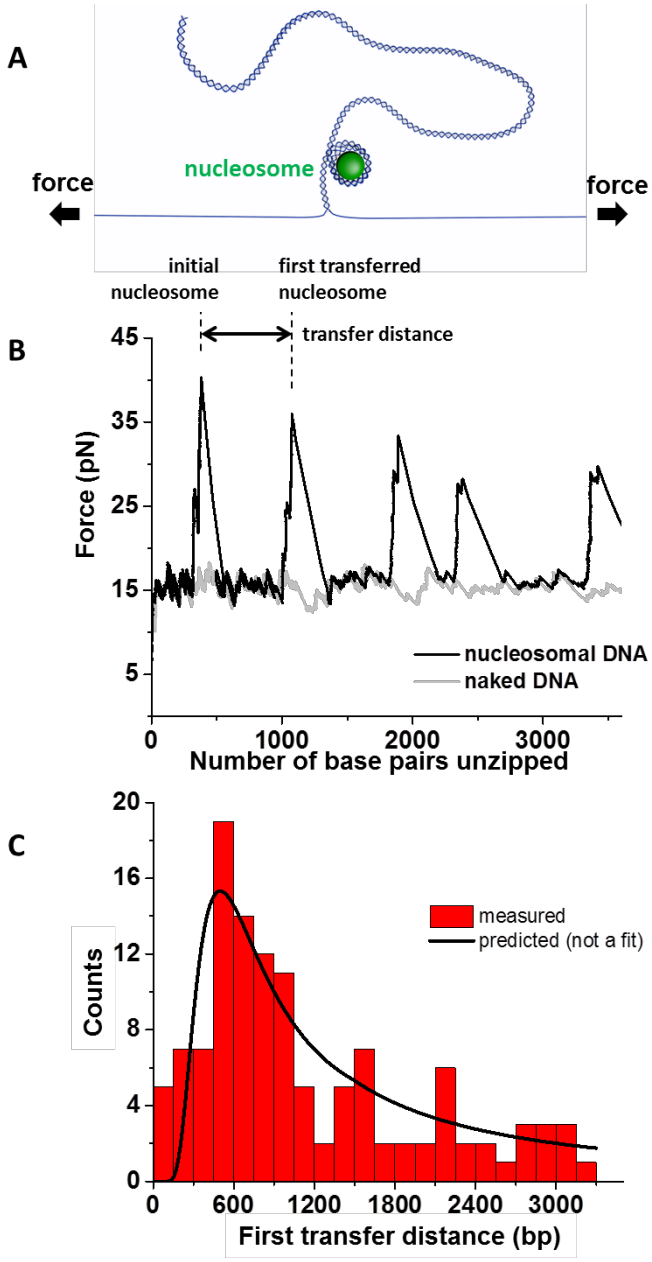

Figure. 2.1: Mechanical displacement of a single nucleosome.

(A) Experimental configuration. A single dsDNA molecule was mechanically unzipped using an optical trap. The dsDNA contained a positioned nucleosome followed by a long (2.9 kbp) segment of naked DNA.

(B) A representative unzipping trace. A force rise from the naked DNA baseline indicated the detection of a bound protein complex. A dashed vertical line indicates the dyad location of a nucleosome.

(C) Histogram of nucleosome transfer distance. A transfer distance was obtained from the first transfer event of each trace. The histogram was obtained by pooling data from 121 traces. The prediction (not a fit) from the DNA looping model is plotted for comparison. The resulting Pearson test gives a reduced χ^2 of 0.53 with a *p*-value of 0.81 (Methods; Figure 2.3A).

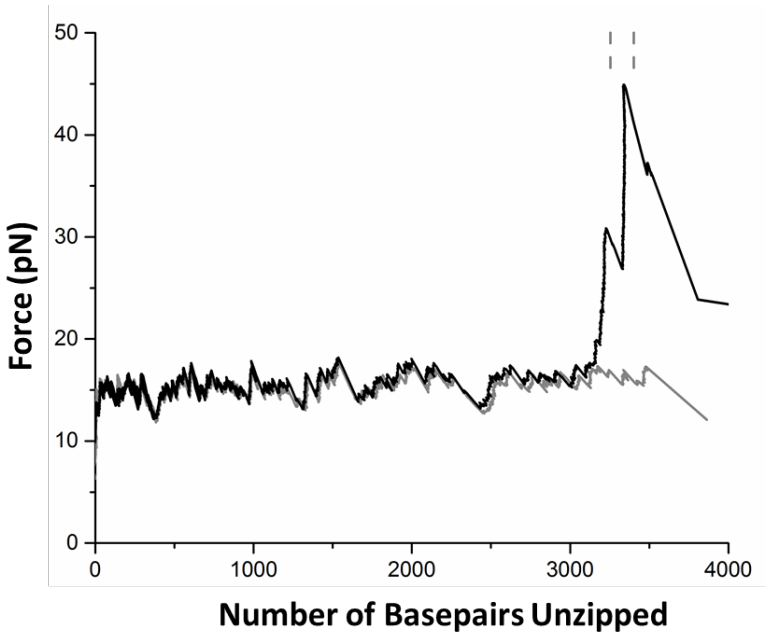

Figure 2.2: Mapping of nucleosome position on a DNA template in the reverse direction as that described in Figure 2.1.

The nucleosomal DNA template mechanically unzipped in Figure 2.1 was constructed by ligation of a DNA template containing a single positioned nucleosome to a long naked DNA downstream. This design should ensure that the nucleosomes detected downstream of the initially nucleosome were a result of nucleosome transfer, and not due to additional nucleosomes pre-existing on the template. In order to verify this, we conducted a control experiment to mechanically unzip the same nucleosomal template as used in Figure 2.1 but in the reverse direction. The figure above shows a representative trace of this control experiment. Out of all the traces unzipped (N = 48), 92% showed a single nucleosomal force signature located within the expected 601 sequence (grey), and a complete absence of any force peaks above the baseline prior to the initial nucleosome. A few traces showed a force signature away from the 601 sequence, most likely due to over-assembly of the nucleosome used for this control experiment. Note that the nucleosomal templates used in experiments for the main figures were slightly under-assembled (see Figure 2.5).

We therefore attribute the subsequent force signatures to the transfer of the original nucleosome. The vast majority of unzipping traces (99%) showed at least one transfer event. For the first such transfer event on each unzipped template (Table 2.1), 67% of traces showed a force signature consistent with that of a nucleosome [10] and 32% were consistent with that of a tetrasome [11,12], though it is possible that some of these may have been hexasomes [16,17]. These results are in agreement with previous findings that parental H3/H4 tetrasomes generally remain intact after replication fork passage, while H2A/H2B dimers are more labile [18,19].

# of traces	Nucleosome	Tetrasome	Naked DNA
Before disruption N=192	$63.5^{+6.8}_{-7.2}$ %	$6.7^{+4.6}_{-3.1}$ %	$30.2^{+7.0}_{-6.4}$ %
First transfer N=122	$67.2^{+8.2}_{-9.1}$ %	$32.0^{+9.1}_{-8.2}$%	$0.8^{+3.7}_{-0.8}$ %
Second transfer N=122	$53.3^{+9.1}_{-9.3}$ %	$42.6^{+9.3}_{-4.9}$ %	$4.1^{+5.2}_{-2.8}$ %

Table 2.1: Summary of the structures of transferred nucleosomes after mechanical displacement.

Data from mechanical displacement of a nucleosome were analyzed as described in the Methods section and the number of traces for each type of nucleosome is included in this table. Out of a total of 193 traces, 122 traces (63.2%) and 13 traces (6.7%) showed a force signature within the NPE consistent with that of a canonical nucleosome and a tetrasome respectively. The remaining 58 traces (30.1%) showed a force signature corresponding to naked DNA, indicative of a slight under-assembly of the nucleosomes. Only the traces with a nucleosome at the 601 positioning sequence were further analyzed (Figure 2.1C). For the first transfer event, out of 122 traces, 82 traces (67%) and 39 traces 32%) showed a force signature consistent with a canonical nucleosome or tetrasome, respectively. Only one trace (0.8%) showed a positioned nucleosome without any subsequent transfer and was therefore not included in Figure 2.1C.

Nucleosome transfer is consistent with DNA loop formation

Nucleosome transfer in this experimental system could occur via a diffusion-based process, during which histones dissociate from the DNA after being displaced by the fork, diffuse in solution, and then re-associate with another DNA segment. However, this mechanism would result in a distribution of transfer distance that peaks at zero, because histones would most likely associate with a DNA segment in close proximity, such that short distance transfer dominates. In contrast, our data of the first transfer distance peaked at 500-700 bp, and do not support histone dissociation and diffusion. Previous studies also provide evidence indicating that during replication, parental histones are not released into solution[7,8,20], arguing against a diffusion-based mechanism.

An alternative mechanism for nucleosome transfer is based on DNA looping. Upon fork invasion of the nucleosome, the histone surfaces become partially exposed and available dsDNA may loop back onto the histone surfaces and capture the histones. As the fork progresses, the nucleosome is thereby repositioned to another location on the DNA. Although this possibility was raised nearly twenty years ago [8], there has been no direct experimental evidence to date. Importantly, support for such a model must be made quantitatively, because DNA loop formation makes explicit predictions on the loop size distribution [21-24] and thus the nucleosome transfer distance distribution. Transfer distances below 200 bp are energetically unfavorable as the persistence length of DNA is approximately 150 bp, thus prohibiting the formation of small loops. Very long transfer distances are also improbable, because the putative acceptor DNA must sample a large volume, reducing its chance of encountering the initial nucleosome.

Consequently, the defining features of the DNA looping model are an extremely low transfer probability at short distances, a sharp rise in the probability at ~ 200 bp followed by a peak at ~ 500 bp, and a long tail.

Figure 2.1C shows a comparison of measured transfer distances and a direct prediction by the loop formation theory (not a fit). There is a good agreement between the two distributions (Methods; Figure 2.3A). The loop formation model depends predominantly on the persistence length of DNA which dictates the likelihood of downstream DNA being in close proximity to the nucleosome. Although persistence length is DNA sequence-dependent [25], such dependence should be secondary on the length scale considered here. Consistent with this, an additional experiment conducted with a DNA template of a different sequence yielded a similar transfer distance distribution (Figure. 2.4). Additionally, we found that increasing the rate of unzipping ten-fold does not lead to major changes in the transfer distance distribution or efficiency, although there is a slight increase in the nucleosome fraction (Figure 2.5; Table 2.2).

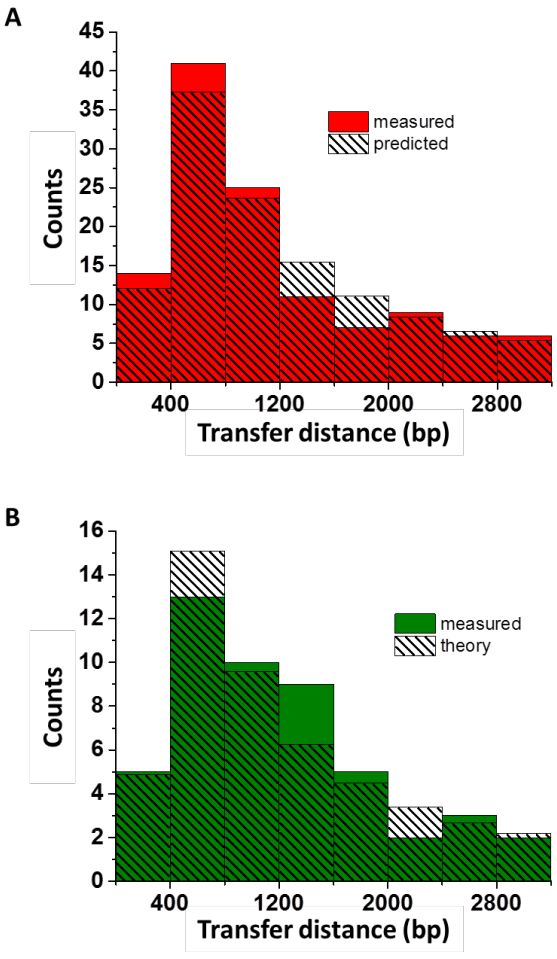

Figure 2.3: Comparison of measured and predicted nucleosome transfer distances.

(A) The transfer distances from the mechanical displacement of a single nucleosome data (from Figure 2.1C) is overlaid with the predicted count calculated from the DNA-looping model, all binned in 400 bp increments. The Pearson test gives a reduced χ^2 of 0.53 with a *p*-value of 0.81 (see Methods for details).

(B) The transfer distances from the T7 helicase displacement of a single nucleosome data (from Figure 2.7C) is overlaid with the predicted count calculated from the DNA-looping model, all binned in 400 bp increments. The Pearson test gives a reduced χ^2 of 0.31 with a *p*-value of 0.95 (see Methods for details).

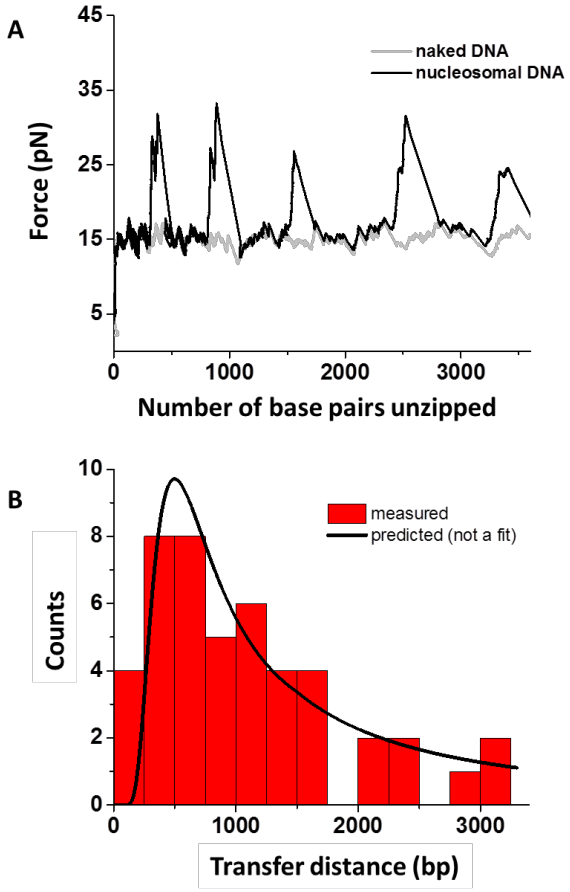

Figure 2.4: Mechanical displacement of a nucleosome on a reverse-sequence DNA template.

(A) Representative trace for mechanical displacement of a nucleosome on a different DNA template. The first 764 bp of the DNA template containing the 601 nucleosome positioning element was identical to that used for Figure 2.1. However, this segment was then ligated to a 2927-bp segment, which was identical to the 2987-bp segment used in Figure 2.1 except for the slightly shorter length, but had a reversed sequence (Methods). Therefore, if the peak position at 500-700 bp of transfer distance shown in Figure 2.1C were due to the DNA sequence favoring nucleosome association at those positions, then the peak position for this template would be shifted to 3000-3200 bp.

(B) The measured transfer distance distribution for this template shows no substantial differences from that of Figure 2.1C, again peaking at 500-700 bp. This suggests that DNA sequence is not a primary factor influencing our observed transfer distance distribution.

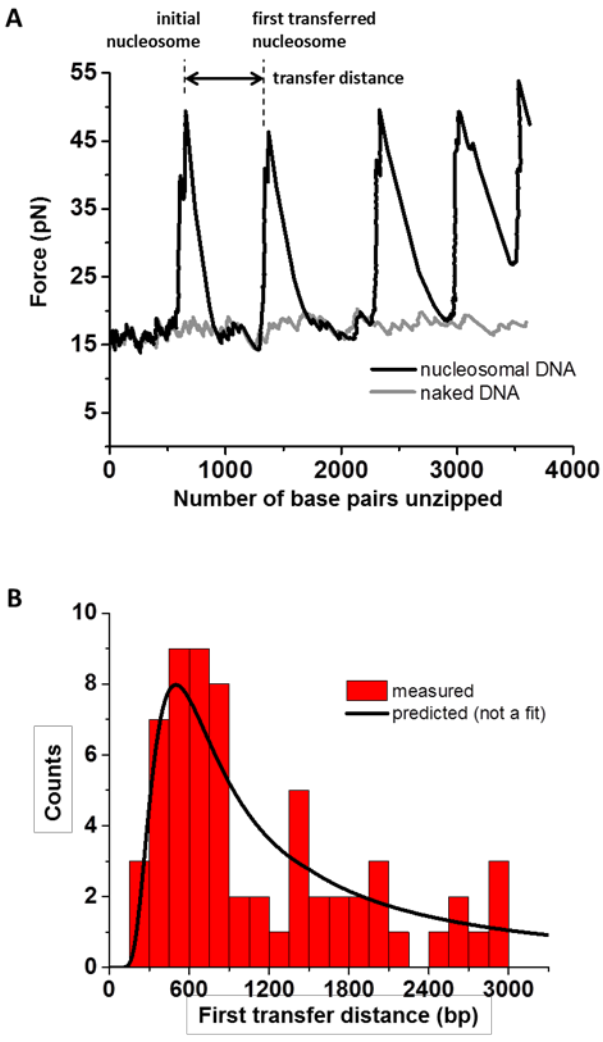

Figure 2.5: Mechanical displacement of a nucleosome at 100 pN/s loading rate clamp.

(A) Representative trace for mechanical displacement of a nucleosome by unzipping DNA using a 100 pNs^{-1} loading rate clamp. The structures of the initial and transferred nucleosomes are consistent with those measured using a 10 pN s^{-1} loading rate clamp (Figure 2.1A), except for an increase in the peak forces.

(B) The measured transfer distance distribution at this faster unzipping rate and the prediction by the DNA loop formation model. This suggests that the rate at which the nucleosome is disrupted is slower than that of DNA loop formation, the latter being in the millisecond time

scale [2]. There is, however, a slight increase in the nucleosome fraction for the first transfer event (Table 2.2).

# of traces	Nucleosome	Tetrasome	Naked DNA
Before disruption N=95	$66.3^{+10.4}_{-9.4}$ %	$7.4^{+7.2}_{-4.4}$ %	$26.3^{+10.0}_{-8.5}$ %
First transfer N=63	$81.0^{+8.8}_{-11.9}$ %	$19.0^{+11.9}_{-8.8}$ %	$0.0^{+5.7}_{-0.0}$ %

Table 2.2: Summary of the structures of transferred nucleosomes after mechanical displacement at 100 pN/s loading rate clamp

For mechanical displacement of a nucleosome using a 100pN/s loading rate clamp, out of 95 traces, 63 (66.3%) traces showed a force signature consistent with that of a nucleosome at the initial position, 7 (7.4%) traces showed a signature indicative of a tetrasome, and the remaining 25 (26.3%) traces showed a force signature consistent with naked DNA. Only the traces with a nucleosome at the 601 positioning sequence were further analyzed. For the first transfer event, 51(81%) traces showed a nucleosome signature and 12 (19%) traces showed that of a tetrasome.

Local DNA concentration and DNA elasticity dictate transfer

To further examine whether DNA looping mediates nucleosome transfer, we carried out nucleosome disruption experiments in the presence of competitor DNA (Figure 2.6A), which should compete with the downstream DNA for acceptance of a transferred nucleosome. The DNA looping model directly predicts an effective local concentration of the available downstream DNA at the nucleosome (Methods), and thus nucleosome transfer to downstream DNA should decrease with an increase in competitor DNA concentration, following a simple competitive binding relation (Methods).

In these experiments, nucleosomes were disrupted in the presence of varying concentrations of competitor DNA that was of nearly equal length as that of the downstream DNA. As expected, with an increase in competitor DNA concentration, the probability for nucleosome transfer to the downstream DNA decreased. Example trace without and with transfer to the downstream DNA are shown in Figure 2.6B. Figure 2.6C shows a summary of the probability of transfer to the downstream DNA as a function of competitor DNA concentration, along with a direct prediction (not a fit) based on a simple competitive binding relation. There is good agreement between measurements and prediction at competitor DNA concentrations ≤ 100 ng μL^{-1}; concentrations above this threshold resulted in measured values somewhat larger than predicted. Deviation in this range is likely due to the use of a simple competitive binding relation without consideration of the excluded volume effect (Methods), which becomes significant at high competitor DNA concentrations resulting in a preference for intra-DNA transfer. Therefore, over the range where the competitive binding relation holds, these results support DNA loop formation as the mechanism of nucleosome transfer.

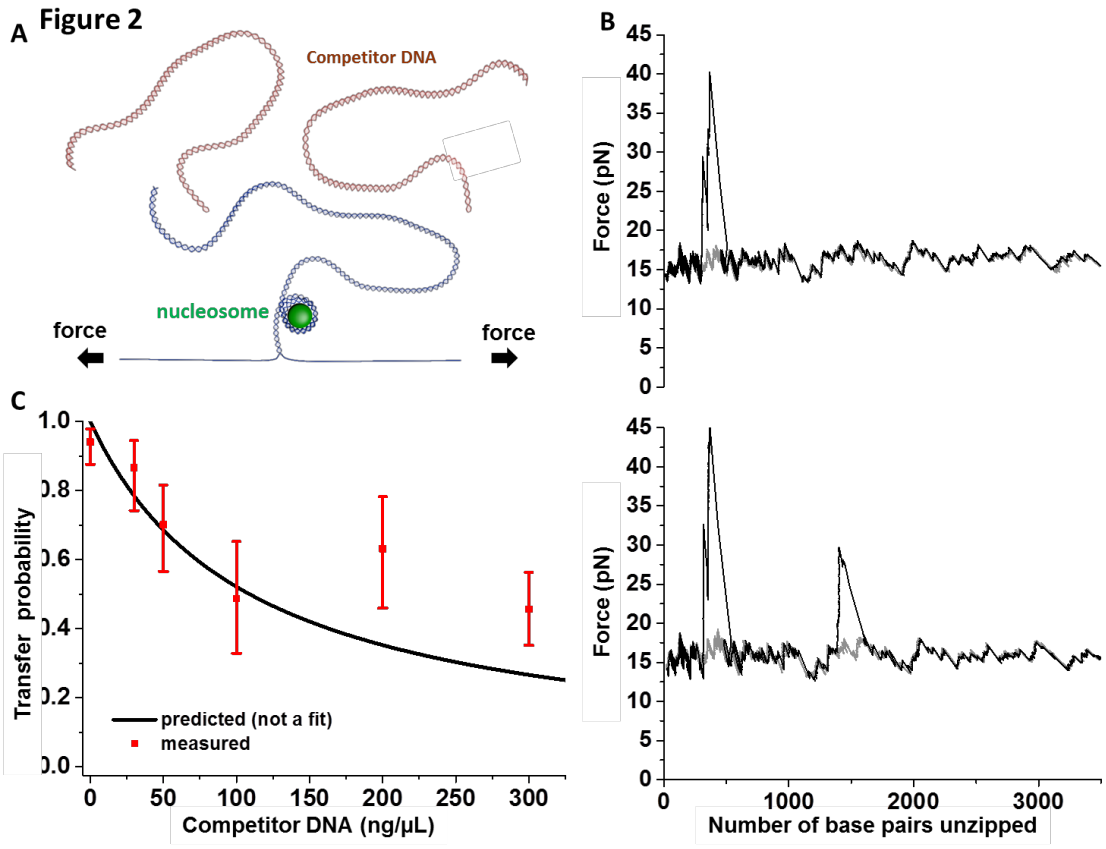

Figure. 2.6: Mechanical displacement of a single nucleosome in the presence of competitor DNA.

(A) Experimental configuration. A single dsDNA molecule was mechanically unzipped using an optical trap. The dsDNA contained a positioned nucleosome followed by 2.9 kbp of naked DNA. Linear competitor 2.9 kbp dsDNA was introduced into the chamber at varying concentrations immediately prior to mechanical disruption.

(B) Two example unzipping traces in the presence of 100 ng/μL of competitor DNA. The top trace shows an absence of a transferred nucleosome to the downstream DNA, whereas the bottom trace shows the presence of a transferred nucleosome.

(C) The probability of nucleosome transfer to downstream dsDNA as a function of competitor DNA concentration. Error bars represent 95% confidence intervals. A direct prediction (not

a fit) based on DNA looping and a simple competitive binding relation (Methods) is shown for comparison.

Helicase-induced nucleosome transfer

Although fork progression was initially carried out mechanically, *in vivo* it is mediated by helicases that unwind dsDNA during replication. We therefore used T7 helicase as a simple model system to investigate the fate of a single nucleosome located on a parental dsDNA template during unwinding (Figure 2.7A). As shown in Fig. 2.7B, prior to encountering the nucleosome, the helicase unwound the dsDNA at the expected rate, as reported previously [26-28]. Upon encountering the nucleosome, the helicase showed a discrete pause, consistent with previous studies that characterized nucleosomes as major barriers for helicase unwinding [29]. Initial pausing occurred near the dyad region of the positioned nucleosome, which contains the strongest histone-DNA interactions [10,30]. In 89% of the traces, helicase eventually exited the pause within the experimental time window of 150 s, and then proceeded at its initial speed, indicating the complete displacement of the nucleosome. As the helicase unwound further along the DNA, it paused again at locations initially lacking nucleosomes. These additional pauses suggest nucleosome transfer downstream from its original location. Analysis of the distance of the first transfer event revealed a distribution that was again in agreement with prediction by the DNA loop formation model (Methods; Figure. 2.3B). Thus, a simple passive mechanism is able to account for nucleosome transfer during fork progression, carried out either mechanically or by a motor protein.

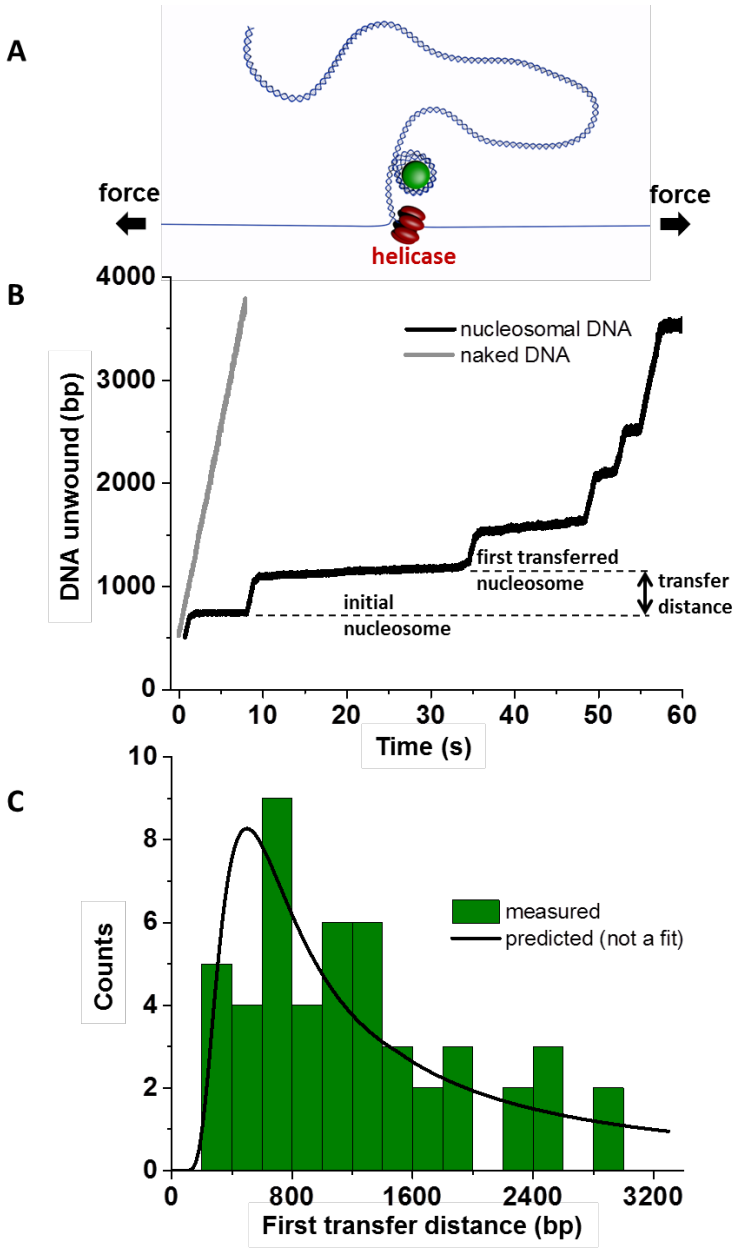

Figure. 2.7: Helicase displacement of a single nucleosome.

(A) Experimental configuration. A single dsDNA molecule was unwound by a T7 helicase as the two strands of the DNA were held under 12 pN of force by an optical trap, which assisted helicase unwinding but was insufficient to mechanically separate the dsDNA.

(B) A representative helicase unwinding trace. Helicase unwinding was interrupted by discrete pauses along the DNA template. Dashed lines indicate the dyad locations of the initial positioned nucleosome and the transferred nucleosome.

(C) Histogram of nucleosome transfer distance. A transfer distance was obtained from the first transfer event of each trace as indicated by the arrow in Figure. 2.6B. The histogram was obtained by pooling data from 49 traces. The prediction (not a fit) from the DNA looping model is plotted for comparison. The resulting Pearson test gives a reduced χ^2 of 0.31 with a *p*-value of 0.95 (Methods; Figure. 2.3B).

Nucleosome transfer to leading strand behind replication fork

During DNA replication, dsDNA available for nucleosome transfer is located behind the replication fork on the nascent daughter duplexes, which are poised to accept parental nucleosomes from ahead of the replication fork [20,31,32]. We hypothesize that if nucleosome transfer is dictated by DNA loop formation, transfer should take place on the upstream dsDNA, in a similar fashion as demonstrated for the downstream dsDNA. To investigate this hypothesis, we carried out leading strand replication using the T7 replisome to generate upstream dsDNA. The parental DNA template contained a single nucleosome with minimal naked DNA downstream (ahead) of the nucleosome (Figure 2.8A). In order to quantitatively assay the position of the transferred nucleosome, the 5'-end of the replicated leading strand was fluorescently labelled, and the replication product was subjected to exonuclease III digestion prior to being assayed by a denaturing gel (Figure 2.8B, replicates shown in Figure 2.10). The ssDNA resistant to digestion provided a quantitative measure for nucleosome position following DNA replication. The resulting distribution of the ssDNA length shows nucleosome transfer, peaked at 500-700 bp upstream of the initial nucleosome position. Although the measured transfer distance showed some sequence preference not accounted for by the loop formation model in its current simplest form, the overall features of the distribution are consistent with the model. Furthermore, the measured effect of competitor DNA on nucleosome transfer in these bulk replication assays is again well predicted by the DNA looping theory (Figure 2.9).

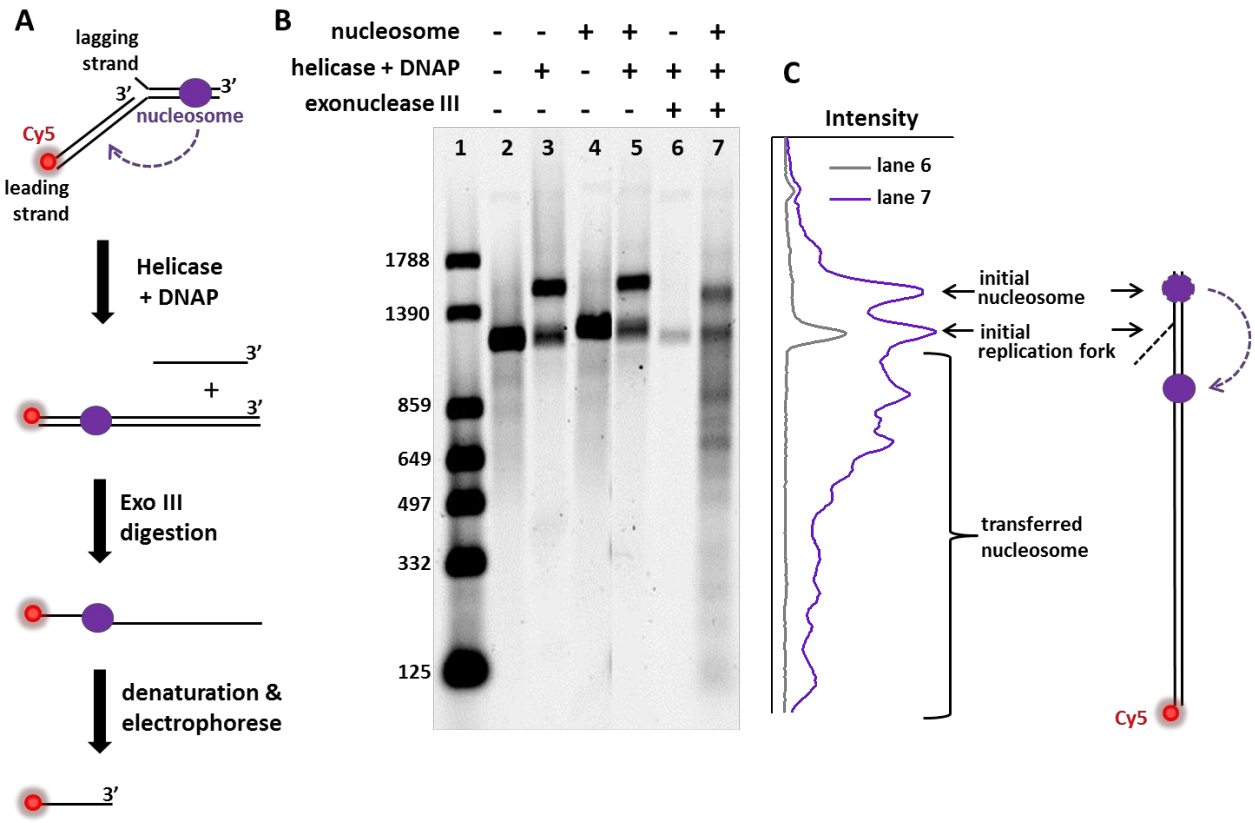

Figure. 2.8: Replisome displacement of a single nucleosome.

(A) Experimental configuration. Leading strand replication was carried out using the T7 replisome on a Cy-5 labeled parental template containing a single nucleosome with minimal dsDNA downstream.

(B) Nucleosome transfer after replication. The replication product was exonuclease III digested and assayed on a denaturing gel (lane 7). Lane 1 is a ladder and lanes 2-6 are control experiments. Lanes digested with exonuclease III were loaded with 5 times as much sample as the other lanes in order to achieve more accurate quantification.

(C) A line scan of lane 7 contained contributions from both the transferred nucleosome as well as background. In particular, a fraction of replisomes did not proceed past the nucleosome, and another fraction contained inactive replisome bound at the initial fork (see lane 6). The

background in lane 6 is removed from lane 7 during subsequent analysis. The template schematic right of the line scan explains some features of the band positions in the gel and the line scans.

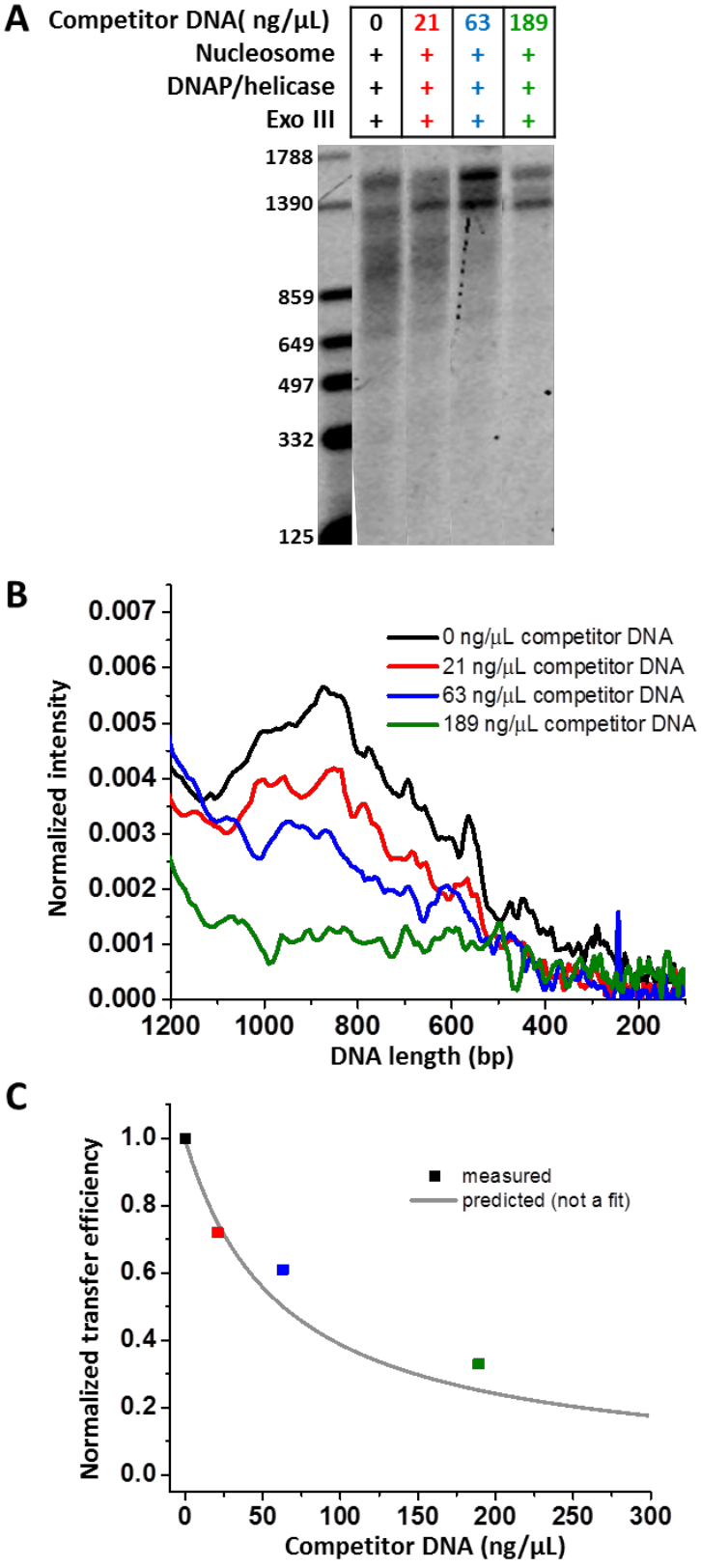
A
Competitor DNA(ng/μL)
Nucleosome
DNAP/helicase
Exo III
0
21
63
189
1788
1390
859
649
497
332
125
B
Normalized intensity
0.007
0.006
0.005
0.004
0.003
0.002
0.001
0.000
1200
1000
800
600
400
200
DNA length (bp)
0 ng/μL competitor DNA
21 ng/μL competitor DNA
63 ng/μL competitor DNA
189 ng/μL competitor DNA
C
Normalized transfer efficiency
1.0
0.8
0.6
0.4
0.2
0.0
0
50
100
150
200
250
300
Competitor DNA (ng/μL)
measured
predicted (not a fit)

Figure 2.9: Replication through a nucleosome in the presence of competitor DNA.

(A) Replication on a nucleosome template in the presence of increasing amounts of competitor DNA. The experiments were performed in the same fashion as those shown in Figure 2.7 except for the addition of competitor DNA. Exonuclease III digestion was used to footprint the transferred nucleosome, as described in the bulk replication section under Methods.

(B) Line scans of lanes in (A). Line scans were the background subtracted and normalized to the total amount of fully replicated DNA under each competitor DNA condition (data not shown).

(C) Normalized nucleosome transfer as a function of competitor DNA concentration. The measured normalized transfer frequency was calculated by integrating each line scan from 1200 bp to 100 bp (corresponding to 300 bp transfer distance to 1400 bp transfer distances) and normalizing it by that measured in the 0 ng μL^{-1} condition. The predicted transfer frequency was calculated as described in the competitor DNA section under Methods.

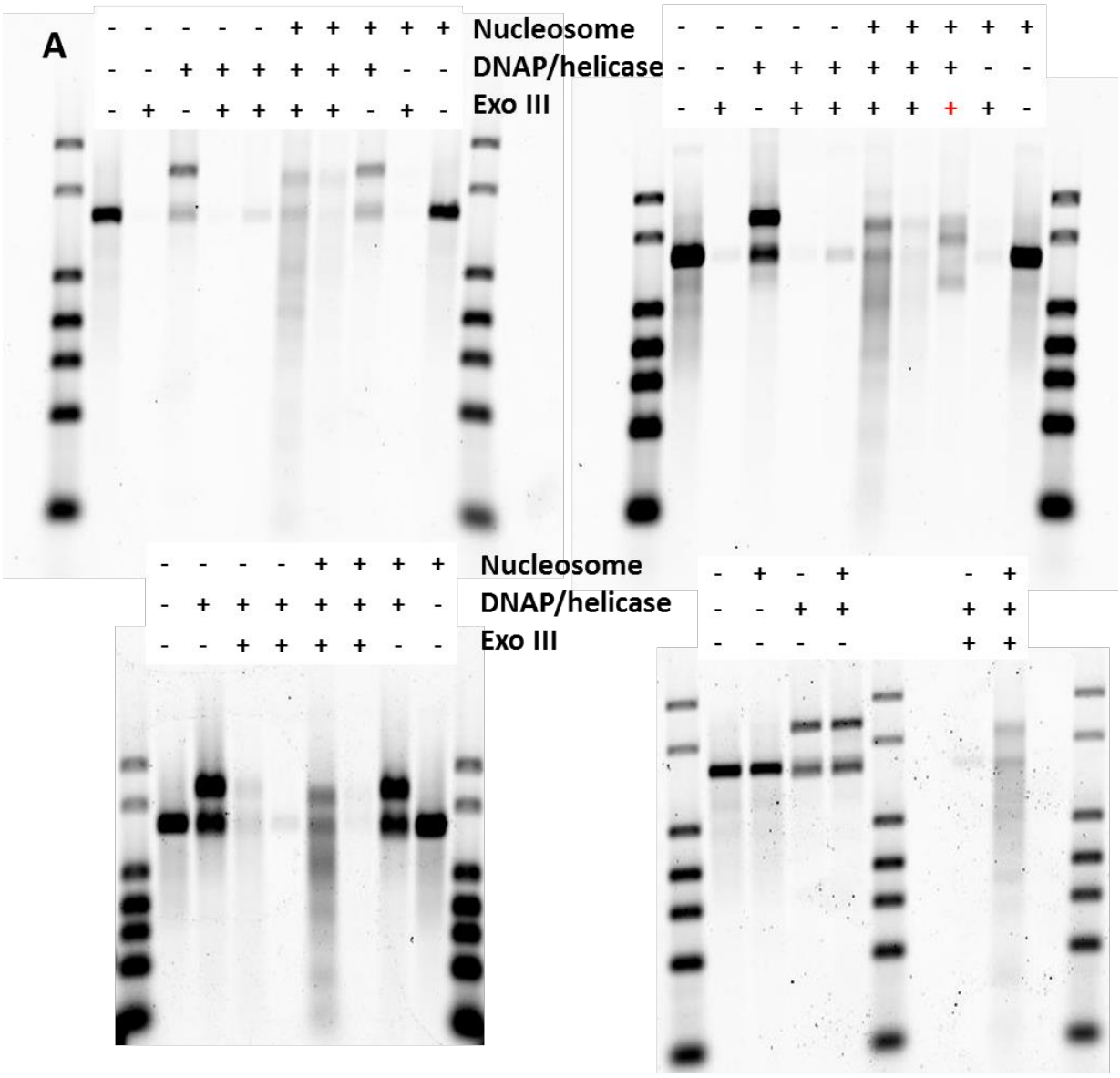
A
Nucleosome
DNAP/helicase
Exo III
Nucleosome
DNAP/helicase
Exo III
B
Probability density (bp-1)
0.0010
0.0008
0.0006
0.0004
0.0002
0.0000
-200
0
200
400
600
800
1000
1200
1400
Transfer distance (bp)
Upper Left
Upper Right
Lower Left
Lower Right

Figure 2.10: Additional replication gels for nucleosome transfer experiments**.**

(A) Additional replication gels for the nucleosome transfer experiment shown in Figure 2.7. The upper left panel shows the same replication gel as that for Figure 2.7, except that all lanes in the gel are included. Lanes shown in Figure 2.7 (from left to right) correspond to lanes 1, 2, 4, 11, 9, 6, and 7 in the full gel shown here. The remaining three gels are replicates. Unmarked lanes contain Cy5 labeled DNA ladders, with bands sized at 1788, 1390, 859, 649, 497, 332, and 125 bp, from top to bottom. Duplicate nucleosome/ replication/ exonuclease digestion lanes were loaded with equal (right) and 6-fold (left) amounts of DNA as the other lanes. Note that the red plus (+) over lane 8 in the upper right-hand gel indicates the accidental addition of exo-nuclease simultaneously with helicase and DNAP, this lane was excluded from all analysis.

(B) Nucleosome transfer distance distributions calculated from individual replicates shown in (A). The transfer distance distribution shown in Figure 2.11A is the average of the four replicates.

DISCUSSION

Taken together, results from these three distinct experimental approaches provide consistent support for passive nucleosome transfer by DNA loop formation (Figure 2.11A). As a nucleosome is displaced, it will be spontaneously transferred to available dsDNA, and this transfer is mediated by the formation of a DNA loop that bridges the nucleosome from its initial location to its new location (Figure 2.11B). Previous studies found nucleosomes remain associated with DNA during transcription after the passage of RNA polymerase [33,34]. Earlier studies with pol III suggested a loop of 80 bp[33]; whereas more recent work with pol II favors a "zero-size" DNA loop[35]. In contrast, for DNA replication, such small, or non-existent, loops are not consistent with previously measured *in vivo* distance scales[31,32,36].

Indeed, a number of *in vivo* and *in vitro* chromatin replication studies support key aspects of our looping model. DNA loop formation requires at least ~ 200 bp of free dsDNA to form a minimal DNA loop [22,37], consistent with the 200-600 bp of available naked nascent dsDNA present immediately upstream of the replication fork *in vivo* [20,31,32]. Additionally, parental nucleosomes have been shown to be located within approximately 400 bp of their original positions after the completion of the cell cycle [7,31,36], close to the most probable loop size. DNA loop formation may also be facilitated by the configuration [38] of nascent dsDNA strands as they emerge from the replisome which would contribute to the partitioning [19,39] of nucleosomes between the two daughter strands by coordinating nucleosome transfer with DNA synthesis[40].

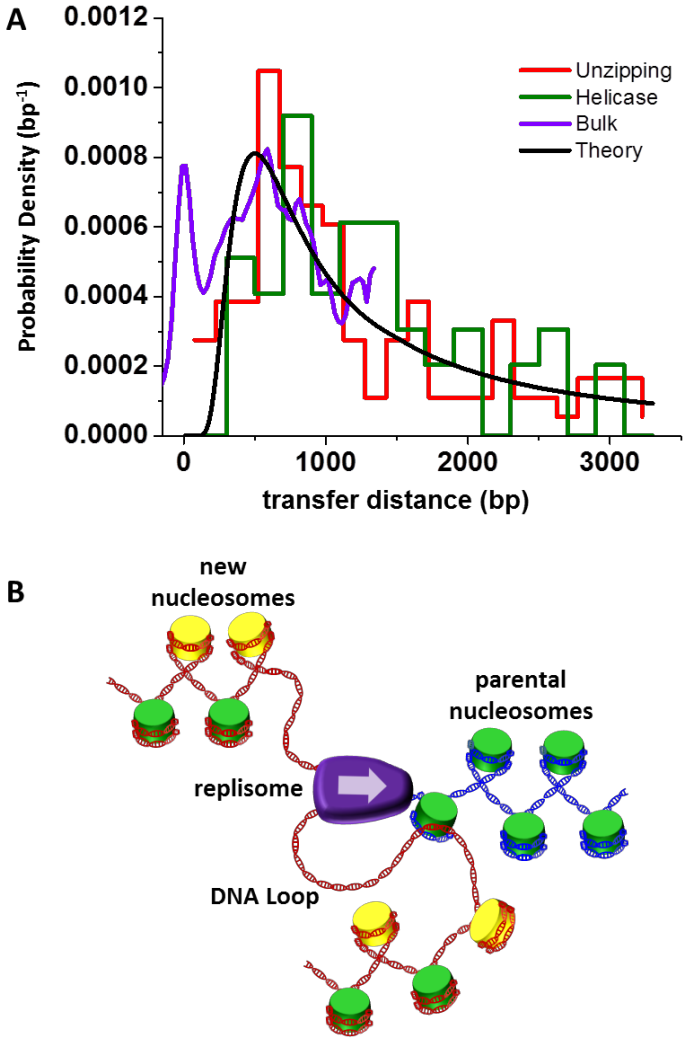

Figure 2.11: The passive nucleosome transfer model via DNA loop formation.

(A) Comparison of nucleosome transfer distance distributions as measured using three experimental approaches: mechanical fork progression (red; Figure 2.1C), helicase unwinding (green; Figure 2.6C), and leading strand replication (purple; Figure 2.10). Note that the peak near zero from the leading strand replication curve (purple) was background introduced by the fraction of reaction that did not proceed past the nucleosome as indicated in Figure 2.7. The prediction (black, not a fit) from the DNA looping model is also shown for comparison.

(B) A mechanistic model of passive nucleosome transfer mediated by DNA loop formation. When a replisome (purple) encounters a parental nucleosome (green) at the replication fork, a DNA loop forms in one of the daughter duplexes (red), bridging the nucleosome from its initial location to its new location and thus facilitating direct transfer to the daughter duplex. Nascent histones (yellow) are also deposited on the daughter strands by chaperones.

In vivo, passive transfer would only occur if there is sufficient available dsDNA to accept parental histones. Consistent with this requirement, overexpression of new histones or perturbation of chaperone function both result in replication fork stalling [9]. This implies that when daughter DNA is saturated with new histones, or new histones are not positioned properly, the parental nucleosome at the fork cannot be efficiently transferred and therefore becomes a substantial barrier for replication. Nascent histone deposition is likely coordinated with the transfer of parental nucleosomes, possibly by regulation of the deposition of new histones through a feedback mechanism involving the transfer of parental nucleosomes[6,41,42].

Although our model does not require specific interactions of histones with the replisome, recent studies have shown that histone H3 may interact with the eukaryotic helicase [43], providing insight into how replisome progression and histone dynamics may be coordinated[40]. However the action by which this potential intermediate transfers parental histones to the nascent DNA has yet to be elucidated and is still controversial[44]. The *in vivo* mechanism for nucleosome inheritance likely requires the coordination of many factors acting at, and around, the replication fork. These complex processes can take place on a simple platform dictated by DNA mechanics. The data presented here has quantified the ability of available DNA to facilitate the transfer of parental nucleosomes.

Our proposed model of passive parental nucleosome transfer via DNA loop formation describes a fundamental mechanism to facilitate parental nucleosome transfer while also permitting broader coordination for the deposition of new histones. DNA loop formation thus provides a

simple pathway that facilitates cellular complexity by exploiting fundamental physical properties.

REFERENCES

1. Kouzarides, T. Chromatin modifications and their function. *Cell* **128**, 693-705 (2007).
2. Ransom, M., Dennehey, B.K. & Tyler, J.K. Chaperoning histones during DNA replication and repair. *Cell* **140**, 183-95 (2010).
3. Gaydos, L.J., Wang, W. & Strome, S. Gene repression. H3K27me and PRC2 transmit a memory of repression across generations and during development. *Science* **345**, 1515-8 (2014).
4. Alabert, C. et al. Two distinct modes for propagation of histone PTMs across the cell cycle. *Genes Dev* **29**, 585-90 (2015).
5. Seale, R.L. Studies on the mode of segregation of histone nu bodies during replication in HeLa cells. *Cell* **9**, 423-9 (1976).
6. Osberg, B., Nuebler, J., Korber, P. & Gerland, U. Replication-guided nucleosome packing and nucleosome breathing expedite the formation of dense arrays. *Nucleic Acids Res* **42**, 13633-45 (2014).
7. Bonne-Andrea, C., Wong, M.L. & Alberts, B.M. In vitro replication through nucleosomes without histone displacement. *Nature* **343**, 719-26 (1990).
8. Randall, S.K. & Kelly, T.J. The fate of parental nucleosomes during SV40 DNA replication. *J Biol Chem* **267**, 14259-65 (1992).
9. Groth, A. et al. Regulation of replication fork progression through histone supply and demand. *Science* **318**, 1928-1931 (2007).
10. Hall, M.A. et al. High-resolution dynamic mapping of histone-DNA interactions in a nucleosome. *Nat Struct Mol Biol* **16**, 124-9 (2009).
11. Dechassa, M.L. et al. Structure and Scm3-mediated assembly of budding yeast centromeric nucleosomes. *Nat Commun* **2**, 313 (2011).
12. Shundrovsky, A., Smith, C.L., Lis, J.T., Peterson, C.L. & Wang, M.D. Probing SWI/SNF remodeling of the nucleosome by unzipping single DNA molecules. *Nat Struct Mol Biol* **13**, 549-54 (2006).
13. Li, M. et al. Dynamic regulation of transcription factors by nucleosome remodeling. *Elife* **4**(2015).
14. Li, M. & Wang, M.D. Unzipping single DNA molecules to study nucleosome structure and dynamics. *Methods Enzymol* **513**, 29-58 (2012).
15. Killian, J.L., Li, M., Sheinin, M.Y. & Wang, M.D. Recent advances in single molecule studies of nucleosomes. *Curr Opin Struct Biol* **22**, 80-7 (2012).
16. Kireeva, M.L. et al. Nucleosome remodeling induced by RNA polymerase II: loss of the H2A/H2B dimer during transcription. *Mol Cell* **9**, 541-52 (2002).
17. Rhee, H.S., Bataille, A.R., Zhang, L. & Pugh, B.F. Subnucleosomal structures and nucleosome asymmetry across a genome. *Cell* **159**, 1377-88 (2014).
18. Xu, M. et al. Partitioning of histone H3-H4 tetramers during DNA rpelication-dependent chromatin assembly. *Science* **328**(2010).
19. Jackson, V. Deposition of newly synthesized histones: hybrid nucleosomes are not tandemly arranged on daughter DNA strands. *Biochemistry* **27**, 2109-20 (1988).
20. Gruss, C., Wu, J., Koller, T. & Sogo, J.M. Disruption of the nucleosomes at the replication fork. *EMBO J* **12**, 4533-45 (1993).
21. Le, T.T. & Kim, H.D. Probing the elastic limit of DNA bending. *Nucleic Acids Res* **42**, 10786-94 (2014).

22. Shore, D., Langowski, J. & Baldwin, R.L. DNA flexibility studied by covalent closure of short fragments into circles. *Proc Natl Acad Sci U S A* **78**, 4833-7 (1981).
23. Peters, J.P., 3rd & Maher, L.J. DNA curvature and flexibility in vitro and in vivo. *Q Rev Biophys* **43**, 23-63 (2010).
24. Sankararaman, S. & Marko, J.F. Formation of loops in DNA under tension. *Phys Rev E Stat Nonlin Soft Matter Phys* **71**, 021911 (2005).
25. Geggier, S. & Vologodskii, A. Sequence dependence of DNA bending rigidity. *Proc Natl Acad Sci U S A* **107**, 15421-6 (2010).
26. Johnson, D.S., Bai, L., Smith, B.Y., Patel, S.S. & Wang, M.D. Single-molecule studies reveal dynamics of DNA unwinding by the ring-shaped T7 helicase. *Cell* **129**, 1299-309 (2007).
27. Sun, B. et al. ATP-induced helicase slippage reveals highly coordinated subunits. *Nature* **478**, 132-5 (2011).
28. Sun, B. et al. T7 replisome directly overcomes DNA damage. *Nat Commun* **6**, 10260 (2015).
29. Eggleston, A.K., O'Neill, T.E., Bradbury, E.M. & Kowalczykowski, S.C. Unwinding of nucleosomal DNA by a DNA helicase. *J Biol Chem* **270**, 2024-31 (1995).
30. Jin, J. et al. Synergistic action of RNA polymerases in overcoming the nucleosomal barrier. *Nat Struct Mol Biol* **17**, 745-52 (2010).
31. Lucchini, R., Wellinger, R.E. & Sogo, J.M. Nucleosome positioning at the replication fork. *EMBO J* **20**, 7294-302 (2001).
32. Gasser, R., Koller, T. & Sogo, J.M. The stability of nucleosomes at the replication fork. *Journal of Molecular Biology* **258**, 224-239 (1996).
33. Studitsky, V.M., Kassavetis, G.A., Geiduschek, E.P. & Felsenfeld, G. Mechanism of transcription through the nucleosome by eukaryotic RNA polymerase. *Science* **278**, 1960-3 (1997).
34. Hodges, C., Bintu, L., Lubkowska, L., Kashlev, M. & Bustamante, C. Nucleosomal fluctuations govern the transcription dynamics of RNA polymerase II. *Science* **325**, 626-8 (2009).
35. Kulaeva, O.I. et al. Mechanism of chromatin remodeling and recovery during passage of RNA polymerase II. *Nat Struct Mol Biol* **16**, 1272-8 (2009).
36. Radman-Livaja, M. et al. Patterns and mechanisms of ancestral histone protein inheritance in budding yeast. *PLoS Biol* **9**, e1001075 (2011).
37. Baumann, C.G., Smith, S.B., Bloomfield, V.A. & Bustamante, C. Ionic effects on the elasticity of single DNA molecules. *Proc Natl Acad Sci U S A* **94**, 6185-90 (1997).
38. Sun, J. et al. The architecture of a eukaryotic replisome. *Nat Struct Mol Biol* **22**, 976-82 (2015).
39. Tran, V., Lim, C., Xie, J. & Chen, X. Asymmetric division of Drosophila male germline stem cell shows asymmetric histone distribution. *Science* **338**, 679-82 (2012).
40. Smith, D.J. & Whitehouse, I. Intrinsic coupling of lagging-strand synthesis to chromatin assembly. *Nature* **483**, 434-8 (2012).
41. Ramachandran, S. & Henikoff, S. Transcriptional Regulators Compete with Nucleosomes Post-replication. *Cell* (2016).
42. Yadav, T. & Whitehouse, I. Replication-Coupled Nucleosome Assembly and Positioning by ATP-Dependent Chromatin-Remodeling Enzymes. *Cell Reports*.

43. Huang, H. et al. A unique binding mode enables MCM2 to chaperone histones H3-H4 at replication forks. *Nat Struct Mol Biol* **22**, 618-26 (2015).
44. Campos, E.I. et al. Analysis of the Histone H3.1 Interactome: A Suitable Chaperone for the Right Event. *Mol Cell* **60**, 697-709 (2015).
45. Schnitzler, G.R. Isolation of histones and nucleosome cores from mammalian cells. *Curr Protoc Mol Biol* **Chapter 21**, Unit 21 5 (2001).
46. Wolffe, A.P. & Ura, K. Transcription of dinucleosomal templates. *Methods* **12**, 10-9 (1997).
47. Lowary, P.T. & Widom, J. New DNA sequence rules for high affinity binding to histone octamer and sequence-directed nucleosome positioning. *J Mol Biol* **276**, 19-42 (1998).
48. Lee, K.M. & Narlikar, G. Assembly of nucleosomal templates by salt dialysis. *Curr Protoc Mol Biol* **Chapter 21**, Unit 21 6 (2001).
49. Brower-Toland, B. & Wang, M.D. Use of optical trapping techniques to study single-nucleosome dynamics. *Methods Enzymol* **376**, 62-72 (2004).
50. Patel, S.S., Rosenberg, A.H., Studier, F.W. & Johnson, K.A. Large scale purification and biochemical characterization of T7 primase/helicase proteins. Evidence for homodimer and heterodimer formation. *J Biol Chem* **267**, 15013-21 (1992).
51. Inman, J.T. et al. DNA Y structure: a versatile, multidimensional single molecule assay. *Nano Lett* **14**, 6475-80 (2014).
52. Egelman, E.H., Yu, X., Wild, R., Hingorani, M.M. & Patel, S.S. Bacteriophage T7 helicase/primase proteins form rings around single-stranded DNA that suggest a general structure for hexameric helicases. *Proc Natl Acad Sci U S A* **92**, 3869-73 (1995).
53. Patel, G. et al. A257T linker region mutant of T7 helicase-primase protein is defective in DNA loading and rescued by T7 DNA polymerase. *J Biol Chem* **286**, 20490-9 (2011).
54. Koch, S.J., Shundrovsky, A., Jantzen, B.C. & Wang, M.D. Probing protein-DNA interactions by unzipping a single DNA double helix. *Biophys J* **83**, 1098-105 (2002).
55. Gaillard, C. & Strauss, F. Ethanol precipitation of DNA with linear polyacrylamide as carrier. *Nucleic Acids Res* **18**, 378 (1990).
56. Jacobson, H. & Stockmayer, W.H. Intramolecular Reaction in Polycondensations .1. The Theory of Linear Systems. *Journal of Chemical Physics* **18**, 1600-1606 (1950).
57. Shimada, J. & Yamakawa, H. Ring-closure probabilities for twisted wormlike chains. Application to DNA. *Macromolecules* **17**, 689-698 (1984).
58. Becker, N.B., Rosa, A. & Everaers, R. The radial distribution function of worm-like chains. *Eur Phys J E Soft Matter* **32**, 53-69 (2010).
59. Hyeon, C. & Thirumalai, D. Kinetics of interior loop formation in semiflexible chains. *J Chem Phys* **124**, 104905 (2006).

CHAPTER 3

SINGLE MOELCULE STUDIES OF THE EUKARYOTIC REPLISOME

INTRODUCTION

Several decades ago genetic screens performed in yeast identified the MCM proteins (mini-chromosome maintenance) as initiators of DNA replication[1]. Since then, these MCM proteins have been characterized as the main proteins composing the hetero-heximeric helicase central to the eukaryotic replication machinery[2]. Early biochemical studies of the MCM 2-7 complex characterized it as a very weak helicase, initially raising doubts about its functionality within the replisome[3]. In fact, the MCM 2-7 complex was shown to barely unwind a stretch of 30 basepairs[4,5]. Curiously, a complex composed of MCMs 4, 6, and7 (two of each subunit) was a comparatively robust helicase[6], leading to the hypothesis that the other helicase subunits found in vivo function to negatively regulate helicase activity perhaps prohibiting unregulated helicase unwinding.

Such regulatory feature intrinsic to the MCM helicase complex would not be surprising given the multi-layered, cell-cycle dependent mechanism of helicase loading assembly required for replication initiation[7 8]. Briefly, a hetero-heximeric origin-recognition complex (ORC) binds to replication origins early in G1, recruiting the Cdc6 kinase to the origin[9]. Stepwise recruitment of MCM2-7 helicases is mediated by Cdt1, Cdc6, and ORC leading to the formation of a pre-Initiation Complex (pre-IC) composed of two MCM2-7 helicases[9,10]. Initially, MCM2-7 encircles dsDNA which is thought to enter the helicase through an opening between MCM-2 and -5[11]. Closure of this "gate" and the conversion of dsDNA into ssDNA within the helicase requires subsequent phosphorylation of MCM by the DDK kinase at the start of S-phase[9,12]. Concomitantly with the phosphorylation of MCM2-7, another kinase, CDK, drives the recruitment of Cdc45 to the pre-IC and the subsequent association of GINS, the leading-strand

polymerase-ε, and priming polymerase-α[9,13-15]. At this point, the replication complex is considered active however it still requires the lagging-stand polymerase-δ, MCM10, and a host of other proteins to escape the replication origin and become a processive replisome[13,16].

The central hub of this replisome is still the MCM2-7 complex, however the Cdc45 and GINS proteins are essential components of the active helicase and remain associated with the elongating replisome. Purification of this 11-subunit complex, termed CMG, produces a comparatively robust DNA helicase, now considered to be the complete eukaryotic helicase complex[17-19]. Upon this platform, the rest of the replication machinery as well as chromatin remodelers, histone chaperones, and topoisomerases are recruited to the DNA to drive duplication of the genome[20]. Characterizing how the CMG helicase interacts with the DNA to mediate the conversion of dsDNA into ssDNA will provide a baseline upon which to build a more complete understanding of DNA replication at the molecular level.

To build a more complete understanding of the inner workings of the eukaryotic replisome, I have taken a bottom-up approach to characterize the individual proteins that drive leading strand replication. Single-molecule manipulation of the CMG helicase has the potential to reveal unwinding rates, processivity, and step-size all of which would be the fundamental properties that drive replication fork progression. Incorporation of DNA polymerse-ε to build up leading-strand replication could then provide information into how the helicase and polymerase are coordinated at the replication fork. Comparison of these measured replication rates and processivity to that of the helicase alone and DNA polymerase alone would provide further insight into how these proteins work together to replication the genome. Such information would

be particularly interesting in the context of replication roadblocks; such as DNA lesions or nucleosomes, to answer how the replication machinery responds to such impediments. Within this chapter, I have laid out the initial experimental attempts to approach these goals.

MATERIALS AND METHODS

Protein Purification

Proteins were purified in Michael O'Donnell's lab at Rockefeller University according to the protocol published in Georgescu et al.[21] Briefly, the CMG protein used in these studies were purified from yeast expressing C-terminal Flag (x3) tagged Cdc45 and N-terminal His_6-kinase-tagged Mcm5. DNA polymerase-ε was purified from yeast using a N-terminal 3x-Flag-tag. RPA was purified from e. coli as described in Finkelstein et al.[22] Mcm10 was purified from e. coli using a maltose binding protein tag on the C-terminus which was cleaved off using the PreScission Protease.

DNA templates

All oligos were annealed in buffer containing 100 mM KAc and 30 mM Hepes pH 7.5 by floating annealing reaction in 500 mL of water which was brought to 95°C and then allowed to cool to room temperature. The "Arm2-adapter1-bio" template was used for EMSA, strand displacement, and TPM experiments. It was made by ligating, via an BstXI overhang, an anti-dig labelled 1.1kb PCR product to "adapter 2," composed of two oligos (IDT) LB_MCM_lower2_Sap1 and LB_MCM_upper2_BstXI. This ligation was gel purified and then annealed, this time heating only to 75°C, to the leading strand oligo: LB_CMG_Low1-3Bio (radiolabeled for the bulk assays). These "arms" were then ligated to a 764 bp PCR and a 2.9 kb

PCR product, in that order, via an AlwNI overhang and SapI overhang, respectively. This ligated template was used for the single molecule tracking experiments. For leading strand replication, a forked template was constructed by annealing four oligos together: LB_MCM_Upper1_BstEII, LB_CMG_Lower1A, and LB_CMG_Lower1B composed the primed leading strand and LB_MCM_lower2_Sap1 was the lagging strand. This template was then ligated to a PCR-ed 764 bp trunk via an AlwNI overhang. The primed leading strand was also annealed separately and used for primer extension assays.

For single molecule experiments performed without CMG, standard Y-arms were prepared as described previously[23]. For all single molecule experiments, each arm was ~1000 bp.

Radiolabelling oligos

For the bulk electomobility shift assay and strand displacement experiments, the 5'-end of LB_MCM_ lower1-3Bio was dephosporylated by rSAP (NEB). The enzyme was heat killed as directy by NEB, and a P^{32} phosphate group was transferred from ATP to the 5'-end by T4 PNK kinase (NEB). For the primer extension and leading strand replication the 5'-end of LB_MCM_Upper1_BstEII was radiolabeled.

CMG electromobility shift assay

1 nM of radiolabeled Arm2-adapter1-bio template was incubated with varying concentrations of CMG in 10 µL of Helicase Buffer (HB; 20 mM Tris pH 7.5, 5mM DTT, 40 µg/mL BSA, 0.1mM EDTA, 10mM $MgSO_4$, 20 mM KCl) at 30°C for 15 minutes. 2 µL of 50% glycerol was then added to the reactions and they were loaded on to a 4% native PAGE gel. The gels was run for 3

hours at 120 V at 4°C before being placed on filter paper, wrapped in plastic wrap, and exposed to a phosphor screen overnight. The phosporscreen was then imaged on a Typhoon 9400 and analyzed using ImageQuant (GE). Oligo sequences can be found in Table 3.1.

CMG strand displacement

0.5 nM of Arm2-adapter1-bio was mixed with 25 nM CMG with or without 50 nM Mcm10 in Helicase Buffer with 1 mM ATP. The reaction was conducted at 30°C and 10 uL was removed from the reaction at the time points indicated in the figure. The reaction were stopped through the addition of 2 µL of 5X stop buffer (100 mM EDTA, 25% glycerol, 0.5% SDS, 0.1% xylene cyanole, 0.1% bromophenol blue) and frozen in liquid nitrogen until all time points have been collected. The samples are then thawed and run on a 10% native PAGE, in 1X TBE, at room temperature, for 1 hour at 100 V. The gel was then placed on filter paper, wrapped in plastic wrap, and exposed to a phosphorscreen, overnight. The phosphorscreen is then imaged using a Typhoon 9400 and the image analyzed using ImageQuant (GE).

Tethered Particle Bead Tracking

The CMG helicase is first loaded on the leading strand by incubating 100 nM CMG with 5 nM Arm2-adapter1-bio in Helicase buffer (10 uL total reaction volume) at 30°C for 15 minutes, without ATP. During the CMG preloading, chambers were incubated with anti-FLAG at 0.2 mg/ml for 5 min, and then the surface was blocked by incubation with casein at 5 mg/ml for 5 min. The pre-incubation was then diluted with 10 µL Helicase Buffer with 10 µg/mL streptavidin and 1 mM ATP and flowed into the chamber for 5 min. Tethers are formed by anchoring CMG to the surface via a FLAG-tag on Cdc45. The lagging strand is then labelled

with 500 nm anti- digoxigenin-coated microspheres at 4 pM, which bound to the digoxigenin linkers on the DNA template. Finally, chambers were washed with Helicase Buffer + 4 mg/mL casein, without ATP, and then chambers were mounted on a Nikon TiE inverted microscope. Using custom Labview bead tracking software, at least 100 tethers are selected over at least 5 fields of view. Beads were tracked at 300 frames/second for 10 seconds prior to the addition of 20 μL of reaction buffer (HB with 10 mM ATP or AMPPNP with or without 100 nM Mcm10). Ten seconds of bead tracking is collected immediately following addition of reaction buffer and then at 5, 10, 15, 20, and 30 minutes.

Experiments were performed at room temperature (24°C).

The tether length is then analyzed by calculating the x-y variance of the bead position and using a look-up table of DNA lengths to convert to tether length using custom Labview analysis software. Only tethers that were 1 kb in length were then followed over each time point, if the bead disappeared and was no longer tracked, it was counted as a bead displacement event.

Single molecule tracking

Tethering CMG to the surface is done as described above, for experiments where force is applied to the lagging strand. For experiments were force is applied to the leading strand, a 4kb length of DNA labelled at both ends with biotin is incubated prior to the addition of streptavidin coated beads (done with the same concentration as the anti-dig beads).

Experiments done without CMG were performed by anchoring the DNA template directly to the chamber surface. Briefly, chambers were first incubated with anti-digoxygenin at 0.2 mg/ml for

5 min, and then the surface was blocked by incubation with casein at 5 mg/ml for 5 min. Then DNA templates were flowed into the chamber at 100 pM for 5 min. This was followed by incubation with 500 nm streptavidin-coated microspheres at 4 pM, which bound to the biotin linkers on the DNA template. Finally, chambers were washed with helicase buffer and 2mg/mL casein and the following proteins as indicated: 200 nM Mcm10, 20 nM pol-ε or T7 gp5 (NEB) with 625 nM dNTPs, 200 nM RPA.

Experiments were performed at room temperature (24°C).

Tether manipulation

CMG

The tether was stretched to 12 pN and then held at a constant force of 10 pN for up to 120 s. If the tether lasts the full 120 s it is then mechanically unzipped at 10 pN/s.

Mcm10

First, approximately 400 bp of dsDNA were mechanically unzipped, at a constant velocity of 200 nm/s for 2 seconds, to produce a ssDNA loading region for Mcm10. The tether is then rezipped at -50 nm/s (trap moves backward towards its starting position) until the force drops below 2 pN. Then the tether is unzipped completely at 200 nm/s.

Pol-ε and T7 gp5

For live tracking, approximately 400 bp of dsDNA were mechanically unzipped, at a constant velocity of 200 nm s^{-1} for 2 seconds, to produce a ssDNA loading region for helicase. The tether was held at a constant position for up to 30 s for helicase loading to occur, if loading did not

occur within this time frame, the tether was released and a new tether was selected. If the force dropped below 10 pN, owing to polymerase loading and translocation to the fork junction, the tether was then held at a constant force of 12 pN for up to 15 s.

For assaying extent of polymerization, approximately 400 bp of dsDNA were mechanically unzipped, at a constant velocity of 200 nm/s for 2 seconds, to produce a ssDNA loading region for Mcm10. The tether is then rezipped at -50 nm/s (trap moves backward towards its starting position) until the force drops below 2 pN. Then the tether is unzipped completely at 200 nm/s.

RPA

For assaying RPA stability on ssDNA, approximately 400 bp of dsDNA were mechanically unzipped, at a constant velocity of 200 nm/s for 2 seconds, to produce a ssDNA loading region for RPA. The tether is then rezipped at -50 nm/s (trap moves backward towards its starting position) until the force drops below 2 pN. Then the tether is unzipped completely at 200 nm/s.

Leading strand replication

Three templates were used for leading strand replication, the construction of which was described above. 1 nM of DNA template was incubated in Helicase Buffer with 100 μM dNTPs and 5 mM ATP, as indicated, with 10 nM pol-ε, and 40 nM CMG. CMG is added first to the reaction and incubated with the DNA for 10 minutes at 30°C and then the rest of the proteins were added and the reactions were incubated at 30°C for 20 minutes. Reactions were stopped with 2 μL of stop/loading buffer (90% formamide, 20 mM EDTA, 0.1% bromophenol blue and xylene cyanole) and then heated to 95° for 10 minutes. Samples are then spun down and loaded onto a 5% denaturing PAGE, run for ~2.5 hours, at room temperature, in 1X TBE, at 50 V.

Oligo name	**sequence**
LB_MCM_lower2_Sap1	/5Phos/GTC CAA CAA GTG AGG TAG AGT CCT TTT TTT TTT TTT TTT TTT TTT TTT TTT TTT TTT TTT TTT TTT TTT TTT TTT TTT TTG ACG CTG TTC AGT TCT GGC TTG CTA CGA CAT CTA
LB_CMG_Low1-3Bio	/5Phos/ATG TCG TAG CAA GCC AGA ACT GAA CAG CGT CTT TTT TTT TTT TTT TTT TTT TTT TTT TTT TTT TTT TTT TTT TTT T/3Bio/
LB_MCM_upper2_BstXI	GGA CTC TAC CTC ACT TGT TGG ACA CGC
LB_MCM_Upper1_BstEII	/5Phos/GTC ACA CTA GAC TAG GTC GTA CTG AGG
LB_CMG_Lower1A	/5Phos/ATG TCG TAG CAA GCC AGA ACT GAA CAG CGT CTT TTT TTT TTT TTT TTT TTT TTT TTT TTT CCT CAG TAC GAC
LB_CMG_Lower1B	/5Phos/CTA GTC TAG TGT GAC TTT TTT TTT TTT TTT TTT TTT TTT TT*T* T*T*T

Table 3.1: oligos makes and sequences used to make fork junctions for eukaryotic replication proteins

RESULTS

CMG interacts extensively with the lagging strand

In vivo, The MCM helicase is loaded onto double strand DNA by the ORC complex[7,9]. Through the recruitment of additional proteins, Cdc45 and GINS, the Mcm2-7 helicase and bound DNA is remodeled such that the active CMG helicase is able to translocate 3'- to 5'- along the leading strand[5,24-26]. The remodeling process is largely unknown as intermediates have yet to be trapped and characterized[27,28]. The currently working model is based on the high-resolution crystal structure of the Mcm double hexamer[29]. The double heximers interact with each other through protein-protein interactions, which remain intact at the time of helicase activation by accessory proteins (most likely Cdc45, GINS, and Mcm10)[12,29]. Helicase activation prior to separation of the heximers would cause local melting on the DNA as the two helicase start to engage with the phosphate backbone and draw the DNA into the central channel[29-31]. Catching of the locally melted DNA by internal sensors and hairpins could further drive remodeling of the CMG helicase and extrusion of the lagging stand through the MCM 2/5 gate[32]. At this point the double heximers could disengage from each other making space for the loading of the DNA polymerases[31]. How the active CMG helicase interacts with DNA would provide insight into the mechanistic underpinnings of replisome architecture, strand separation, and how various roadblocks and DNA damage may effect helicase progression. High resolution tracking of CMG helicase unwinding is possible using an optical trap and provides a direct measurement of helicase-DNA interactions, unwinding rates, and processivity[33,34].

In an effort to simplify working with the eukaryotic replisome, we have chosen to skip the ORC-mediated loading steps and instead load the CMG helicase on a forked DNA template. For

efficient helicase loading the 3'-end of the fork must be available presumably to thread through the central channel of the helicase[5,26,35]. While it is possible to load the purified CMG helicase onto a forked template where the 3'-end is blocked by streptavidin[35], the efficiency is very low suggesting that such a loading scheme is selecting for helicase complexes where the Mcm2/5 gate is not completely closed (communication with Lance Langston). Weather this is selecting for the "proper" configuration of the CMG helicase is unclear. Crystal structure data seems to suggest that first half of the inner channel is large enough to accommodate dsDNA suggesting that perhaps the unwinding is mediated by an internal plough-share type mechanism[29,35].

Alternatively, a strand-exclusion model where the lagging strand is completely excluded from the helicase has been supported by several experiments[5,24,36,37]. The initial characterization of strand translocation used a strand specific streptavidin block, which was found to only be an effective block when placed on the leading strand[24]. This set of data set the precedent for future experimental configurations, where it has been taken for fact that the lagging strand is completely excluded from the helicase. This would indicate that the unwinding mechanism may be more akin to prokaryotic helicase like that from T7 bacteriophage[38]. However, FRET studies have indicated that the lagging strand makes extensive contacts with the exterior of the helicase which may play a role in strand separation[37]. Early studies support the importance for these contacts as unwinding template lacking a lagging strand flap are less efficiently unwound although binding is minimally effected[5,6]. The addition of a long dsDNA lagging strand at the replication fork has minimal effect on the Kd of CMG binding to the template (Figure 3.1), as compaired to previously published results[39]. This indicates that the dsDNA is not inhibiting the

ability of CMG to find the fork and is probably not sequestered in non-specific binding to the dsDNA.

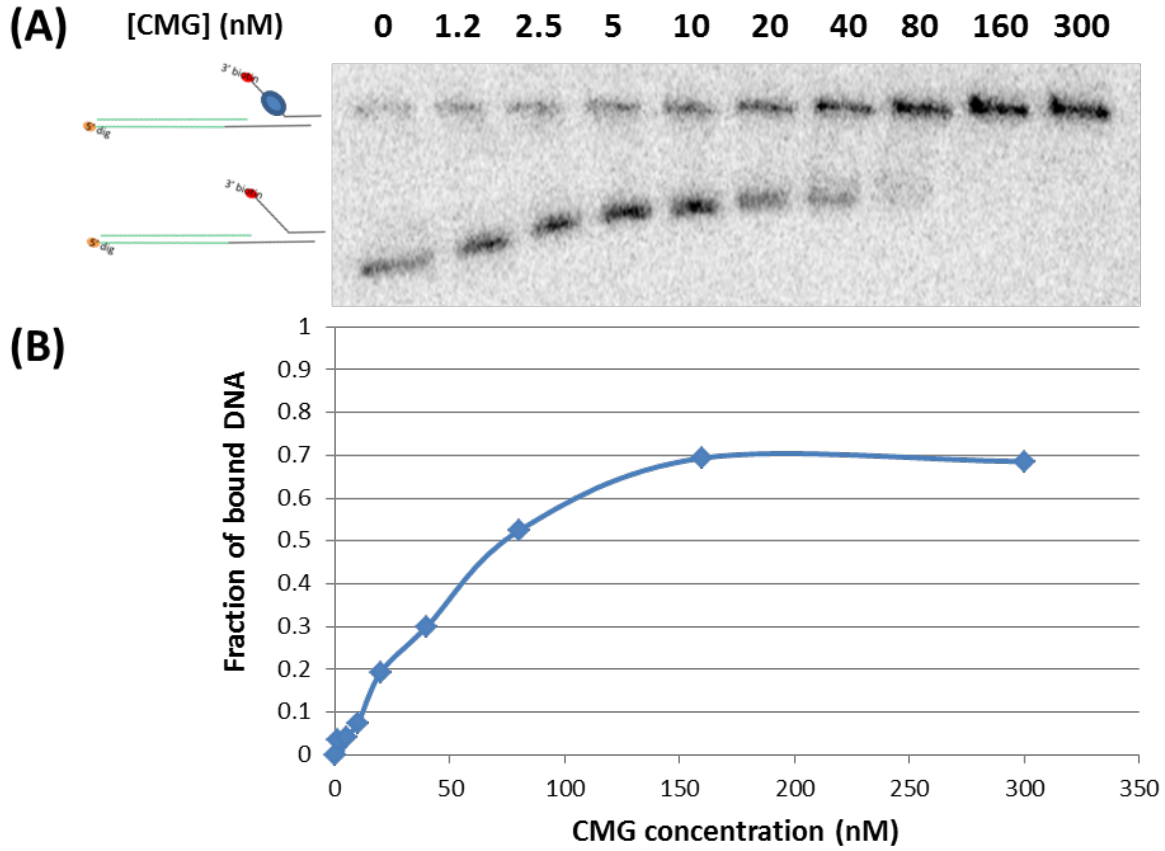

Figure 3.1: CMG loads efficiently on a forked template with a 1kb arm (for tethering) as assayed by electro-mobility shift assay (EMSA). (A) Image of radioactive EMSA reaction products, schematic on the left of gel image. CMG concentration indicated along the top of the gel. (B) Quantification of the fraction of shifted DNA, using the no CMG condition as the baseline.

Recent EM studies of CMG loaded on a fork template have produced preliminary data that suggests that the dsDNA ahead of the helicase is clamped within the entrance of the central pore[10,29,40]. This counters previous investigations that suggested that the inner channel of the helicase doesn't interact with dsDNA[24], however given the ever changing conditions under which the CMG helicase is studied (whole cell extracts and purified systems) it is not surprising that there would be variable results. Interestingly, the extent to which CMG helicase interacts with the lagging strand appear to be ATP-dependent alluding to the possibility that these interactions may be meaningful in mediating efficient strand separation[40] as assayed using single molecule DNA unzipping (Figure 3.2).

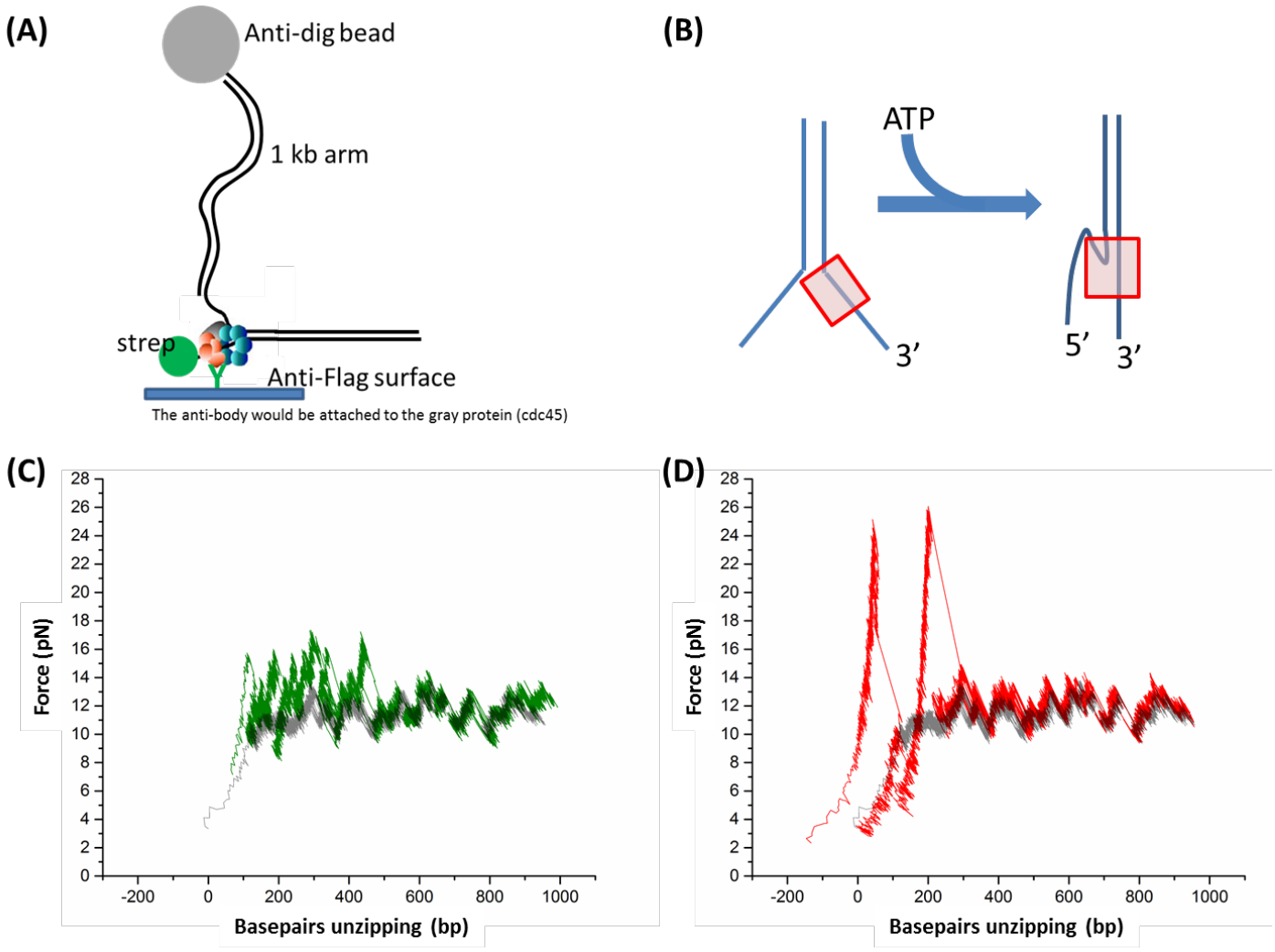

Figure 3.2: ATP binding of CMG changes engagement with the lagging strand. (A) Experimental configuration: CMG helicase is anchored to the surface through Cdc45 via an anti-Flag attachment to the coverslip surface. The downstream segment of DNA is approximately 800 bp long. (B) Model for lagging strand engagement, based on communications with the O'Donnell lab. (C) Unzipping signature in the absence of ATP. (D) Unzipping signature in the presence of 10 mM ATP.

It is interesting to note that even in the presence of ATP, when strand separation by CMG should have occurred; there was no measurement of helicase translocation. Unpublished data from the O'Donnell lab indicated that the CMG helicase is unable to unwind more than 100 bp of DNA in bulk strand displacement reactions. Their interpretation is that CMG can invade the duplex DNA and then stalls, probably when the DNA duplex reforms behind the helicase. In my unzipping experiments, stalling of the helicase within the duplex DNA would be measured as a change in the position of the helicase force signature with respect to the underlying DNA sequence. However, all of the unzipping traces taken in the presence of ATP have a force signature at the very start of the DNA tether and no change in the position was measured over time (Figure 3.2D). This could indicate that CMG is not unwinding the DNA under these single molecule conditions or that this configuration isn't compatible with measuring CMG unwinding or position. This later possibility may be use to the fact that the DNA is anchored to the coverslip surface via the helicase, which

CMG helicase requires Mcm10 for processive unwinding

Bulk unwinding assays clearly indicate that strand displacement by CMG is very inefficient (Figure 3.3). Interestingly, the low unwinding efficiency has plagued biochemical work on eukaryotic helicases for decades. Initially, the MCM helicase was purified in two distinct configurations; the Mcm 4/6/7 heximer and the Mcm2-7 heximer[5,6]. It was immediately noted that the 4/6/7 complex was far more efficient at strand separation than the in vivo configuration of the Mcm 2-7 heximer[6]. This suggests that the additional subunits may function to inhibit or slow DNA unwinding, the mechanistic advantage of which is yet unknown[38,41].

The addition of Cdc45 and GINS to the helicase complex increased binding efficiency and longevity on the DNA as well as increasing strand separation efficiency over the Mcm2-7 helicase[3,11,13,17,25]. However, the unwinding efficiency is still very low (Figure 3.3B) and the time scale is excessive given that S-phase is completed in about 2 hours on average[8]. A logical assumption would be that the highly purified CMG helicase may not function properly without the presence of the other replisome components.

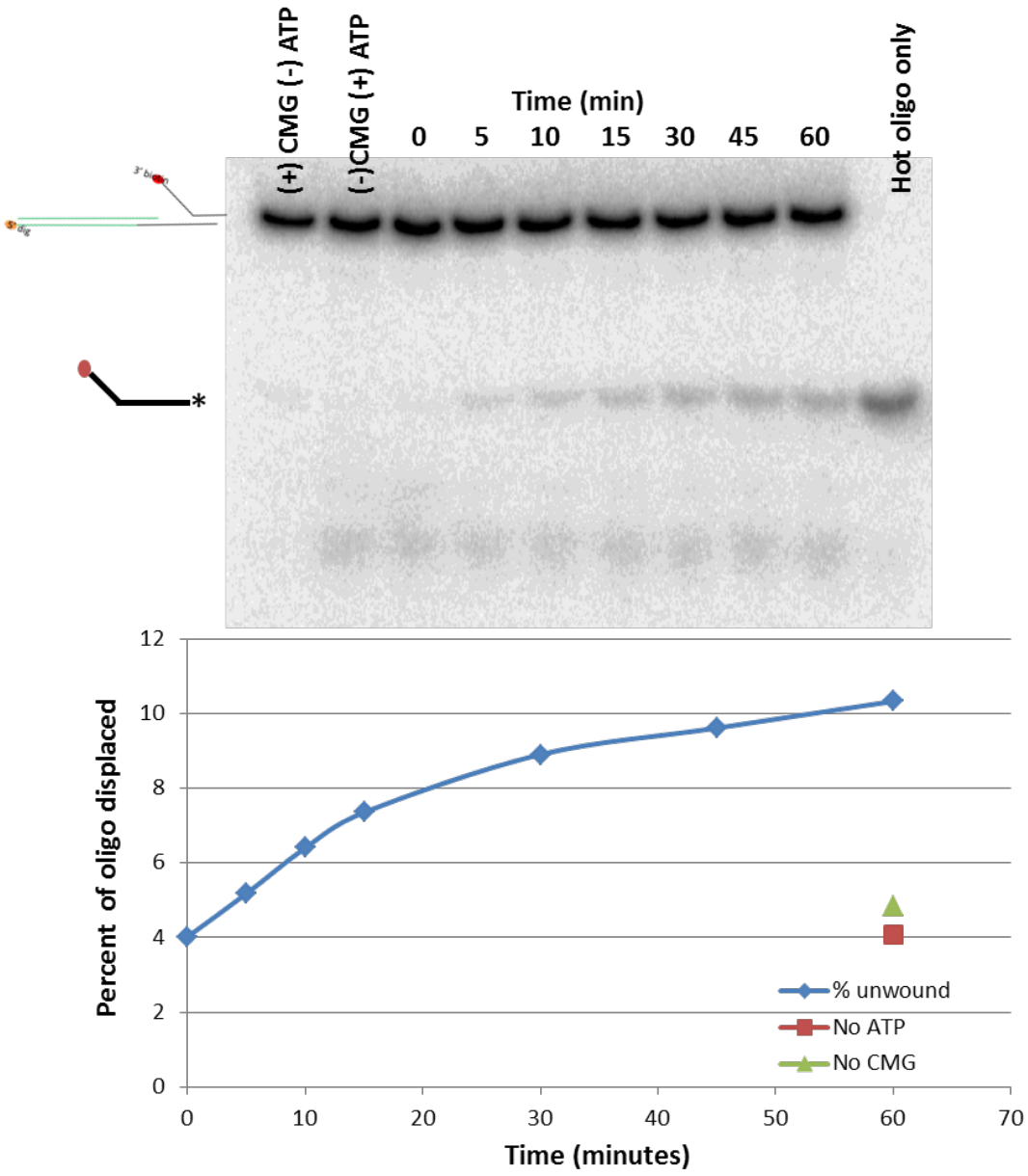

Figure 3.3: Strand displacement by 50 nM of CMG. (A) Image of radioactive gel with template schematic on the left and time points along the top. (B) Quantification of the percentage of displaced leading strand.

One accessory protein shown to associate with CMG helicase is Mcm10[16,42,43]. Early purifications of CMG helicase were, perhaps, not as clean as later, more optimized, purifications where the Mcm10 protein was effectively removed (communications with Lance Langston), this could explain the high unwinding efficiency of the early CMG purifications that was initially reported[21]. With this increased purity in the protein preparations, the addition of Mcm10 to the reactions significantly increases strand displacement efficiency as well as the time scale over which unwinding occurs (Figure 3.4). In the absence of Mcm10, CMG takes an hour to reach 10% strand displacement (Figure 3.3B). The addition of Mcm10 greatly increases strand displacement activity of CMG; reaching over 50% in just over a minute (Figure 3.4 B). These findings indicate that Mcm10 may be playing a dual role in both helicase loading as well as effective strand engagement and unwinding.

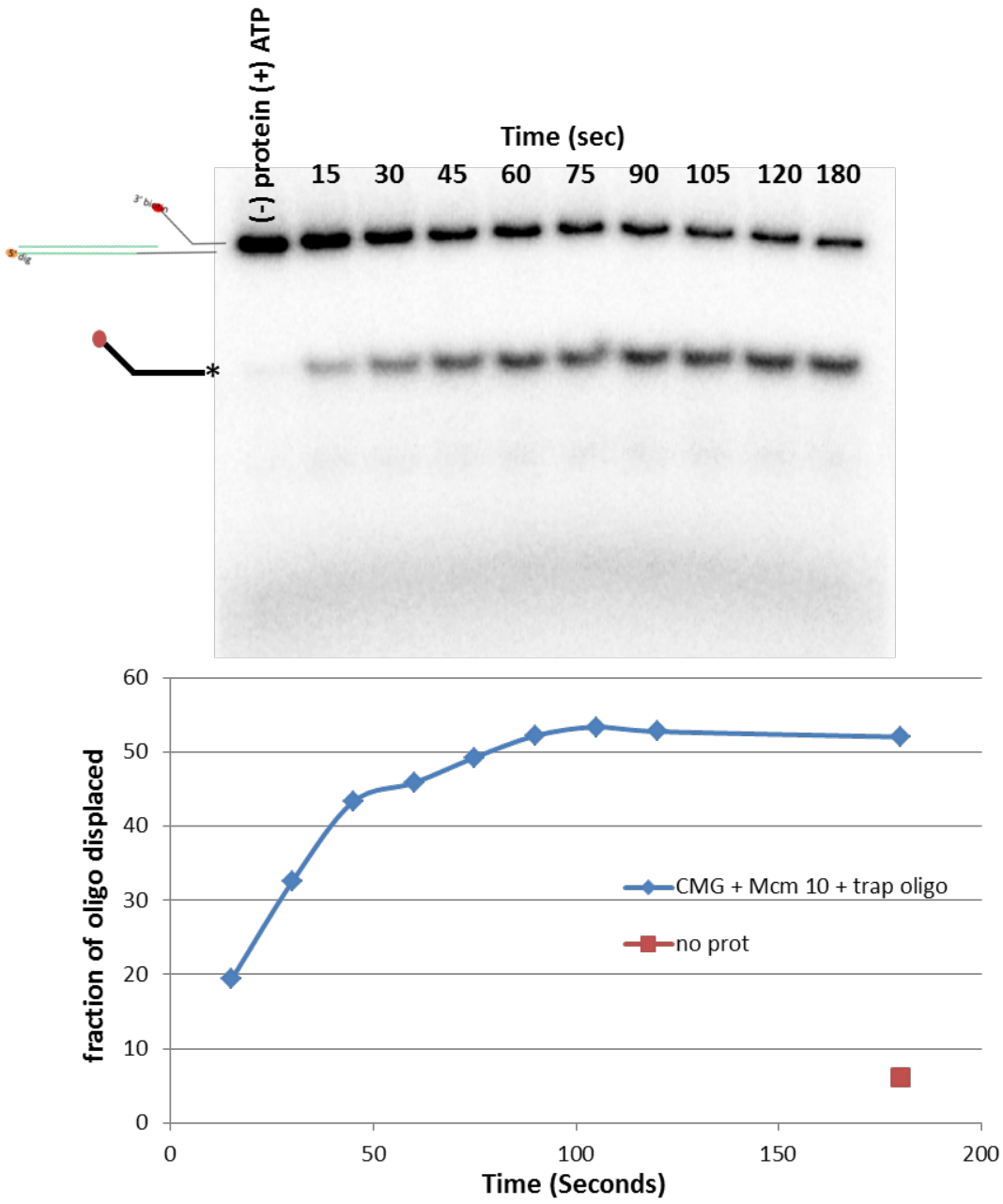

Figure 3.4: Strand displacement by 50 nM of CMG and 100 nM Mcm10. (A) Image of radioactive gel with template schematic on the left and time points along the top. (B) Quantification of the percentage of displaced leading strand.

To attempt to differentiate the effect of Mcm10 on helicase loading from a general increase in unwinding speed single molecule bead tracking was implemented. In the tethered molecule configuration, CMG is tethered to the surface via the Flap-tag on Cdc45 and then the 3'-end is blocked by streptavidin to inhibit tether dissociation. Any free CMG is then washed from the chamber thus eliminating the possibility for helicase reloading and providing a method to assay a single turn-over event of the helicase. The immediate increase in strand displacement with the additional of Mcm10, over the condition without Mcm10, indicates that Mcm10 may play a primary role in engaging CMG with the DNA to mediate processive unwinding. One potential model is that CMG stutters at the fork, not fully engaged with the fork and thus unable to process forward (communications with Lance Langston). While the total strand displacement with Mcm10 does not reach that of the bulk experiments, this may be due to the known affinity of Mcm10 for dsDNA[44] which could reduce the efficiency of Mcm10 to find CMG at the fork. It could also indicate that one of the primary ways that Mcm10 is acting to drive highly efficient strand displacement in bulk assays is by speeding unwinding thus allowing each helicase to catalyze many more reactions than helicase alone.

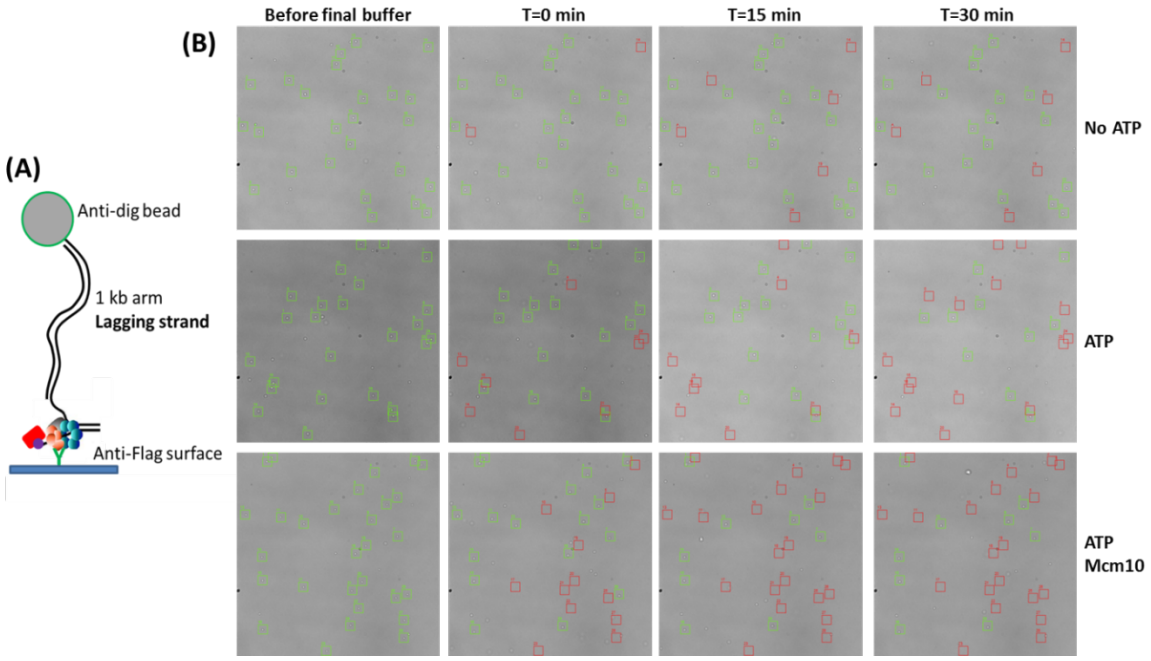

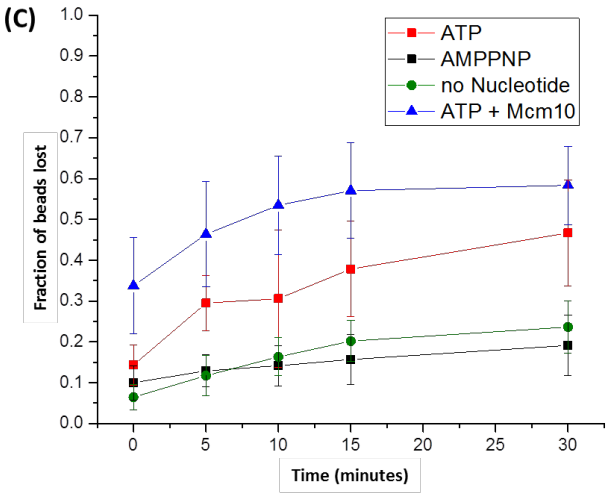

Figure 3.5: Tethered particle tracking of bead displacement. (A) Experimental configuration. (B) Still images of a single field of view of tethers; green boxes indicate beads that are actively being tracked and red boxes indicate failed bead tracking due to the loss of the bead from the tether. (C) Quantification of displaced beads over time, error bars indicate standard error of the mean over replicate experiments.

Unfortunately, CMG unwinding could not be detected under force using an optical trap using a similar configuration as in the tethered particle tracking experiments (Figure 3.6), the only difference being a ligation of approximately 800 bp of DNA in front of the helicase. For live tracking of the helicase, an optical trap was used to hold the attached bead under a constant force to prevent reannealing of the DNA behind the helicase and allow live-tracking of the fork position over time. As a helicase converts dsDNA to ssDNA, the length of the DNA between the bead and the helicase will increase over time. Measurements of base-pairs unwound over time in the presence of non-hydrolyzable ATP-analog (AMPPNP) were indistinguishable from that measured in the presence of ATP, indicating that the DNA unwinding was not measured (Figure 3.6 C). It is curious that the bead displacement assay shows clear helicase activity as measured by the loss of beads over time (Figure 3.5). Could the addition of a long segment of DNA be inhibiting CMG unwinding in some way? Perhaps the addition of force along the DNA somehow changes how the helicase interacts with the DNA template, inhibiting unwinding in some way. Another possible explanation is that CMG has invaded the dsDNA but stalls due to the reannealing of the DNA behind the helicase (Figure 3.7). If this happens, there would be no way to measure the position of the helicase it is no longer located at the fork junction of the DNA template and therefore any helicase unwinding could not be measured.

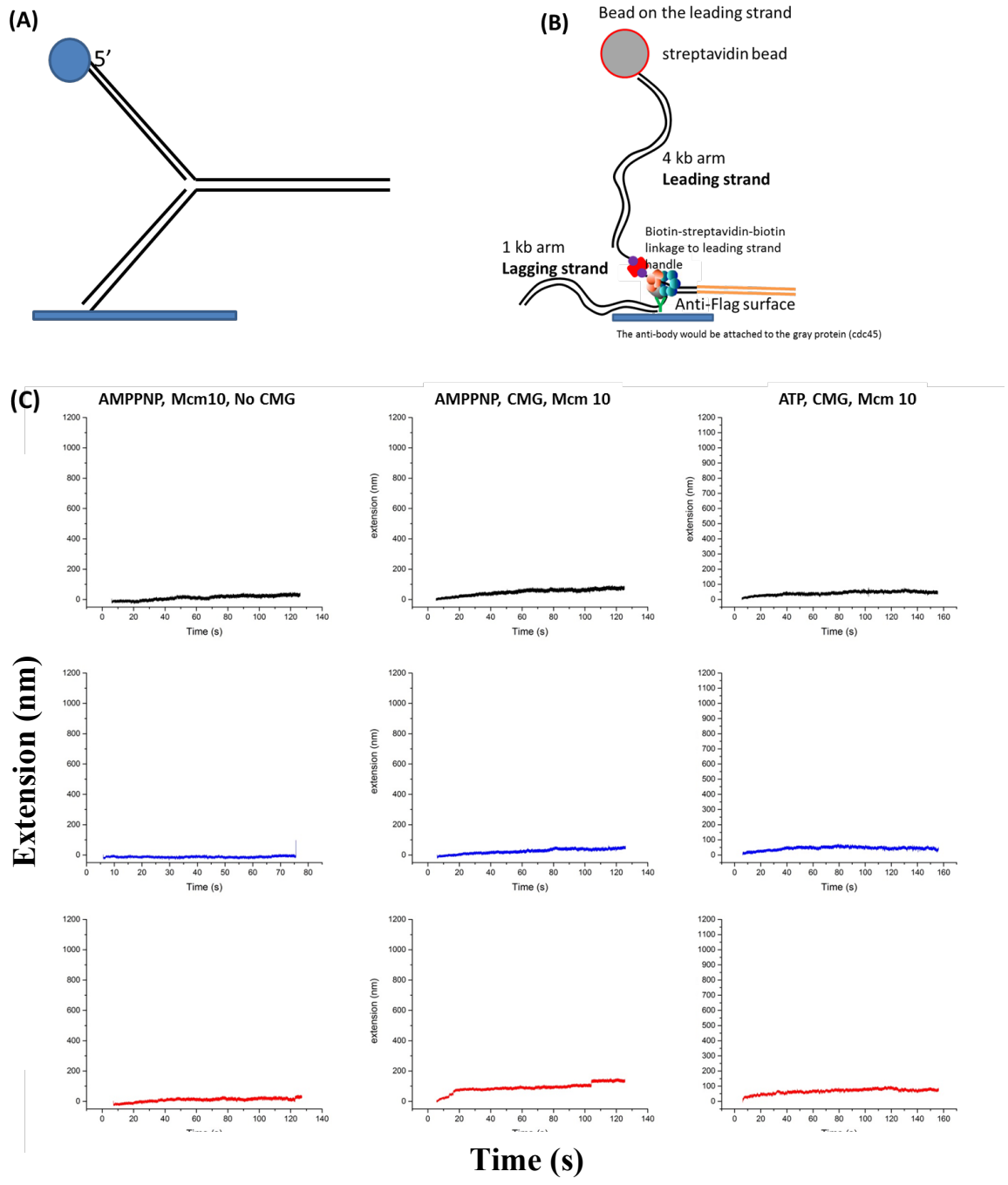

Figure 3.6: Real time tracking of CMG unwinding using an optical trap. (A) Experimental configuration for the "no CMG" configuration. (B) Experimental configuration for CMG tracking. (C) Example traces under three different experimental conditions as indicated, plotted as tether extension verses time. Length of the Y-arms has been subtracted from the

extension, such that zero corresponds to no dsDNA unwound rather than total tether extension.

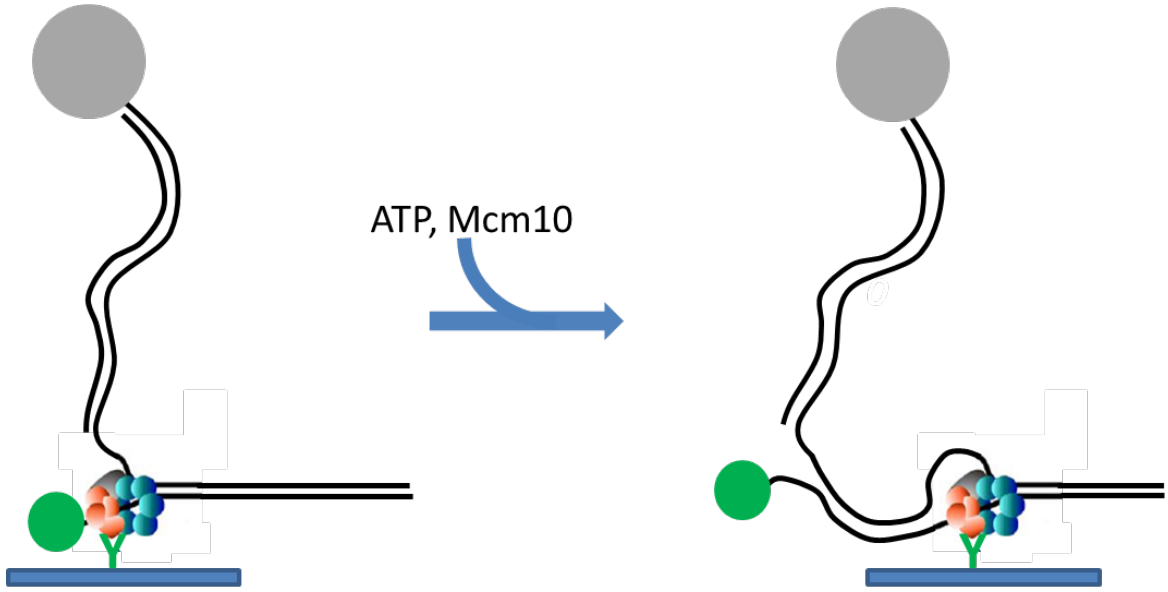

Figure 3.7: Possible result of CMG unwinding an 800 bp template when the helicase is anchored to the surface. With the addition of ATP (and Mcm10) the helicase invades the dsDNA and then stalls due to the reannealing of the DNA behind the helicase. When the bead is then held at a constant force, the position of the fork-junction rather than the helicase position is being measured.

Mcm10 interacts with ssDNA and can drive oligo annealing (in bulk).

The in vivo function for Mcm10 is not fully understood, although it has been found to interact with several replication structures[45,46]. Initially it was found to associate with the pre-initiation complex prior to double hexamer separation where it seems to drive this event[16]. Among its many new functional aspects, Mcm10 had been found to play a role in chromosome condensation[47], to recruit DNA polymerase-α to replication forks and may remain there to stabilize this polymerase within the replisome[48] (Zhu et al. Gene Dev 2007). Recently, the ability for Mcm10 to stimulate CMG activity has been characterized suggesting that it may also act as a general processivity factor for the helicase and replisome in general[16,42,46].

Under both bulk and single molecule conditions, the ability for Mcm10 to interact with exposed ssDNA is significant (Figure 3.7 and Figure 3.8)[49]. In solution Mcm10 facilitates the annealing of two separate oligos in a highly efficient manner (Figure 3.8). This protein is known to bind ssDNA and form higher order structures[50,51]. In the bulk assays there is an initial super-shift indicating that Mcm10 has bound the oligo as an initial intermediate to the reannealing. Perhaps, Mcm10 binds to the ssDNA, dimerize, and through this dimerization brings the two oligos together facilitating basepairing. Weather Mcm10 forms a filament along the oligo to bring the two strands together seems unlikely as that would be detected as a large smear on the gel. However, the translocation of Mcm10 along ssDNA has been suggested in previous studies[50,51] perhaps functioning at the fork and facilitating incremental annealing of the two strands (Figure 3.9).

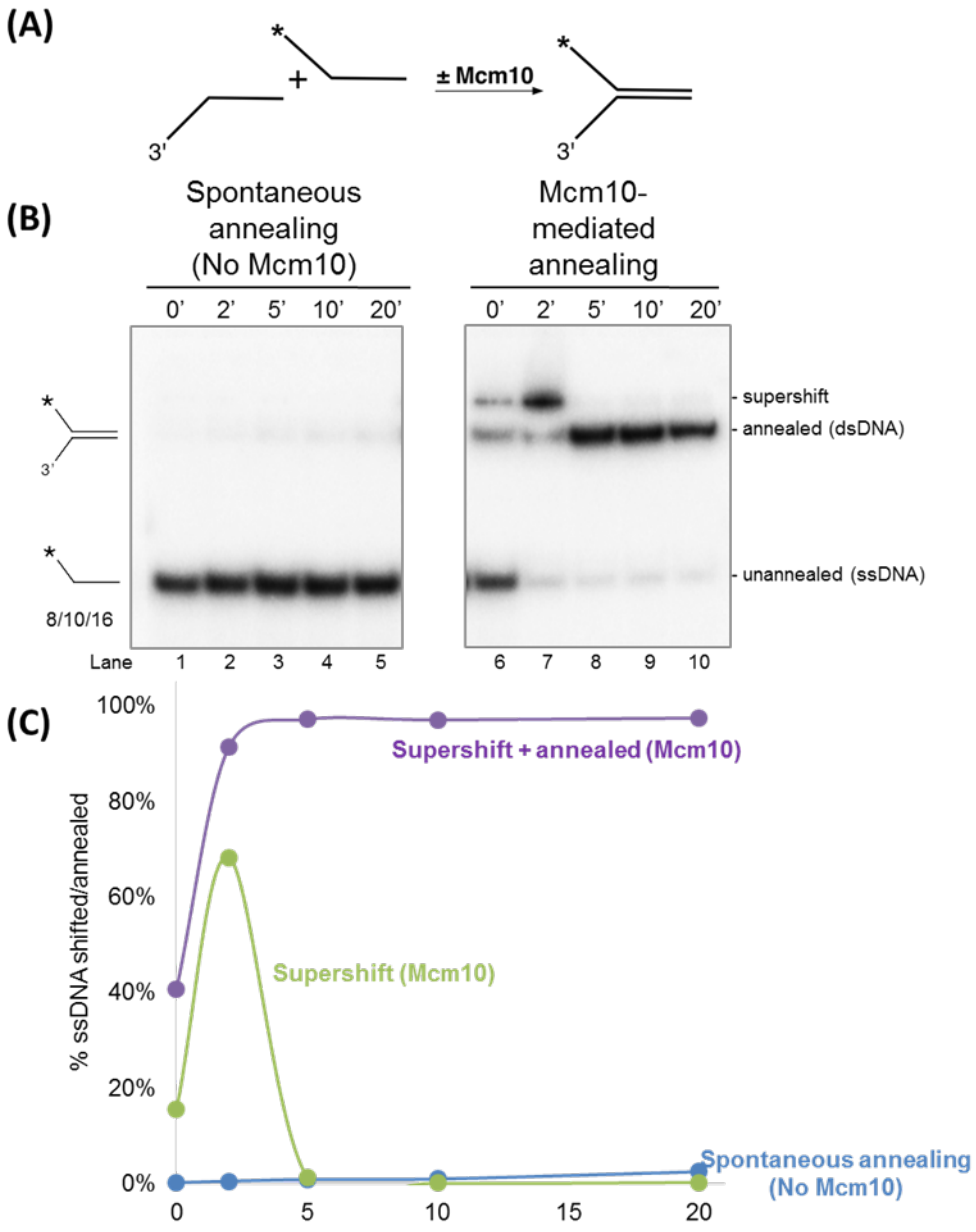

Figure 3.8: Mcm10 anneals oligos in solution. The data for this figure was collected in collaboration with Lance Langston in the O'Donnell Lab at Rockefeller University. (A) Experimental configuration. (B) Radioactive gel showing the reaction products; schematic on left and time points across the points. (C) Quantification of products over time.

Under single molecule conditions, it appears that Mcm10 can be pushed along the ssDNA and displaced by the reformation of the double-strand basepairing (Figure 3.9 C). Unzipping the DNA only partially allows Mcm10 to bind to the exposed ssDNA. During this initial unzipping some force peaks were measured, consistent with the moderate affinity of Mcm10 for dsDNA. Without delay, the two strands are then allowed to reanneal by slowing moving the optical trap back to its original position prior to unzipping (Figure 3.9A). When Mcm10 is absent from the reaction chamber, this "rezipping" step follows along the same force trajectory as the unzipping step. Departure from this force signature suggests an inhibition of basepairing by a bound protein, as is observed when Mcm10 is present during the experiment. Finally, once the tether has returned to its initial position prior to the initial unzipping step and the force has dropped below 2 pN, indicating full rezipping of naked DNA, the tether is then completely unzipped. This final unzipping can determine if a protein bound to the ssDNA remains bound through the rezipping process. In the case of Mcm10, the rezipping force is lower than that of naked DNA indicating the protein remains bound, however there is a variable force signature rather than a linear decrease (Figure 3.9C). A linear decrease in the rezipping force would indicate that the ssDNA is completely coated in protein which remains bound as the force drops. In the case of Mcm10, the rezipping force is decreased form that of naked DNA however it shows variations in the force signatures suggesting that basepairing is being facilitated by Mcm10. The subsequent unzipping then indicated that any bound Mcm10 is competed off the ssDNA by the reannealing of the two strands. Furthermore, is it worthwhile to note that while Mcm10 binds efficiently to exposed ssDNA it does not drive strand separation, even under force, consistent with bulk analysis (data not shown).

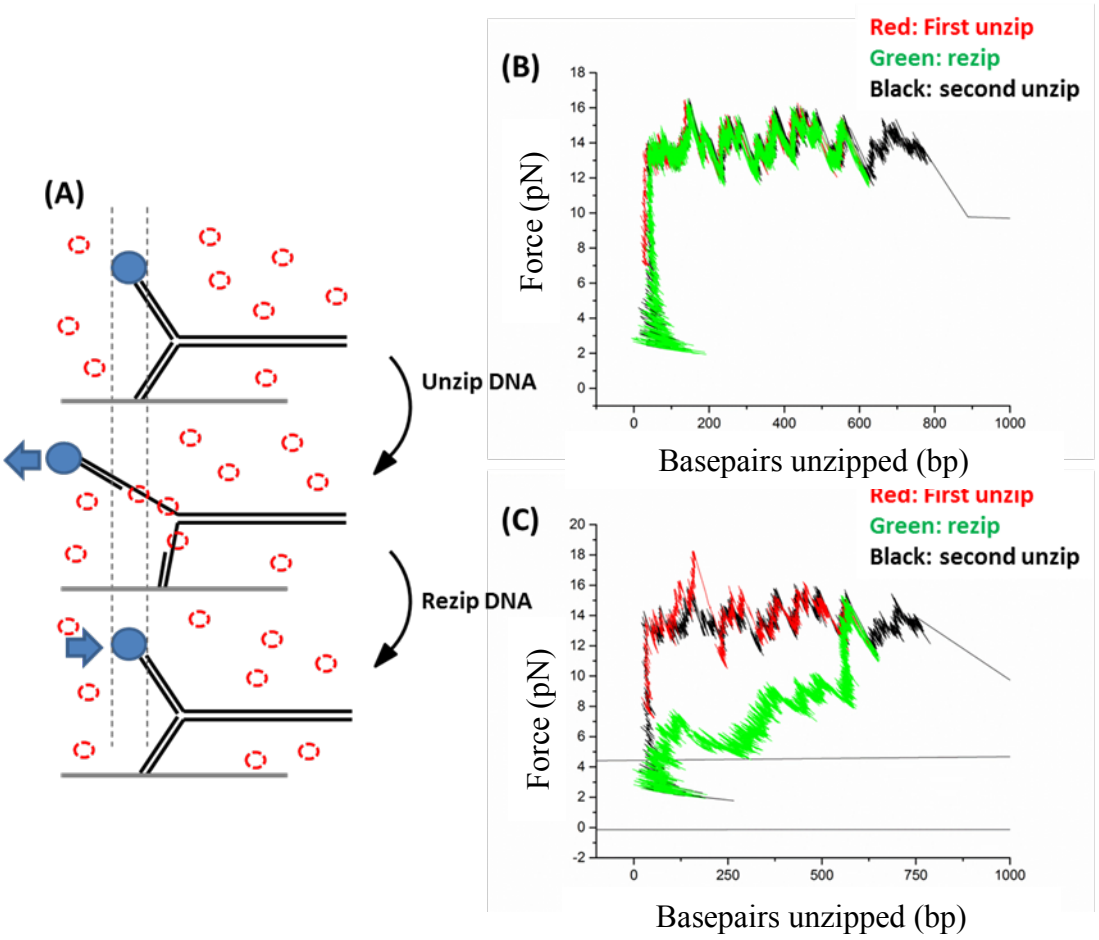

Figure 3.9: Mcm10 binding to exposed ssDNA. (A) Experimental configuration. (B) Example trace taken in the absence of free Mcm10. (C) Example traces taken in the presence of 225 nM Mcm10.

Building up the eukaryotic replisome for single molecule studies

Single molecule studies of polymerase-ε

The requirement of Mcm10 for efficient CMG activity in vitro, may also indicate the necessity for further replisome reconstitution to facilitate in vitro studies of the eukaryotic system. Intuitively this is logical given the many layers of control implemented in vivo that regulate replication progression and ensure a single, complete round of replication in each cell cycle. The leading strand polymerase (pol-ε) forms a very long-lived complex with CMG such it (CMGε) can be purified directly from yeast as a functional complex[52]. This purification scheme has been used for EM studies of the CMGε complex which has provided further insight into how DNA might be oriented and engaged by the core leading-strand replisome components[39]. From these recent studies, it appears that the leading strand may be highly distorted as it exits the helicase and enters the polymerase. Docking in the speculative positions of pol-α on the lagging strand suggests that the excluded strand would be tightly associated with the surface of CMG. The addition of polymerases to a replisome is known to increase the stability of the whole complex on the DNA, a clear advantage for efficient and faithful genome duplication[53].

With the goal of reconstituting eukaryotic replication under single molecule conditions, incremental characterization of the individual components is beneficial for determining the role of each component in the final reaction. To this end, the addition of the leading strand polymerase prompted experiments to assay strand extension by the polymerase alone similar to the studies done for the T7 replication system[54]. For these experiments there are several possible configurations, only two of which were utilized. First, a stretch of ssDNA is generated via

unzipping and then the tether is held a constant position until the force on the bead drop below a given threshold (in this case 10 pN) (Figure 3.10A). This experimental program has been utilized to study the T7 DNA polymerase where it is capable of binding from solution, extending the leading strand to the fork, where it can start to strand displace (efficiently only if it lacks the exonuclease domain) and drop the applied force on the leading strand. Once the force drops below the programmed threshold, the T7 DNA polymerase can continue to strand extend under constant force; the speed at which it processes depends on the assisting force applied[55] (Figure 3.10C). However, the yeast pol-ε does not show this behavior as there is no change to tether extension over time under a constant force.

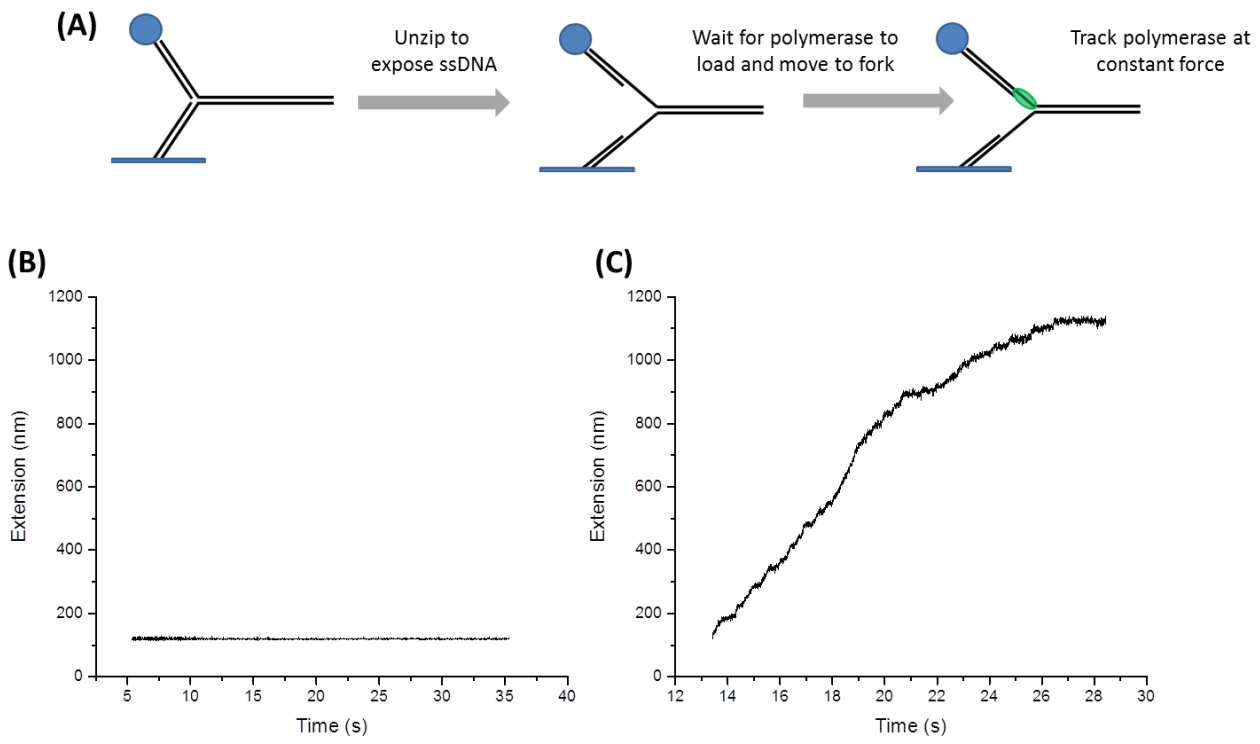

Figure 3.10: Real-time tracking of DNA polymerases. (A) Experimental configuration. (B) Monitoring tether extension over time in the presence of 20 nM pol-ε and 625 nM dNTPs. (C) Monitoring tether extension over time in the presence of 20 nM T7 gp5 and 625 nM dNTPs. The length of the Y-arms has been subtracted from the extension, such that zero corresponds to no dsDNA unwound rather than total tether extension. In this experiment, 300 bp (~100 nm) of DNA has been unzipped initially to facilitate polymerase loading, therefore the traces at this initial extension value rather than at zero.

To investigate whether pol-ε is perhaps synthesizing to the fork but unable to destabilize the basepairing at the junction, a slightly different configuration is used. First, about 400 bp of ssDNA is generated and then the tether is held at a constant position to allow the polymerase to load and primer extend. The tether is then rezipped until the force drops below 2 pN and then the tether is fully unzipped. (Figures 3.11 A and 3.12 A) This provided a measure of how extensive the DNA was able to reanneal and thus indicating the extent to which the primer was extended. Additionally, the change in force and j-index during the holding step also provides an indicator for polymerase activity along the ssDNA[54]. These measurements clearly demonstrate the activity of T7 gp5 on the DNA template (Figure 3.11 B and C), where the second unzipping revealed that the DNA was unable to reanneal (Figure 3.11B) indicated a complete primer extension. Additionally, the force decreased during this hold-step indicates that the polymerase has reached the fork and is destabilizing the basepairs there (Figure 3.11C). These signatures of primer extension are completely absent from the reactions performed with pol-ε[56] (Figure 3.12 B and C).

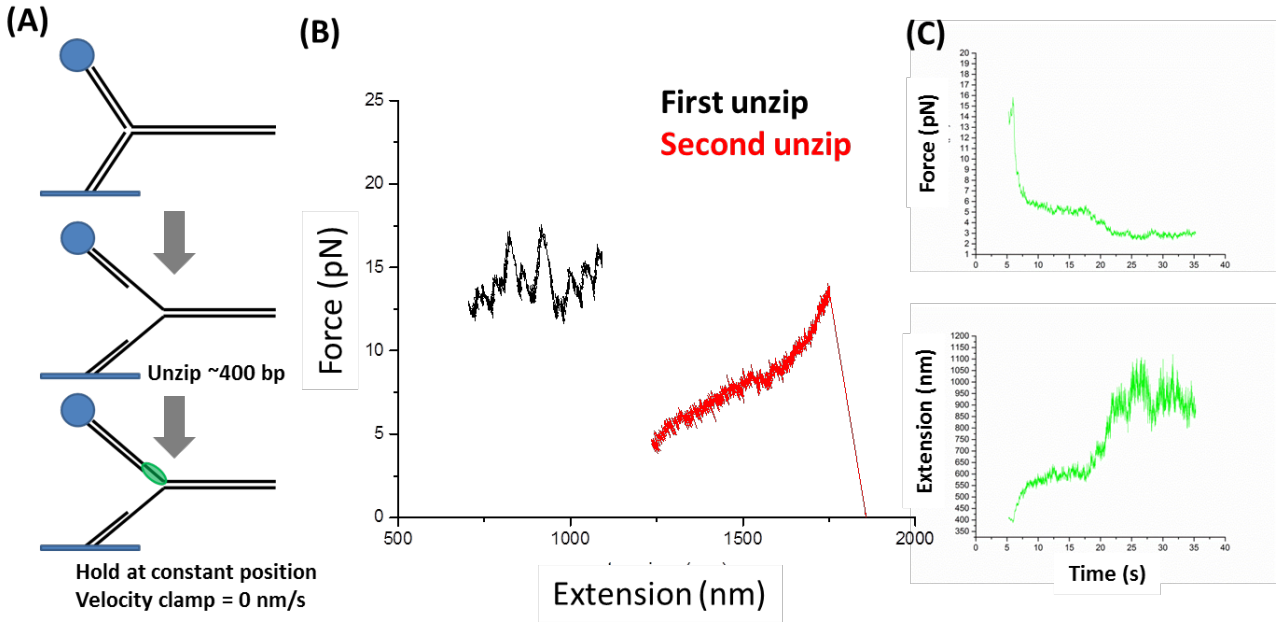

Figure 3.11: T7 polymerase robustly extends a primer under force. (A) Experimental configuration, not shown is the rezipping and second unzipping after the 30 second "hold" step. (B) The initial unzipping (black) to expose ssDNA. The second unzip after rezipping the tether shows no basepairing has reformed after the rezipping step indicating the primer has been efficiently extended to the fork junction. The extension shown corresponds to total extension, included the Y-arm length (~1.9Kb). (C) Force versus time and extension verses time during the hold step.

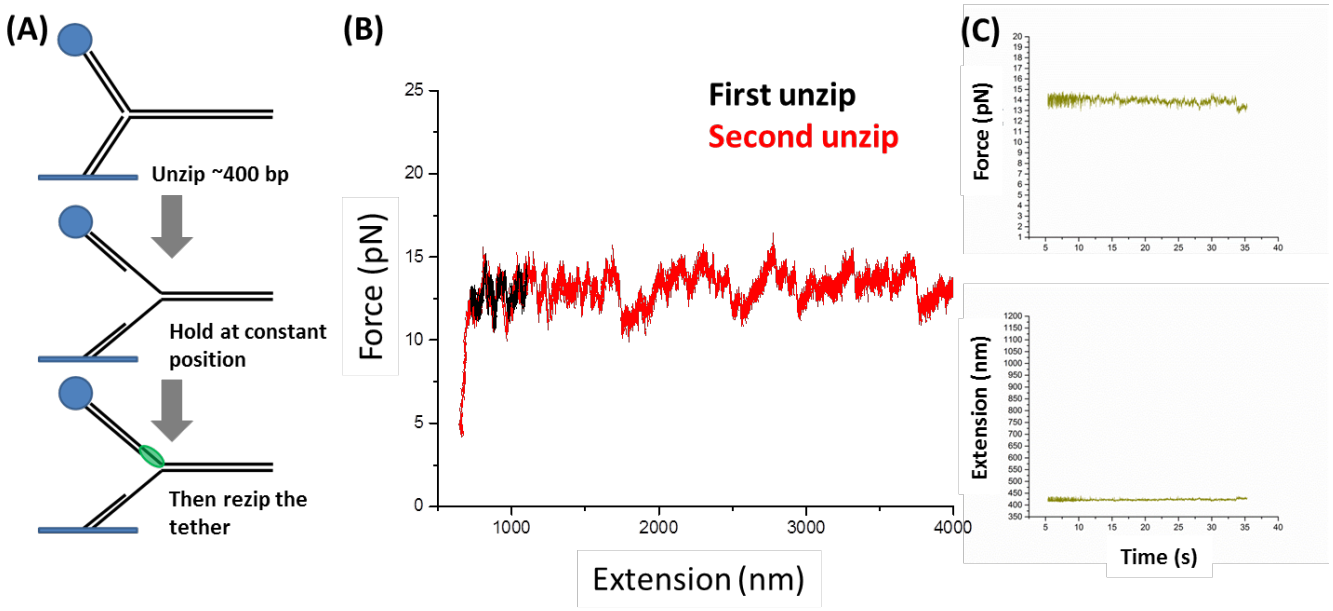

Figure 3.12: Polymerase-ε does not primer extend under force. (A) Experimental configuration, not shown is the rezipping and second unzipping after the 30 second "hold" step. (B) The initial unzipping (black) to expose ssDNA. The second unzip after rezipping the tether shows the basepairing has completely reformed after the rezipping step indicating no primer extension. The extension shown corresponds to total extension, included the Y-arm length (~1.9Kb). (C) Force versus time and tether extension verses time during the hold step. There is no change in the force or extension during the hold step indicating that the polymerase is not primer extending.

This configuration provides information regarding the extent of leading strand synthesis even in the case when the polymerase is unable to strand displace at the fork, which appears to be the case for pol-ε, under these experimental conditions. Alternatively, it is also possible that pol-ε can't efficiently load from solution onto the ssDNA without RFC, PCNA, and/or RPA[57,58]. Additionally, it is possible that pol-ε can load but cannot strand extend without RPA, which has been suggested to act as a true processivity factor for eukaryotic replisome components[57].

In bulk primer extension assays, RPA wasn't necessary for pol-ε primer extension (Figure 3.13 B). Interestingly, there is a clear intermediate product which could be the stalling of pol-ε within the pol-T region of the template, perhaps through the formation of secondary structures on the DNA or by polymerase slippage due to the homogeneous DNA sequence. One thing to note is that the time scale over which the primer is fully extended is on the order of 5-10 minutes which is much longer than single molecule tether lifetime. This may indicate that pol-ε alone has very low efficiency and processivity and may require RPA, PCNA, and RFC to increase its ability to process and load, respectively[57,58].

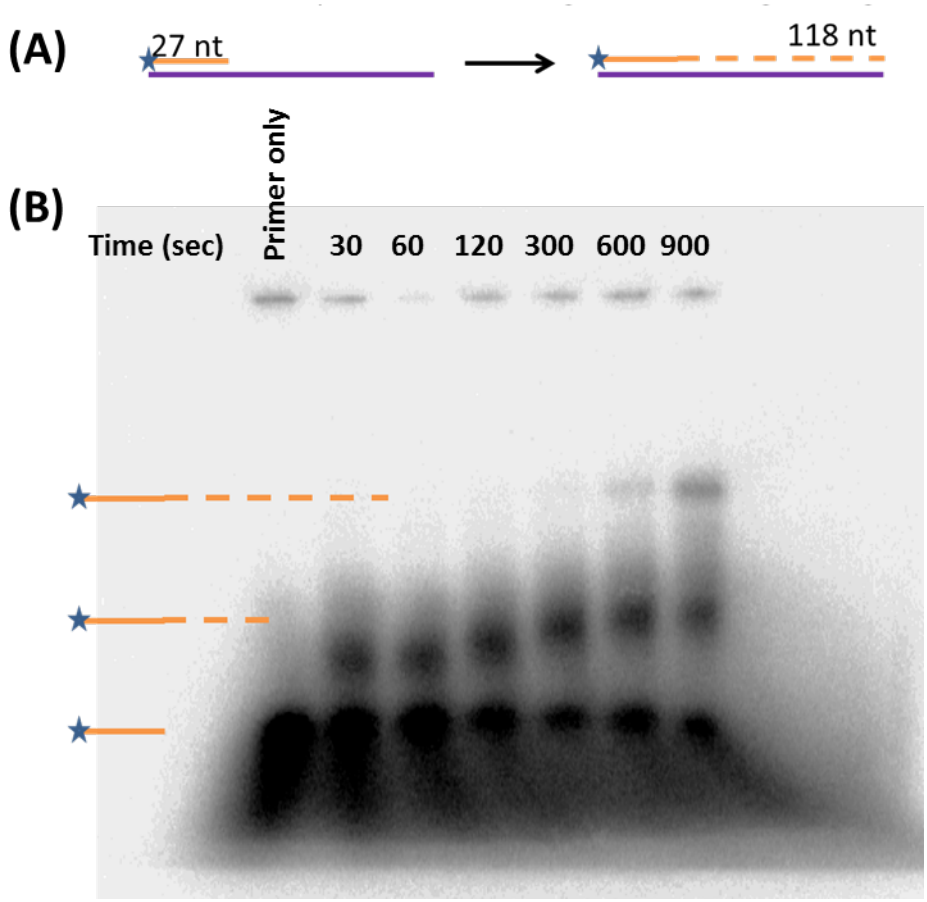

Figure 3.13: Polymerase-ε extends a primer without force or RPA. (A) Experimental configuration. (B) Radioactive gel with the reaction product schematics shown on the left and the time points along the top.

Conversion of ssDNA into dsDNA is modulated by RPA binding

To assay how RPA may facilitate primer extension by pol-ε the effects of RPA along under single molecule conditions first needs to be characterized. In vivo, RPA is thought to completely coat ssDNA resolving secondary structures and providing damage protection[59,60]. Despite this coating model, the change RPA makes to ssDNA is more subtle than one would expect: causing a slight increase in ssDNA extension and stiffness[61]. Similar measurements were made by unzipping a hairpin DNA template to generate ssDNA and then stretching the fully unzipping template past 50 pN in the presence of RPA. At these higher forces, the changes to ssDNA parameters by RPA are even more minimal than previously reported. Since this configuration and range of forces is more relevant for the unzipping-based experiments these measurements for ssDNA parameters are a better representation of the system.

	Kss	Kuhn Length
No RPA (N=9)	256.1109 ± 43.44	2.4147 ± 0.86
200 nM RPA (N=26)	255.1109 ± 31.24	2.4467 ± 0.56

Table 3.2: Calculated ssDNA parameters with and without RPA in solution.

Interestingly, RPA is capable of strand displacement under an applied force. This behavior has been reported before however the underlying mechanism that drives this capability is not completely understood[62-64]. From unzipping-rezipping experiments it seems that RPA is fully coating the exposed ssDNA as the rezipping force drops almost immediately and shows no force signatures indicative of even sparse base-pair formation (Figure 3.14). However, the RPA can be displaced by the reannealing DNA fork as evidence by the second unzipping which shows no difference from the initial unzip (Figure 3.14 C). RPA has been shown to slide along ssDNA in a similar re-zipping experimental configuration[62]. However if this was the case, the rezipping force signature should show an underlying force pattern reflecting the sequential reformation of basepairing.

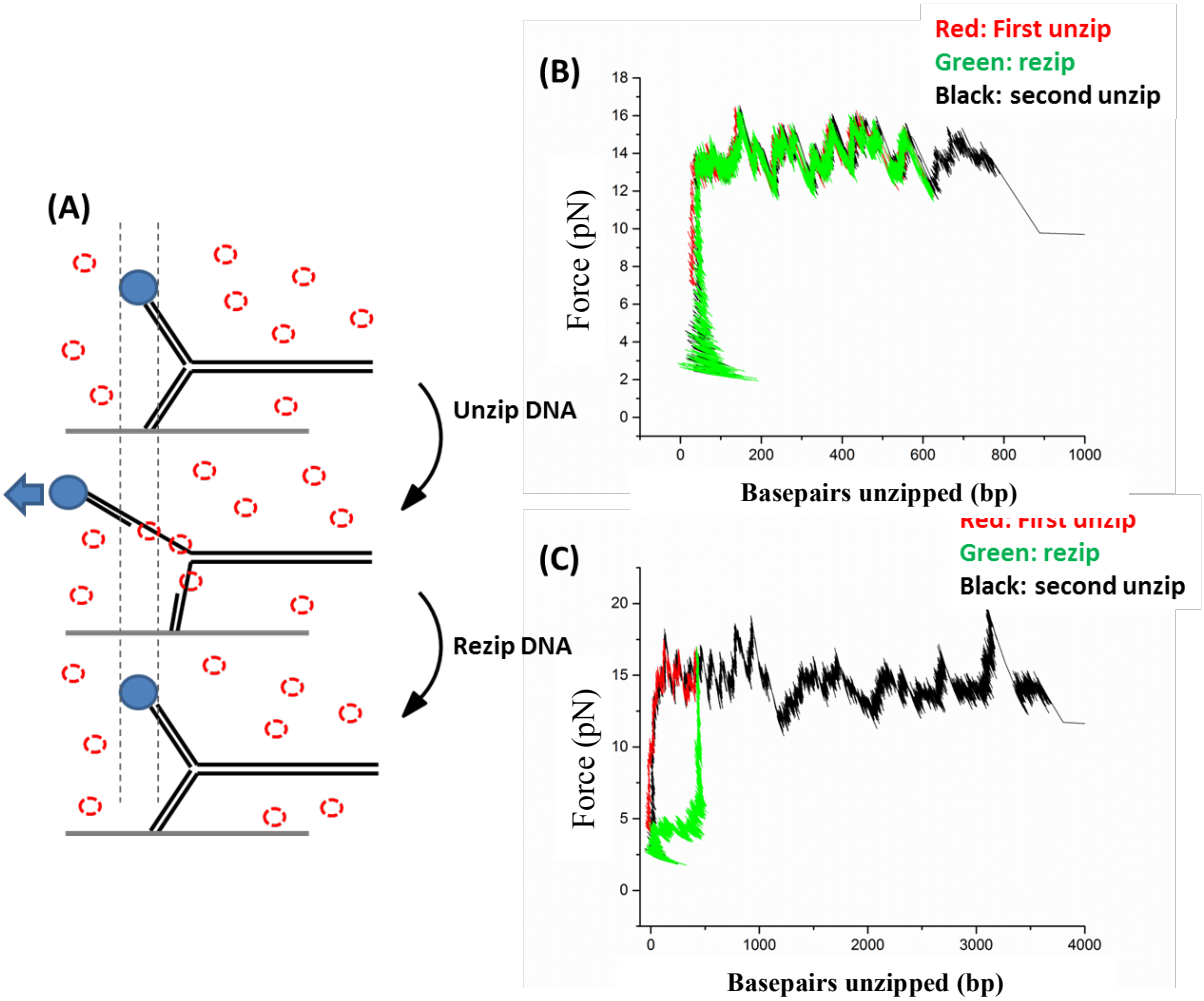

Figure 3.14: RPA binds to ssDNA and prevents re-zipping. (A) Experimental configuration. B) Example trace taken in the absence of free Mcm10. (C) Example traces taken in the presence of 200 nM RPA.

At a constant applied force, RPA can drive strand displacement (Figure 3.15). At 8pN of applied force, RPA will prevent reannealing but also doesn't facilitate strand separation either (Figure 3.15 B). This might be the maximal force that can be applied to an unzipping fork configuration when RPA is present in solution.

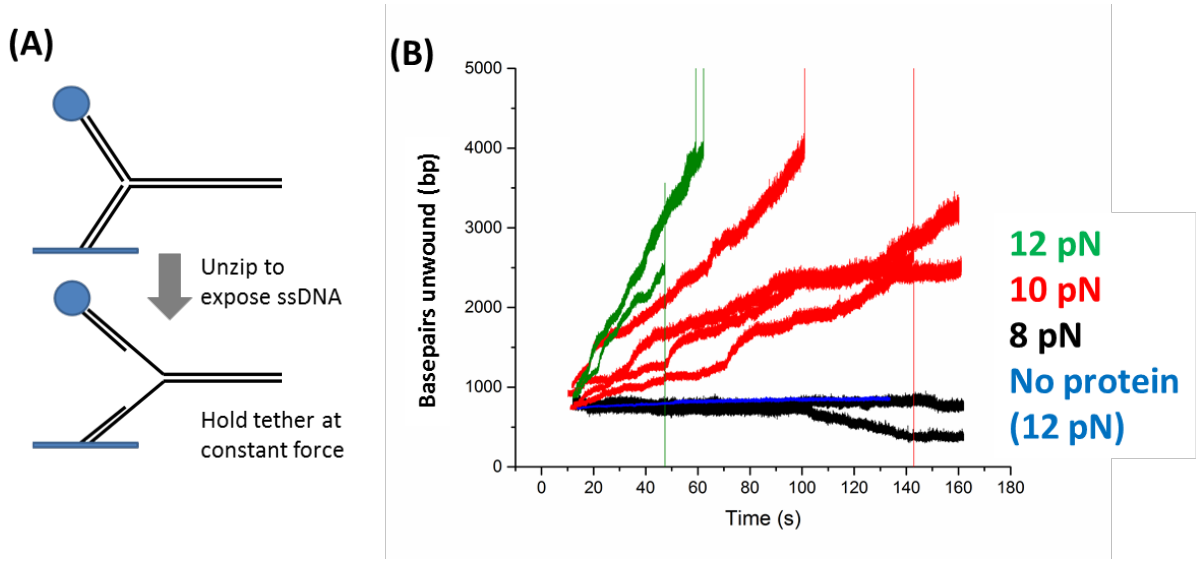

Figure 3.15: RPA can drive strand displacement under force. (A) Experimental configuration. (B) Example traces showing j-index increases over time when held at the indicated constant force in the presence of 200 nM RPA.

CMG and DNA polymerase epsilon act in conjunction to drive leading strand synthesis

Bulk assays of leading strand replication using purified proteins resulted in successful, if low efficiency, replication of an 800 bp segment of DNA. The only requirements for this were CMG and pol-ε, consistent with previous reports (Figure 3.16). Primer extension was possible without CMG only when strand displacement isn't required. When the leading strand is annealed to its complementary, lagging, strand CMG is necessary for full length primer extension. In this case, efficient leading strand replication is dependent on the efficient loading of CMG prior to pol-ε loading. In the case where pol- ε loads ahead of CMG, the progression of CMG would be blocked by the polymerase. Furthermore, if CMG loads and strand displaces it is possible that the resulting primed leading strand is then replicated by pol- ε alone; essentially decoupling CMG and pol- ε activity. This would only be possible on the short template where there is only 30 bp of annealed leading and lagging strands. On the 800 bp template, the helicase could load and start to strand displace only to get stuck within the downstream DNA is pol- ε is not present to replicate the leading strand and prevent the reannealing of the DNA behind the helicase. This, combined with inefficient CMG loading, could be the primary causes for the low replication efficiency. It should also be noted that the leading strand replication was performed for 20 minutes and only minimal full length products were observed. This could indicate the speed at which this very minimal system can replicate or it could reflect the loading efficiency of the proper protein configuration as discussed above.

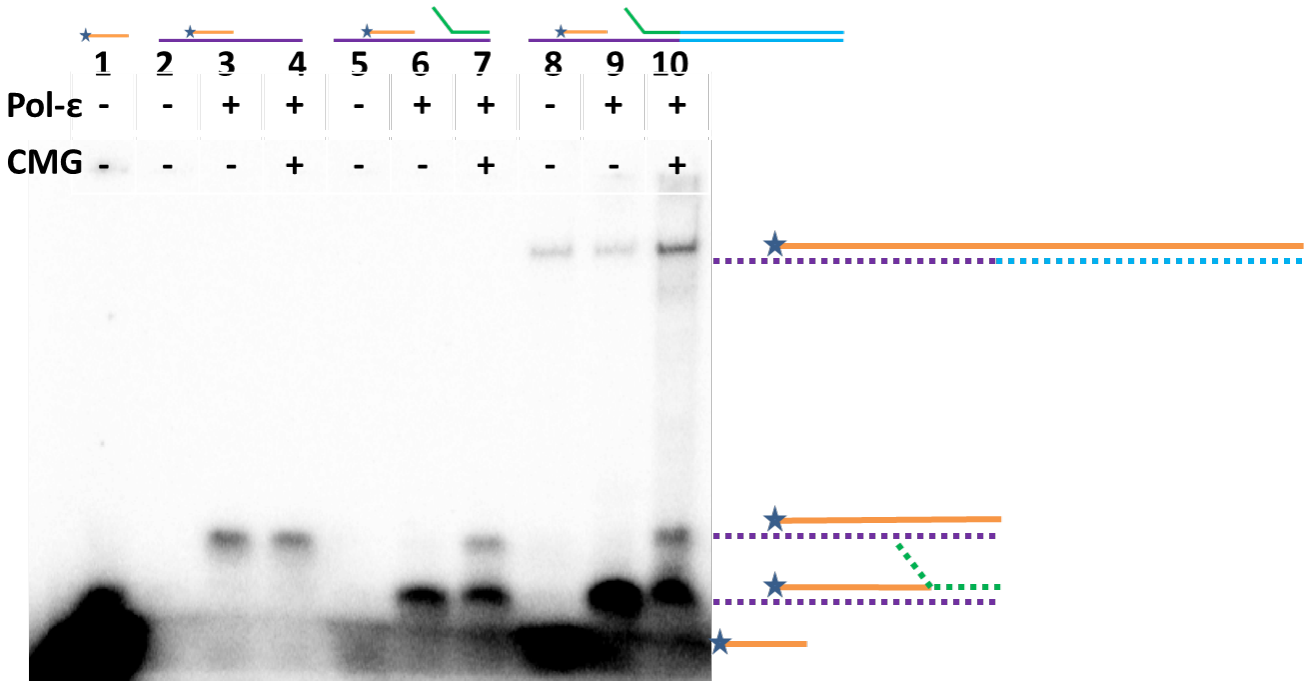

Figure 3.16: Leading strand replication. Along the top of the gel are the templates schematics used in each lane: lane 1 is the primer only, lane 2-4 is the primed leading strand, lane 5-7 is the primed fork, and lane 8-10 is the ligated primed fork. The presence of 20 nM pol-ε and/ or 100 nM CMG is also indicated along the top the gel. To the right of the gel is a schematic of the replication products.

FUTURE DIRECTIONS

Future experiments will have several key hurdles to overcome in order to successfully monitor CMG helicase activity or eukaryotic replication in real time. First and foremost, determining if the CMG helicase along can be tracked in real time; it is possible that without RPA and/or pol-ε the helicase isn't active under force. Given the ability for RPA to strand displace under force (Figure 3.15), adding RPA to a single molecule chamber would not result in meaningful data as any unwinding signal cannot be differentiated from that of RPA alone. It is not unthinkable that without RPA the functionality of the replisome would be compromised[59,60]. Even with an applied force that presumably eliminating secondary structures in the ssDNA and preventing reannealing of the strands behind the helicase or replisome, RPA may play a pivotal role in stabilizing the complex interactions at the replication fork[60].

Using a single optical trap and anchoring the helicase on the coverslip surface has not resulted in any clear indication that the helicase is active, at least in that configuration. One possible reason for this is that the helicase cannot fully engage the DNA due to steric hindrance by the coverslip surface. Alternatively, the helicase might be unwinding into the dsDNA and the ssDNA reanneals around the helicase, since only one point of the DNA is being manipulated the position of the fork ahead of the helicase can no longer be tracked or monitored. Reannealing of the DNA behind the helicase could also stall the helicase and inhibit further translocation, the ability for Mcm10 to increase CMG activity would only exacerbate this issue but quickly driving the progression of CMG into the DNA template. Another possibility is that Mcm10 is not efficiently finding the helicase, although it clearly has an effect in the TPM experiments indicating this might only be a minor concern.

Past the difficulties with tracking CMG, is the question as to whether pol-ε can primer extend on a strand of DNA that is extended under force. It clearly does not behave in the same manner as the T7 DNA polymerase, in that it doesn't even appear to bind to exposed ssDNA held under force. Perhaps this is because there isn't RFC and PCNA to help recruit and maintain the polymerase at the 3'-end of the primer[58]. Preliminary attempts to incorporate RFC and PCNA resulting in complete sticking of the tethers to the coverslip surface (data not shown), sticking issues are usually straight forward to resolve but may require alternative surface passivation methods such as PEG-lyation. A more complicated issue would be that perhaps pol-ε just cannot correctly interact with fully extended DNA or without RPA present[57].

One straight forward solution would be to instead try to capture snap-shots of replication by initiating replication in a chamber, then quenching the reaction by washing out free proteins and nucleotide, and then unzip a large subset of tethers. Proteins that remain bound can be precisely mapped to their position along the DNA and how they are interaction with the DNA could also be assayed. While this approach can't directly measure rates or processivity, it could be utilized to determine efficiency and ensemble rates. One concern with this is the efficiency with which replication occurs is very low (between 10 and 40%) making single molecule investigation of this system very time consuming[21,52]. Additionally, incorporating so many proteins (CMG, pol—ε, RPA, RFC, PCNA, and possibly the lagging polymerases) may make the resulting data very heterogeneous. This would then require a far larger data set that a more minimal systems like e. coli RNAP or a nucleosome.

However, as the in vitro reconstitution of eukaryotic replication improves it is likely that further biochemical insight may make the system more amenable for single molecule manipulation. Continuing to build up our understanding of the individual components does provide at least a baseline with which to compare future studies and perhaps identify differences between successful and unsuccessful experimental configurations. At this point, even the unsuccessful experiments are capable of providing insight into the capabilities and limitations of the eukaryotic replication machinery.

REFERENCES

1. Maine, G.T., Surosky, R.T. & Tye, B.K. Isolation and characterization of the centromere from chromosome V (CEN5) of Saccharomyces cerevisiae. *Mol Cell Biol* **4**, 86-91 (1984).
2. Bochman, M.L. & Schwacha, A. The Mcm complex: unwinding the mechanism of a replicative helicase. *Microbiol Mol Biol Rev* **73**, 652-83 (2009).
3. Pacek, M. & Walter, J.C. A requirement for MCM7 and Cdc45 in chromosome unwinding during eukaryotic DNA replication. *EMBO J* **23**, 3667-76 (2004).
4. Bochman, M.L. & Schwacha, A. The Mcm2-7 complex has in vitro helicase activity. *Mol Cell* **31**, 287-93 (2008).
5. Kaplan, D.L., Davey, M.J. & O'Donnell, M. Mcm4,6,7 uses a "pump in ring" mechanism to unwind DNA by steric exclusion and actively translocate along a duplex. *J Biol Chem* **278**, 49171-82 (2003).
6. You, Z. & Masai, H. DNA binding and helicase actions of mouse MCM4/6/7 helicase. *Nucleic Acids Res* **33**, 3033-47 (2005).
7. Duncker, B.P., Chesnokov, I.N. & McConkey, B.J. The origin recognition complex protein family. *Genome Biol* **10**, 214 (2009).
8. Sclafani, R.A. & Holzen, T.M. Cell cycle regulation of DNA replication. *Annu Rev Genet* **41**, 237-80 (2007).
9. Ticau, S., Friedman, L.J., Ivica, N.A., Gelles, J. & Bell, S.P. Single-molecule studies of origin licensing reveal mechanisms ensuring bidirectional helicase loading. *Cell* **161**, 513-25 (2015).
10. Sun, J. et al. Structural and mechanistic insights into Mcm2-7 double-hexamer assembly and function. *Genes Dev* **28**, 2291-303 (2014).
11. Samel, S.A. et al. A unique DNA entry gate serves for regulated loading of the eukaryotic replicative helicase MCM2-7 onto DNA. *Genes Dev* **28**, 1653-66 (2014).
12. Ticau, S. et al. Mechanism and timing of Mcm2-7 ring closure during DNA replication origin licensing. *Nat Struct Mol Biol* **24**, 309-315 (2017).
13. Im, J.S. et al. Assembly of the Cdc45-Mcm2-7-GINS complex in human cells requires the Ctf4/And-1, RecQL4, and Mcm10 proteins. *Proc Natl Acad Sci U S A* **106**, 15628-32 (2009).
14. Simon, A.C., Sannino, V., Costanzo, V. & Pellegrini, L. Structure of human Cdc45 and implications for CMG helicase function. *Nat Commun* **7**, 11638 (2016).
15. Dhingra, N., Bruck, I., Smith, S., Ning, B. & Kaplan, D.L. Dpb11 protein helps control assembly of the Cdc45.Mcm2-7.GINS replication fork helicase. *J Biol Chem* **290**, 7586-601 (2015).
16. Perez-Arnaiz, P., Bruck, I. & Kaplan, D.L. Mcm10 coordinates the timely assembly and activation of the replication fork helicase. *Nucleic Acids Res* **44**, 315-29 (2016).
17. Moyer, S.E., Lewis, P.W. & Botchan, M.R. Isolation of the Cdc45/Mcm2-7/GINS (CMG) complex, a candidate for the eukaryotic DNA replication fork helicase. *Proc Natl Acad Sci U S A* **103**, 10236-41 (2006).
18. Costa, A. et al. The structural basis for MCM2-7 helicase activation by GINS and Cdc45. *Nat Struct Mol Biol* **18**, 471-7 (2011).
19. Ilves, I., Petojevic, T., Pesavento, J.J. & Botchan, M.R. Activation of the MCM2-7 helicase by association with Cdc45 and GINS proteins. *Mol Cell* **37**, 247-58 (2010).

20. Alabert, C. & Groth, A. Chromatin replication and epigenome maintenance. *Nat Rev Mol Cell Biol* **13**, 153-67 (2012).
21. Georgescu, R.E. et al. Mechanism of asymmetric polymerase assembly at the eukaryotic replication fork. *Nat Struct Mol Biol* **21**, 664-70 (2014).
22. Finkelstein, J., Antony, E., Hingorani, M.M. & O'Donnell, M. Overproduction and analysis of eukaryotic multiprotein complexes in Escherichia coli using a dual-vector strategy. *Anal Biochem* **319**, 78-87 (2003).
23. Inman, J.T. et al. DNA Y structure: a versatile, multidimensional single molecule assay. *Nano Lett* **14**, 6475-80 (2014).
24. Fu, Y.V. et al. Selective bypass of a lagging strand roadblock by the eukaryotic replicative DNA helicase. *Cell* **146**, 931-41 (2011).
25. Lang, S. & Huang, L. The Sulfolobus solfataricus GINS Complex Stimulates DNA Binding and Processive DNA Unwinding by Minichromosome Maintenance Helicase. *J Bacteriol* **197**, 3409-20 (2015).
26. Bochman, M.L. & Schwacha, A. Differences in the single-stranded DNA binding activities of MCM2-7 and MCM467: MCM2 and MCM5 define a slow ATP-dependent step. *J Biol Chem* **282**, 33795-804 (2007).
27. Hesketh, E.L. et al. DNA induces conformational changes in a recombinant human minichromosome maintenance complex. *J Biol Chem* **290**, 7973-9 (2015).
28. Costa, A. et al. Structural studies of the archaeal MCM complex in different functional states. *J Struct Biol* **156**, 210-9 (2006).
29. Li, N. et al. Structure of the eukaryotic MCM complex at 3.8 A. *Nature* **524**, 186-91 (2015).
30. Yuan, Z. et al. Structure of the eukaryotic replicative CMG helicase suggests a pumpjack motion for translocation. *Nat Struct Mol Biol* **23**, 217-24 (2016).
31. Boos, D., Frigola, J. & Diffley, J.F. Activation of the replicative DNA helicase: breaking up is hard to do. *Curr Opin Cell Biol* **24**, 423-30 (2012).
32. Costa, A. et al. DNA binding polarity, dimerization, and ATPase ring remodeling in the CMG helicase of the eukaryotic replisome. *Elife* **3**, e03273 (2014).
33. Sun, B. et al. ATP-induced helicase slippage reveals highly coordinated subunits. *Nature* **478**, 132-5 (2011).
34. Johnson, D.S., Bai, L., Smith, B.Y., Patel, S.S. & Wang, M.D. Single-molecule studies reveal dynamics of DNA unwinding by the ring-shaped T7 helicase. *Cell* **129**, 1299-309 (2007).
35. Langston, L. & O'Donnell, M. Action of CMG with strand-specific DNA blocks supports an internal unwinding mode for the eukaryotic replicative helicase. *Elife* **6**(2017).
36. Abid Ali, F. et al. Cryo-EM structures of the eukaryotic replicative helicase bound to a translocation substrate. *Nat Commun* **7**, 10708 (2016).
37. Graham, B.W., Schauer, G.D., Leuba, S.H. & Trakselis, M.A. Steric exclusion and wrapping of the excluded DNA strand occurs along discrete external binding paths during MCM helicase unwinding. *Nucleic Acids Res* **39**, 6585-95 (2011).
38. Singleton, M.R., Dillingham, M.S. & Wigley, D.B. Structure and mechanism of helicases and nucleic acid translocases. *Annu Rev Biochem* **76**, 23-50 (2007).
39. Sun, J. et al. The architecture of a eukaryotic replisome. *Nat Struct Mol Biol* **22**, 976-82 (2015).

40. Georgescu, R. et al. Structure of eukaryotic CMG helicase at a replication fork and implications to replisome architecture and origin initiation. *Proc Natl Acad Sci U S A* **114**, E697-E706 (2017).
41. Kang, S., Warner, M.D. & Bell, S.P. Multiple functions for Mcm2-7 ATPase motifs during replication initiation. *Mol Cell* **55**, 655-65 (2014).
42. Looke, M., Maloney, M.F. & Bell, S.P. Mcm10 regulates DNA replication elongation by stimulating the CMG replicative helicase. *Genes Dev* **31**, 291-305 (2017).
43. Araki, Y., Kawasaki, Y., Sasanuma, H., Tye, B.K. & Sugino, A. Budding yeast mcm10/dna43 mutant requires a novel repair pathway for viability. *Genes Cells* **8**, 465-80 (2003).
44. Eisenberg, S., Korza, G., Carson, J., Liachko, I. & Tye, B.K. Novel DNA binding properties of the Mcm10 protein from Saccharomyces cerevisiae. *J Biol Chem* **284**, 25412-20 (2009).
45. Thu, Y.M. & Bielinsky, A.K. MCM10: one tool for all-Integrity, maintenance and damage control. *Semin Cell Dev Biol* **30**, 121-30 (2014).
46. Baxley, R.M. & Bielinsky, A.K. Mcm10: A Dynamic Scaffold at Eukaryotic Replication Forks. *Genes (Basel)* **8**(2017).
47. Christensen, T.W. & Tye, B.K. Drosophila MCM10 interacts with members of the prereplication complex and is required for proper chromosome condensation. *Mol Biol Cell* **14**, 2206-15 (2003).
48. Zhu, W. et al. Mcm10 and And-1/CTF4 recruit DNA polymerase alpha to chromatin for initiation of DNA replication. *Genes Dev* **21**, 2288-99 (2007).
49. Perez-Arnaiz, P. & Kaplan, D.L. An Mcm10 Mutant Defective in ssDNA Binding Shows Defects in DNA Replication Initiation. *J Mol Biol* **428**, 4608-4625 (2016).
50. Okorokov, A.L. et al. Hexameric ring structure of human MCM10 DNA replication factor. *EMBO Rep* **8**, 925-30 (2007).
51. Du, W. et al. Mcm10 self-association is mediated by an N-terminal coiled-coil domain. *PLoS One* **8**, e70518 (2013).
52. Langston, L.D. et al. CMG helicase and DNA polymerase epsilon form a functional 15-subunit holoenzyme for eukaryotic leading-strand DNA replication. *Proc Natl Acad Sci U S A* **111**, 15390-5 (2014).
53. Stillman, B. DNA polymerases at the replication fork in eukaryotes. *Mol Cell* **30**, 259-60 (2008).
54. Wuite, G.J., Smith, S.B., Young, M., Keller, D. & Bustamante, C. Single-molecule studies of the effect of template tension on T7 DNA polymerase activity. *Nature* **404**, 103-6 (2000).
55. Sun, B. et al. T7 replisome directly overcomes DNA damage. *Nat Commun* **6**, 10260 (2015).
56. Ganai, R.A., Zhang, X.P., Heyer, W.D. & Johansson, E. Strand displacement synthesis by yeast DNA polymerase epsilon. *Nucleic Acids Res* **44**, 8229-40 (2016).
57. Kenny, M.K., Lee, S.H. & Hurwitz, J. Multiple functions of human single-stranded-DNA binding protein in simian virus 40 DNA replication: single-strand stabilization and stimulation of DNA polymerases alpha and delta. *Proc Natl Acad Sci U S A* **86**, 9757-61 (1989).

58. Chilkova, O. et al. The eukaryotic leading and lagging strand DNA polymerases are loaded onto primer-ends via separate mechanisms but have comparable processivity in the presence of PCNA. *Nucleic Acids Res* **35**, 6588-97 (2007).
59. Fanning, E., Klimovich, V. & Nager, A.R. A dynamic model for replication protein A (RPA) function in DNA processing pathways. *Nucleic Acids Res* **34**, 4126-37 (2006).
60. Broderick, S., Rehmet, K., Concannon, C. & Nasheuer, H.P. Eukaryotic single-stranded DNA binding proteins: central factors in genome stability. *Subcell Biochem* **50**, 143-63 (2010).
61. Chen, J., Le, S., Basu, A., Chazin, W.J. & Yan, J. Mechanochemical regulations of RPA's binding to ssDNA. *Sci Rep* **5**, 9296 (2015).
62. Kemmerich, F.E. et al. Force regulated dynamics of RPA on a DNA fork. *Nucleic Acids Res* **44**, 5837-48 (2016).
63. De Vlaminck, I. et al. Torsional regulation of hRPA-induced unwinding of double-stranded DNA. *Nucleic Acids Res* **38**, 4133-42 (2010).
64. Georgaki, A., Strack, B., Podust, V. & Hubscher, U. DNA unwinding activity of replication protein A. *FEBS Lett* **308**, 240-4 (1992).

CHAPTER 4

SMALL MOLECULE INJECTION INTO SINGLE-CELL C. ELEGANS EMBRYOS VIA CARBON-REINFORCED NANOPIPETTES

PLoS One. 2013 Sep 26; 8 (9): e75712. Doi: 10.1371/journal.pone.0075712.eCollection 2013.

Brennan, L.D.*, Roland, T.* Morton, D.G., Fellman, S.M., Chung, S., Kevek J.W., McEuen P.M., Kemphues K.J., Wang, M.D. *Small molecule injection into single-cell C. elegans embryos via carbon-reinforced nanopipettes*. Adapted with permission from PLOS. *equal contribution

L.D.B. and R.T. fabricated and images the nanopipettes with the supervision of J.W.K. and P.M.M. L.D.B. performed the injection volume measurements and cell injections with assistance from R.T. and D.G.M. The project was initiated by R.T. and S.C. with P.M.M., K.J.K., and M.D.W. L.B. wrote the manuscript with help from R.T., S.M.F., D.G.M., K.J.K. and M.D.W. K.J.K and M.D.W. supervised the project.

INTRODUCTION

The ability to introduce chemical inhibitors into single cells has been an important approach for understanding signaling pathways in many organisms. However, some cells, such as those of the *Caenorhabditis elegans* embryo, are surrounded by an outer layer that provides protection from the environment and makes application of drugs challenging. To address this difficulty, we have developed an injection technique using carbon-reinforced nanopipettes (CRNPs) to introduce a chemical inhibitor into the single-celled *C. elegans* embryo and have used this approach to reinvestigate early polarity establishment. Our technique allows penetration of the embryo with minimal cellular damage, at precisely controlled times in development, facilitating the study of temporally-confined cellular events.

The single-celled *C. elegans* embryo is well established as a model system for studying cell polarity. During the first cell cycle, a remarkable reorganization of the cytoskeletal and cytoplasmic components occurs, culminating in an asymmetric first division yielding daughter cells with different sizes, cell cycle rates and developmental potential [1]. In the early one-cell embryo the essential polarity proteins PAR-3, PAR-6, and PKC-3 are present uniformly around the cortex, but concomitant with actomyosin-driven cortical flows, recede from the posterior end and occupy a cortical domain in the anterior half of the embryo [2,3,4,5,6]. The regression of the anterior PAR proteins away from the posterior pole allows a second set of essential polarity proteins, PAR-2 and PAR-1, to localize to the posterior cortex, in a manner that is mutually exclusive with the anterior proteins [7,8,9], reviewed by Cowan & Hyman [10], Nance & Zallen [11], and Noatynska & Gotta [12]. It is clear that actomyosin contractility plays a significant

role in anteroposterior (A-P) polarization [2,10,13] and there is evidence that microtubules can also direct polarity initiation in the early embryo [14,15,16,17].

A number of experimental approaches have been used to address the role of the cytoskeleton in *C. elegans* embryo polarity, including RNAi knockdown of individual proteins, genetic analyses, and treatment with chemical inhibitors and each system has inherent limitations. Because many cytoskeletal components are essential, using RNAi knockdown and genetic mutation to probe processes of polarity can reduce viability and/or result in sterility, yielding few embryos for analysis, and those remaining may have only partial depletion of protein activity. The use of chemical inhibitors to perturb the early embryo has been difficult due to the tough eggshell covering and permeability barrier that surround the *C. elegans* embryo [18,19,20]. Permeablilization of the embryo for exposure to specific drugs [19,21,22,23,24] has been exceptionally challenging in very early embryos due to their fragility. Genetic mutants and RNAi knockdown to produce *C. elegans* embryos with permeable eggshells have simplified embryonic drug treatment [25,26], but it would also be useful to directly introduce inhibitors into embryos of any genotype. Glass micropipettes have been used to pierce the *C. elegans* embryo for introduction of dyes by iontophoresis to study cell-cell communication in *C. elegans* [27,28]. However, glass needles are quite fragile, and this approach has not generally been employed for delivery of drug delivery in *C.elegans*; investigators have instead relied upon the other means of eggshell permeabilization, noted above. We have found that by reinforcing glass pipettes with an interior lining of carbon, their use for injection of molecules into *C. elegans* embryos becomes readily successful and reproducible. The injection technique that we have developed enables direct administration of small molecules at an extremely early developmental stage, and can be

used for embryos of any genotype to perturb developmental events with high temporal accuracy and reproducibility.

We have utilized carbon-reinforced nanopipettes (CRNPs) to penetrate the *C. elegans* embryo and directly introduce small molecules, and have coupled this with live imaging to visualize the effects of specific inhibitor treatment. In addition to the precise temporal control of this approach, our injection technique allows for simple dosage titration and can easily be combined with RNAi and genetic mutation. Because of the very fine tip of these pipettes, injection into single blastomeres at later stages is also possible. To demonstrate the utility of the CRNPs we have injected the actin polymerization inhibitor, Latrunculin A (LatA), into one-cell embryos prior to polarity establishment and have determined the consequences of such perturbations on the dynamic localization of two critical polarity proteins, the posterior protein PAR-2 and the anterior protein PAR-6.

MATERIALS & METHODS

Pipette fabrication

Fig. 1a shows the protocol steps for making CRNPs, adapted from previous studies [32,54]. Quartz capillaries (Sutter Instrument; Q100-70-7.5) were filled, via capillary action, with ~115 µL of catalyst solution (18 mg $Fe(NO_3)_3$ in 25 mL isopropyl alcohol) and laid flat to air dry at 21°C for at least 12 hours. They were then pulled with a pipette puller (Sutter Instruments P2000, parameters are (Heat, Filament, Velocity, Delay, Pull) = $(700, 4, 55, 130, 55)_{line1}$ and (H, F, V, D, P) = $(700, 4, 55, 130, 250)_{line2}$) into nanopipettes with outer and inner tip diameters of 135 ±66 nm and 74 ± 939 nm, respectively (N =80). A quartz tube ~1 inch in diameter and ~2 inches long was used to hold the pulled pipettes during carbon deposition. The pulled pipettes

were placed in a chemical vapor deposition (CVD) furnace (Kevek Innovations, USA) to deposit a layer of amorphous carbon on the interior surface of the pipettes (6 h; 0.9 Standard Liter per Minute (SLM) CH_4 and 0.6 SLM Ar at 920°C). Figure 1b shows an image after CVD, acquired using a LEO 1550 Field Emission Scanning Electron Microscope (Zeiss, Oberkochen, Germany). CRNPs were fabricated in batches of ~80, stored at room temperature (21°C) and ambient pressure, and front-loaded with solutions of interest before each injection experiment (see below).

To prepare holding pipettes, unmodified quartz capillaries, were pulled to a ~15 μm tip with parameters (H, F, V, D, P) = (700, 5, 100, 250, 100). These pipettes were used without subsequent modification as holders to maintain embryo position during piercing and injection.

Preparation of small molecules and CRNP loading

DAPI (D8417, Sigma) was dissolved in water to a final concentration of 2 mg/mL and stored at 4°C. Latrunculin A (L5163, Sigma) was dissolved in DMSO to a final concentration of 2.4 mM, aliquoted and stored for a maximum of 3 months at -20°C. All small molecule stock solutions were further diluted in 0.8X Egg Buffer (EB) + 0.5mM polyvinylpyrrolidone (PVP; P2307, Sigma) [19] (1X EB: 118 mM NaCl, 48 mM KCl, 2 mM $CaCl_2$, 2 mM $MgCl_2$) to a final concentration of 0.2 mg/mL for DAPI and 60 μM or 90 μM for LatA.. YOYO-1 1mM stock solution (Y3601, Invitrogen) was diluted in 1X egg buffer to a final concentration of 1μM. Working solutions were kept at 4°C for no more than 2 days.

CRNPs were frontloaded by applying suction with a hand-held syringe, for 3 minutes. Loaded

CRNPs were then mounted on a manipulator and dipped into a droplet of injection solution and left to equilibrate for 3 minutes. CRNPs were attached to a Femtojet unit (Eppendorf, Hamburg, Germany) to control duration and pressure of injection. A second micromanipulator, opposite the mounted CRNP, was use to manipulate the holding pipette. This holding pipette was attached via plastic tubing to a 50 ml syringe, which could be used to apply suction to hold the embryo in place during CRNP penetration and removal.

C. elegans strains and maintenance

C. elegans strains were maintained by standard techniques [55], at room temperature (21-23°C) before isolation of the embryos. N2 (Bristol) was used as the wild-type strain. Strains expressing fluorescently tagged proteins of interest have the following genotypes:

TY3558 *unc-119(ed3) ruIs32[Ppie-1::GFP::his-11 + unc-119(+)] III; ojIs1[pie-1::GFP::tbb-2 + unc-119(+)]*

KK1177 *unc-119(ed3) ruIs32[Ppie-1::GFP::his-11 + unc-119(+)] III; axIs1929 [pFM033 pie-1::NMY-2::GFP and mCherry::PAR-2, unc-119(+)]*

KK1169 *itIs272[Ppar-6::PAR-6::mCherry + unc-119(+)]; itIs153[pie-1::PAR-2::GFP (pMW1.03, pRF4 rol-6]* (provided by Alex Beatty, Cornell University).

itIs153 is from Cuenca et al. (2003) [8]; *itIs272* is an mCherry derivative of pJN284 [56] provided by Heon Kim, Cornell University, and *axIs1929* is from Zonies el al. (2010) [43]. TY3558 was provided by the Caenorhabditis Genetic Center, which is funded by the National Institutes of Health Office of Research Infrastructure Programs (P40 OD010440).

RNAi treatment

RNAi was performed by feeding [57]. HT115(DE3) bacteria were freshly transformed with RNAi plasmids, grown to log phase, induced with 400 μM IPTG for 2.5 hours, concentrated five-fold and spotted onto agar plates containing minimal medium with 12.5 μg/mL tetracycline and 50 μg/mL carbenicillin. Worms were allowed to feed on RNAi bacteria at least 16 hours before embryo isolation. L4440 empty vector was used as a negative control [58]. The *par-6* RNAi construct is from Aono et al.(2004) [59].

Injection experiments

One-cell embryos were isolated from young adult worms by dissection in 0.8X EB + 0.5 mM PVP on a glass coverslip. A Ti-E Nikon inverted microscope (Nikon Instruments, Melville NY USA) was used for imaging. A holding pipette was used to immobilize the embryo and the embryo was oriented such that the CRNP would pierce the anterior end as determined by polar body position. Embryos were injected immediately following meiosis II, as assessed by GFP::histone visualization. Duration of injection was set to 1 second, and injection pressure ranged from 10 to 20 psi. Injection success was verified by assessing the morphological phenotypes produced by LatA or by dye visualization. Each CRNP was used to inject multiple embryos.

Application of suction to the holding pipette allowed CRNP withdrawal after injection. Nomarski and fluorescence (FITC, C-FL Texas Red HYQ or DAPI, Nikon filters) images were acquired (NIS Elements, Nikon) sequentially every 30 sec until either cytokinesis or the equivalent cell cycle stage was reached or 1 h elapsed, whichever occurred first.

Embryos injected with YOYO-1 were transferred using a large quartz pipette to a fresh drop of 0.8X + 0.5 mM PVP on a glass coverslip for further development. The drop was kept in a humid chamber for up to 24 hours or until hatching.

For the injection volume calibration, we injected 1.25 mg/ml of dextran-TxRED (~3000 MW) (Invitrogen) into glycerol. The fluorescence image of dextran immediately following injection completion (1 s after injection was initiated) was used to calibrate the injection volume. An intensity line scan of the injected drop of the image was fit to a Gaussian function and the standard deviation of the Gaussian was used to estimate the radius of the spherical drop.

RESULTS

Carbon-reinforced nanopipettes (CRNPs) as a novel drug delivery tool

Single-cell microinjection has been utilized quite commonly as a method for directly introducing small molecules, proteins, RNAs, and DNAs into individual cells. Micropipettes have a tip size of approximately 0.5 μm [29] and are fabricated by pulling glass capillaries to the desired tip diameter [30]. These micropipettes have several limitations owing to the material properties of glass and their large tip size, relative to cell size. Cellular damage due to the large pipette tip diameter is a major limitation in microinjection techniques [31], especially when the cells are small. Reducing the tip diameter should reduce cellular damage. However, glass pipettes, when pulled to smaller dimensions, are more fragile and prone to breakage [32].

To successfully pierce the chitinous shell and permeability barriers, while minimizing damage to the embryo, the tip of an injection pipette must be both strong and small. To accomplish this, quartz capillaries were pulled to an outer tip diameter of 135 ± 66 nm (mean ± SD) and then

reinforced with an interior layer of carbon (Fig.4. 1a and b). Such pipettes are less prone to breakage after repeated injections than are unlined capillaries. An added advantage of the carbon coating is increased visibility of the tip location of the CRNP. Carbon nanopipettes have previously been used to inject dyes [32] and secondary messengers [33] into epithelial cells. Here we have optimized their geometry for precise and delicate injection into the single-cell *C. elegans* embryo.

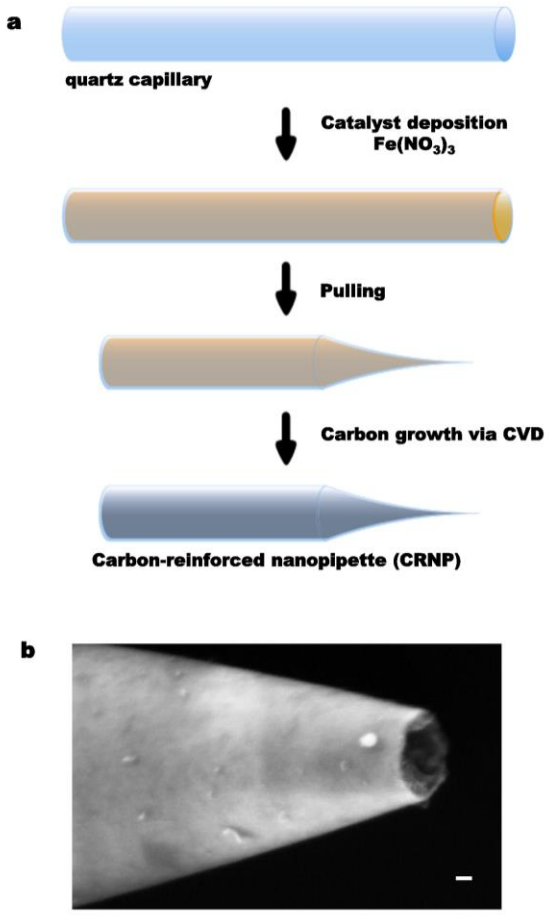

Figure 4.1: Carbon-reinforced nanopipette (CRNP) fabrication.

(**a**) CRNP fabrication procedure. Quartz capillaries were filled with $Fe(NO_3)_3$ catalyst and left to dry, then pulled into pipettes of desired geometry. Carbon was grown within the pipette using chemical vapor deposition (CVD). (**b**) A SEM image of the tip of a CRNP, scale bar is 20 nm.

To determine injection volume of our CRNPs, we injected fluorescent dextran into a glycerol droplet (Materials and Methods) (Fig. 4.2a and b). By measuring the fluorescence intensity

immediately after injection, the injection volume was estimated to be ~10 femtoliters (fL), representing ~0.1% of the total embryo volume. Multiple injections from the same CRNP resulted in consistent injection volumes. To facilitate the injection procedure into an embryo, we used larger quartz 'holding' pipettes to allow withdrawal of the CRNP from the embryo after drug delivery, as presented in Fig. 4.2c and d. The CRNP can be used for repeated injections over the course of days by purging the contents and storing the pipettes in a humid chamber.

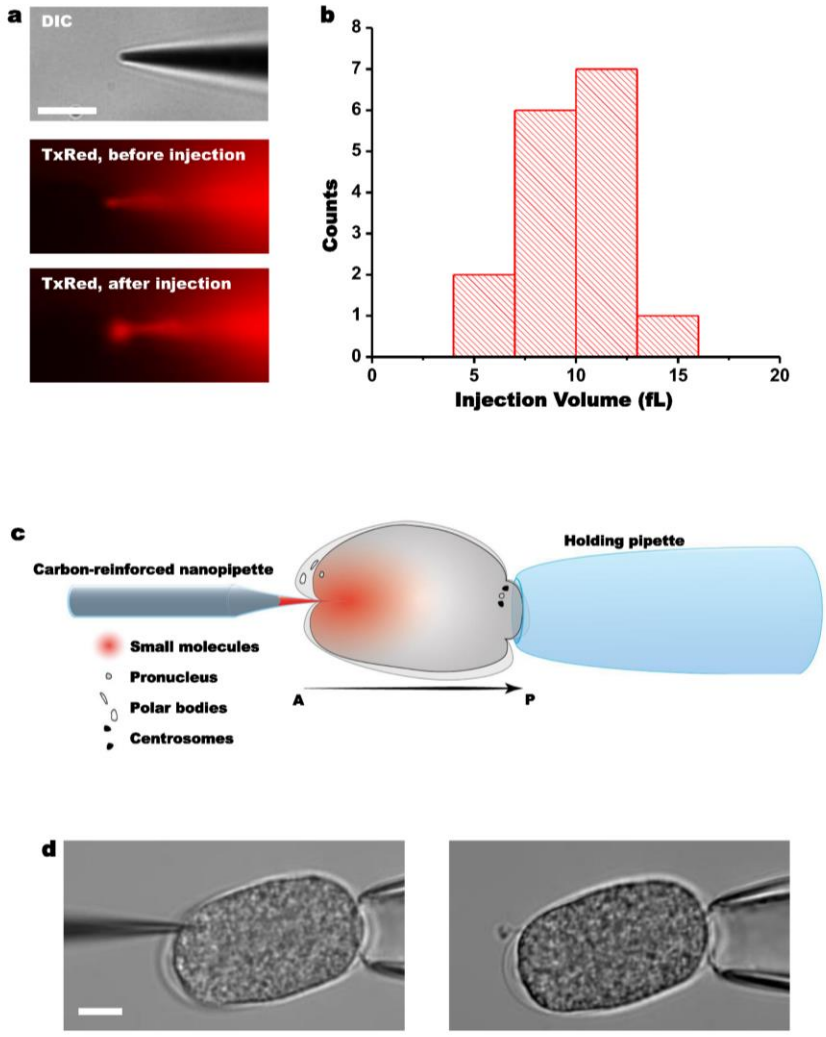

Figure 4.2: CRNP injection characterization and experimental configuration.

(**a**) Characterization of injection volume. A differential interference contrast (DIC) image of a CRNP and fluorescence images before injection of dextran-TxRed into a droplet of glycerol and immediately after the injection. (**b**) Histogram of injection volume from multiple injections using one representative CRNP. (**c**) A cartoon and a (**d**) DIC image of the experimental configuration for embryo injection. A quartz holding pipette was used to immobilize the embryo during injection. Light suction applied through the holding pipette also allowed for the withdrawal of

the CRNP. In all figures, unless otherwise stated, $t = 0$ is defined as the beginning of meiosis II, injection occurs at t ≈ 0:15, anterior is to the left, and scale bars are 10 μm.

As a demonstration of the injection procedure, we injected the DNA intercalating dye, 4',6' diamidino-2-phenylindole dihydrochloride (DAPI), into early one-cell embryos. To ascertain whether these injections perturbed cellular development, the cell cycle, actomyosin contractility, and embryo polarization were monitored in embryos expressing the transgenes GFP::histone 2B (H2B), non-muscle myosin (NMY-2)::GFP, and mCherry::PAR-2 (Fig. 3; $N = 6$). Neither the UV excitation of DAPI, nor occasional cytoplasmic leakage that occurred upon CRNP withdrawal had any measureable effects on cell cycle events, polarity establishment, or cytokinesis. DAPI was observed to co-localize with GFP::H2B (Fig. 4.3, white arrowheads) indicating successful injection. Over time the DAPI signal diminished, likely due to photobleaching and dilution of the dye as the pronuclei swelled. Our successful injection of DAPI demonstrated that small molecules could be successfully introduced into the cell via CRNPs without perturbing cellular integrity or development (6 out of 6 embryos).

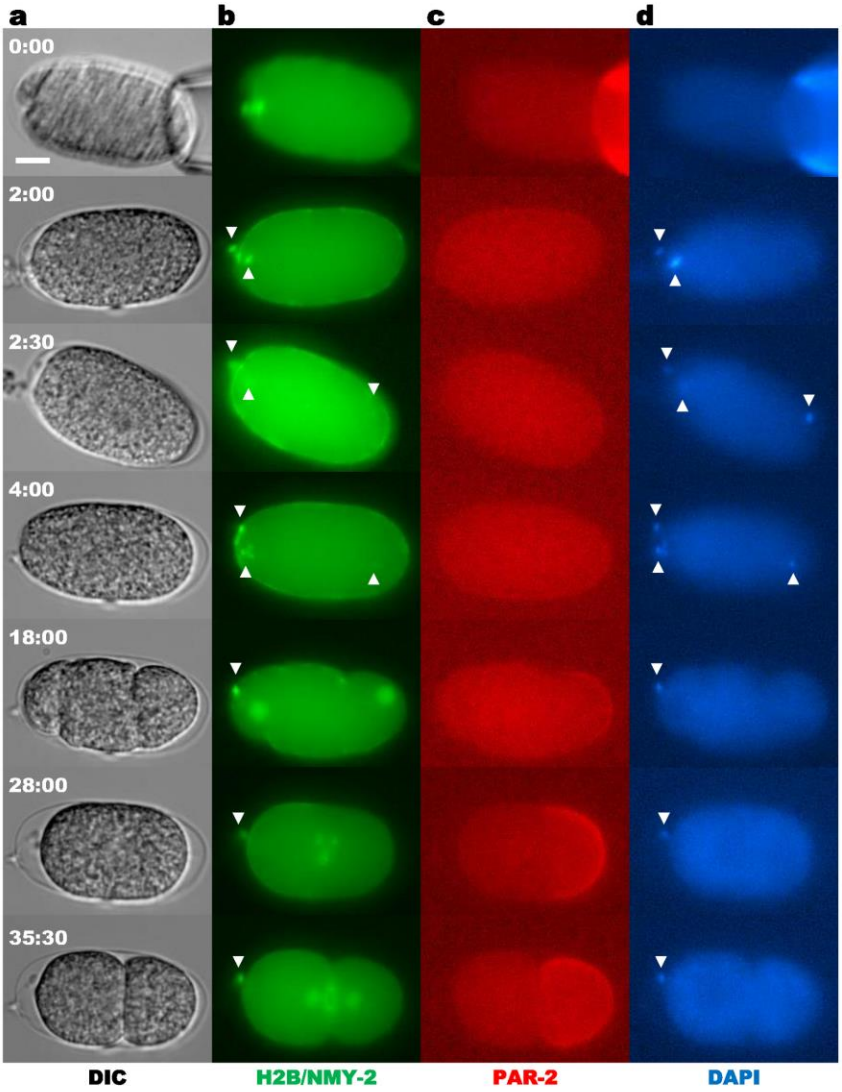

Figure 4.3: Injection of DAPI into a *C. elegans* embryo.

Embryo injected with 0.2 mg/mL DAPI ($N = 6$). (**a**) DIC images. Fluorescence images of (**b**) NMY-2::GFP/ GFP::H2B, (**c**) mCherry::PAR-2, and (**d**) DAPI. White arrowheads indicate co-localization of H2B and DAPI.

In order to test whether our technique could be applied to individual cells at later developmental stages, we also injected two-cell and four-cell embryos with the fluorescent dye YOYO-1. YOYO-1 is membrane impermeable [34], and thus should remain confined to the injected blastomere and segregate to its descendants in subsequent cell divisions. YOYO-1 injected via CRNPs into single blastomeres of two-cell or four-cell stage embryos is exclusively localized within the injected cell (Figure 4.4; N= 5 for 2-cell stage, N= 4 for 4-cell stage). These embryos can complete embryogenesis and hatch into L1 larvae.

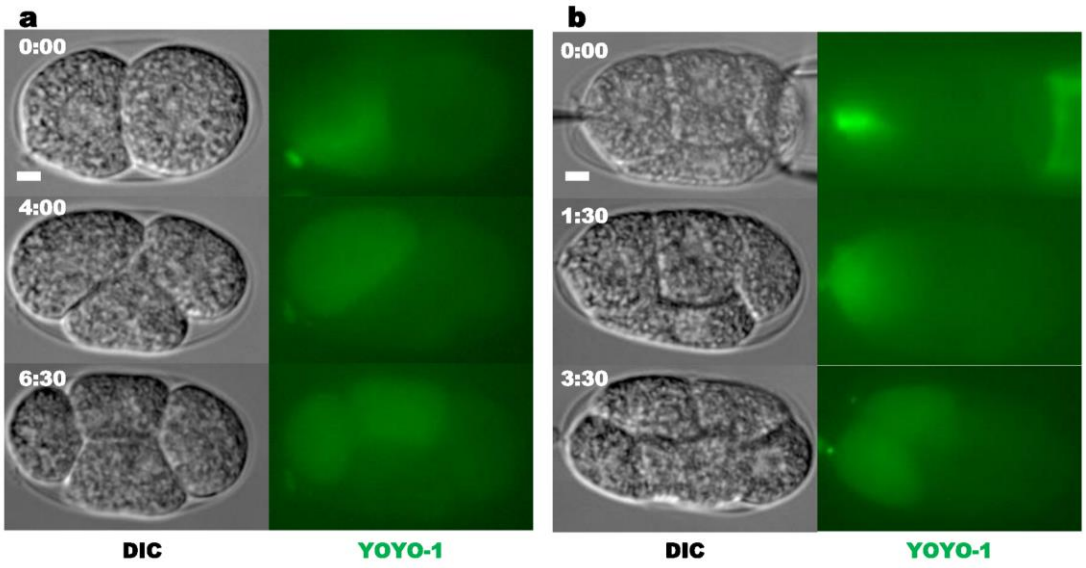

Figure 4.4: Injection of YOYO-1 into multi-cell embryos.

(a) Two-cell embryo in which the P1 blastomere has been injected with 1 μM YOYO-1. (**b**) Four-cell embryo in which the ABa blastomere has been injected with 1 μM YOYO-1 .

Microfilament depolymerization inhibits embryo polarization

To further test whether our CRNP injection technique can deliver specific inhibitors in a controlled manner, we chose to inject Latrunculin A into the early embryo, at a time point before polarity is initiated. LatA sequesters actin monomers, reducing the concentration of free actin and effectively inhibiting microfilament polymerization [35]. The temporal correlation between actomyosin clearing in the posterior and PAR-2 localization originally prompted the hypothesis that actomyosin contractility plays a role in embryonic polarity [2,3,8,36]. Classical experiments by Strome and Wood in 1983 first demonstrated that microfilaments were essential for some aspects of polarity, including segregation of germline granules [21]. Additional genetic and biochemical work has also indicated cross-talk between the actomyosin network and PAR proteins [2,37,38,39,40,41,42]. However, other work has suggested the existence of a secondary, microtubule-mediated, polarization pathway [15,43]. We used CRNP mediated drug delivery to re-examine the role of microfilaments in polarity establishment.

We injected LatA into single-cell embryos expressing GFP::H2B, NMY-2::GFP, and mCherry::PAR-2, at meiosis II, before polarization of PAR proteins is initiated. Injections of either 60 or 90 μM LatA resulted in loss of cortical contraction, no pseudocleavage, and failed cytokinesis, as well as failure to properly localize PAR-2 (Fig. 4.5b and c). PAR-2 localization showed a clear LatA dosage dependence, with localization patterns falling into three categories: accumulation of PAR-2 exclusively at the cortex (similar phenotype to the control), PAR-2 accumulation at both the cortex and centrosome (moderate phenotype) (Fig. 4.5b), and PAR-2 accumulation exclusively at the centrosome (strong phenotype) (Fig. 4.5c). As delineated in Fig. 5d, increasing LatA injection concentration shifted the distribution towards stronger phenotypes. The injection of 60 μM LatA resulted in nearly equal numbers of embryos with moderate and

strong phenotypes. Increasing the concentration of LatA to 90 μM resulted in a predominance of embyros with the strong phenotype (Fig. 4.5d). At the injection concentration of 90 μM, four out of thirteen embryos arrested before pronuclear migration, suggesting this dose was near the threshold of LatA toxicity. These embryos were excluded from further analysis. 8 out of 9 of the surviving embryos exhibited PAR-2 accumulation exclusively at the centrosomes, instead of proper posterior cortical localization. Our PAR-2 localization observations are in agreement with those previously reported for LatA [38], although the strong phenotype we observe is more extreme. Our ability to carefully titrate the drug dosage has revealed subtle dynamics of cortical PAR-2. At the 60 μM LatA concentration, PAR-2 was capable of initially localizing to the cortex but over time moved to the centrosomes (Fig. 4.5b).

We also assessed the ability of PAR-6 to localize appropriately following LatA treatment (Fig. 4.6). In control embryos, PAR-6 was initially present around the entire cortex and then receded to the anterior end, concurrent with cortical flows and posterior cortical smoothing (9 out of 9 embryos; Fig. 4.6a). After injection of LatA, no polarization was observed: PAR-6 remained throughout the cortex (Fig.4.6b and c) correlating with the absence of PAR-2 at the posterior (Fig. 4.5c). Thus LatA treatment does not perturb any process required for PAR-6 cortical accumulation. In 5 out of 8 embryos injected with 60 μM LatA and 5 out of 5 embryos injected with 90 μM LatA, PAR-6 also showed weak accumulation at the centrosomes. Our observations support the conclusion that a functional actin network is necessary for the active segregation of PAR-6 to the anterior cortex, allowing the subsequent loading of PAR-2 onto the posterior cortex.

Figure 5

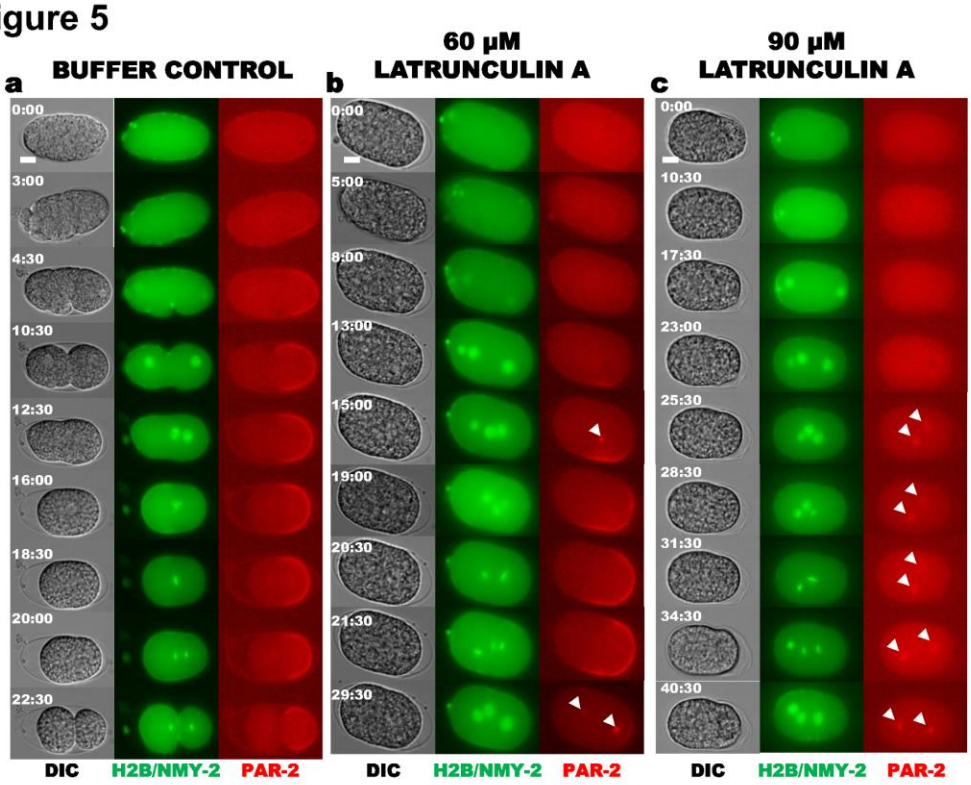
a
BUFFER CONTROL
b
60 µM
LATRUNCULIN A
c
90 µM
LATRUNCULIN A
0:00
3:00
4:30
10:30
12:30
16:00
18:30
20:00
22:30
0:00
5:00
8:00
13:00
15:00
19:00
20:30
21:30
29:30
0:00
10:30
17:30
23:00
25:30
28:30
31:30
34:30
40:30
DIC
H2B/NMY-2
PAR-2
DIC
H2B/NMY-2
PAR-2
DIC
H2B/NMY-2
PAR-2

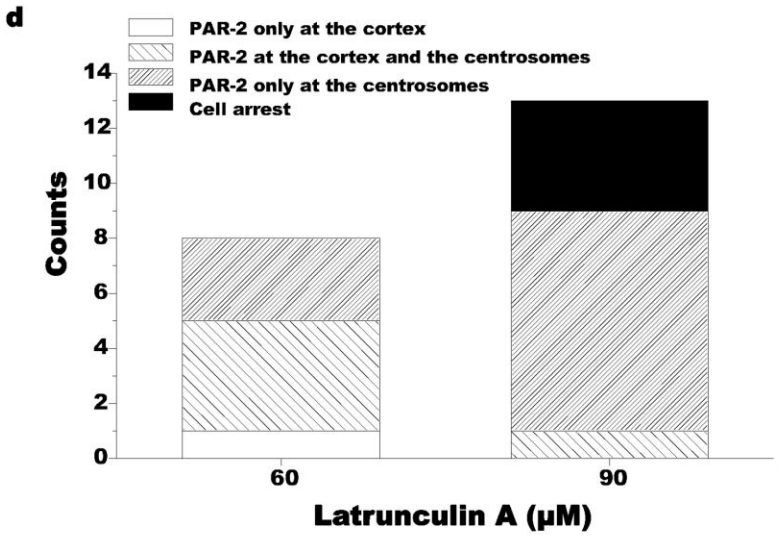
d
PAR-2 only at the cortex
PAR-2 at the cortex and the centrosomes
PAR-2 only at the centrosomes
Cell arrest
Counts
0
2
4
6
8
10
12
14
60
90
Latrunculin A (µM)

Figure4.5: Effect of Latrunculin A concentration on PAR-2 localization.

(**a**) Control with injection buffer containing 3.75 % DMSO in 0.8x EB (*N* = 10). (**b**) Injection of 60 μM LatA (*N* = 8). Shown is an example embryo in which PAR-2 localized at both the cortex and the centrosomes. (**c**) Injection of 90 μM LatA (*N* = 13). Shown is an example embryo with PAR-2 localization at the centrosomes only. For each panel, columns from left to right: DIC; NMY2::GFP/GFP::H2B, and mCherry::PAR-2. In some images, only one centrosome is in focus. (**d**) Distribution of PAR-2 localization phenotypes after injection of 60 μM or 90 μM LatA. In this and all subsequent figures, rows of images are aligned by nuclear dynamics, as assessed by GFP::H2B.

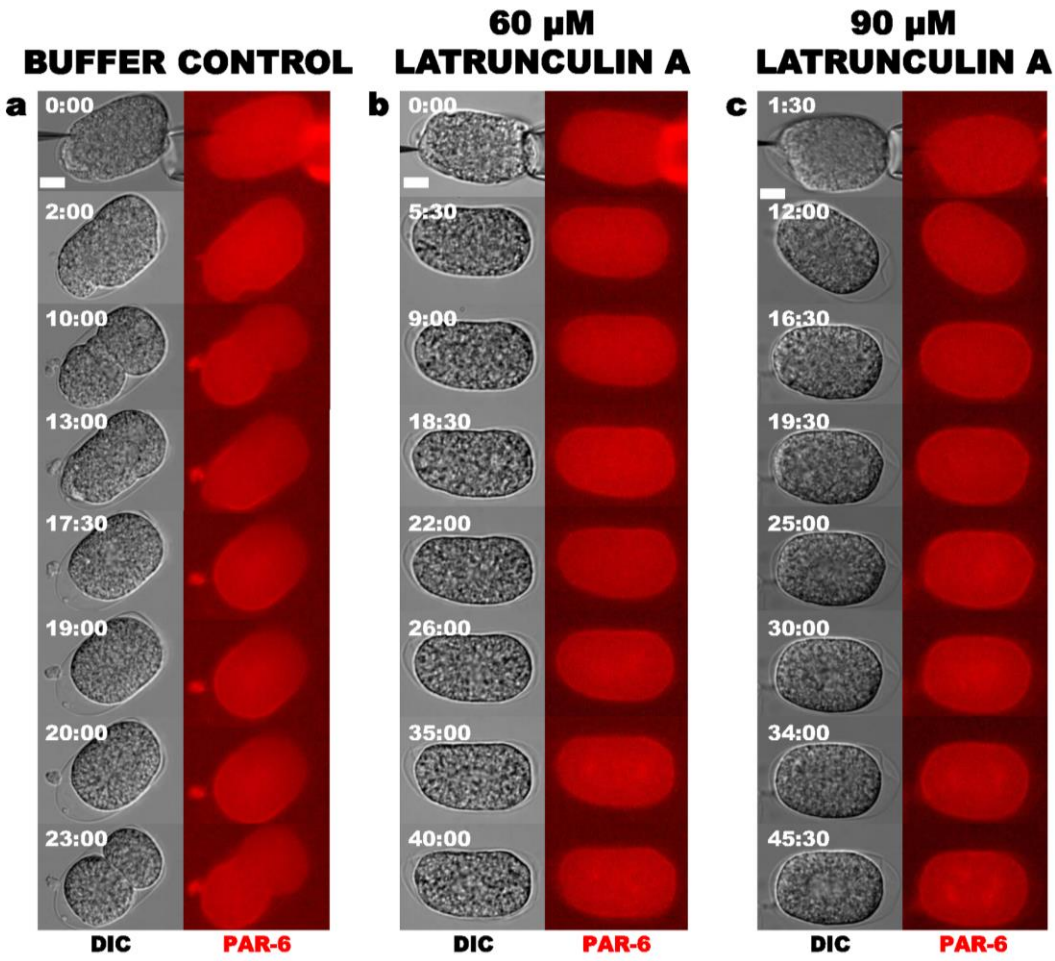

Figure 4.6: Effect of Latrunculin A on PAR-6 localization.

(**a**) Control with injection buffer containing 3.75 % DMSO (*N* = 9). (**b**) Injection of 60 µM (*N* = 10) and (**c**) 90 µM (*N* = 5) LatA. In each panel, DIC is on the left and PAR-6::mCherry is on the right

In order to determine whether microfilaments might play a direct role in cortical PAR-2 localization, we combined *par-6* RNAi depletion with 90 μM LatA injections. In single-cell embryos depleted of PAR-6, without LatA treatment, PAR-2 localized uniformly throughout the cortex ($N = 5$) (Fig. 4.7a) consistent with the known role for anterior PAR proteins in excluding PAR-2 from the cortex [7,8,9,44,45]. Injection of 90 μM LatA, following the completion of meiosis II, into *par-6* RNAi embryos, had no additional effect on cortical PAR-2 localization; PAR-2 localized to the entire cortex (4 out of 4 embryos; Fig. 4.7b). Thus LatA does not prevent PAR-2 from associating with the cortex, but rather interferes with the proper clearing of PAR-6 from the posterior cortex. Our experiments suggest that in LatA-treated embryos, the uniform distribution of the anterior PARs prevents PAR-2 from localizing to the cortex. In embryos with PAR-6 but lacking microfilaments, PAR-2 then localizes to the centrosomes by default perhaps due to its ability to bind microtubules [15].

Because our treatments with LatA resulted in failure to establish polarity, we also treated embryos expressing GFP-tagged beta-tubulin (GFP::TBB-2) with LatA to determine whether our LatA injections might compromise the microtubule system in addition to microfilaments, but we observed no detectable difference in microtubule morphology (7 out of 7 embryos; Fig. 4.8). The orientation of anaphase showed no deviation from control embryos indicating that microtubules were still capable of stably anchoring to the cortex. This indicates that when the microfilament system is severely compromised by LatA, microtubules remain intact but are not sufficient to initiate cortical PAR-2 localization.

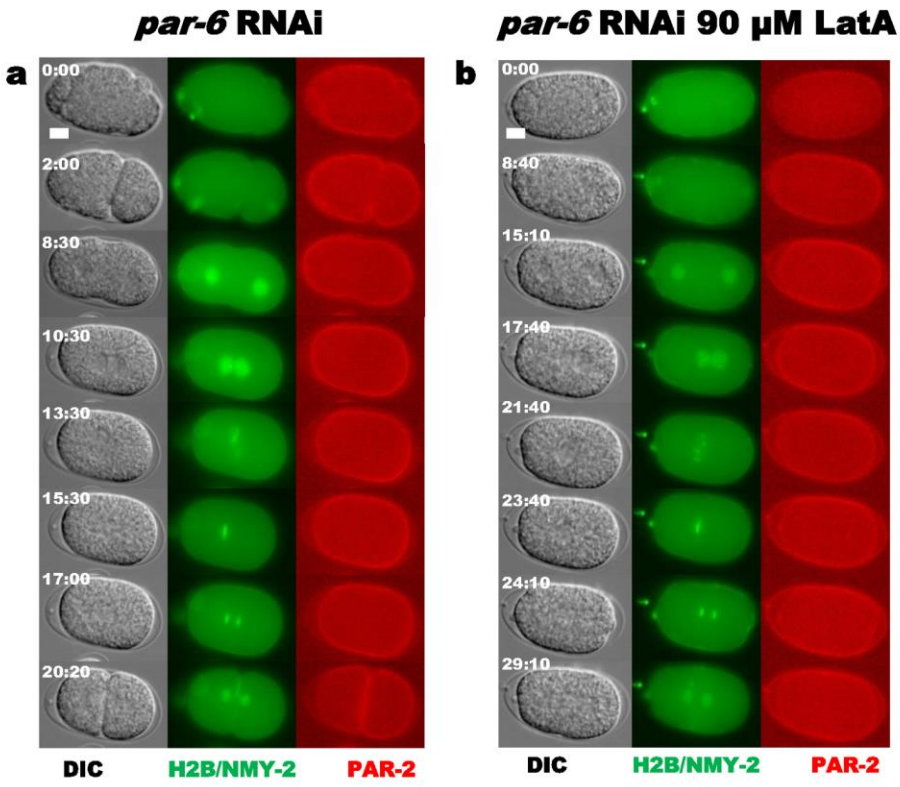

Figure 4.7: Effect of Latrunculin A on PAR-2 localization in PAR-6-depleted embryos.

(**a**) *par-6* RNAi treatment for 24 hr (*N* = 5). (**b**) *par-6* RNAi treatment for 24 hr combined with 90 µM LatA injection following meiosis II (*N* = 4). For each panel, columns from left to right: DIC, NMY-2::GFP/ GFP::H2B and PAR-2::mCherry.

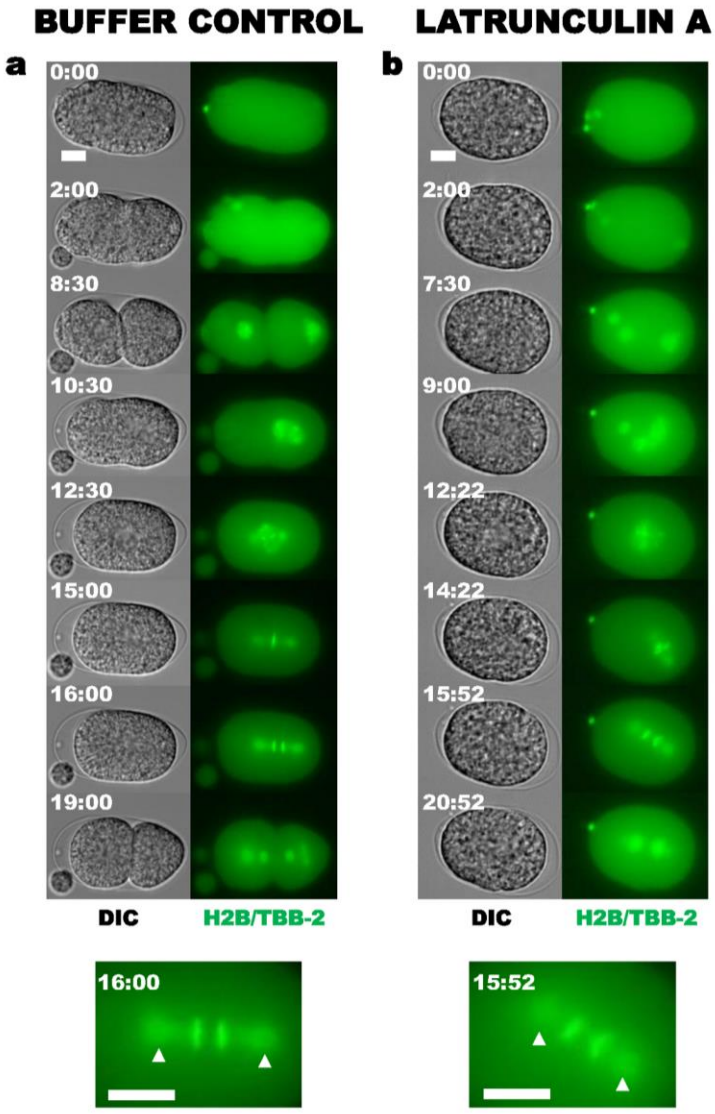

Figure 4.8: Effect of Latrunculin A treatment on microtubule formation.

(**a**) Control with injection buffer containing 3.75 % DMSO (*N* = 8). (**b**) Injection of 60 µM LatA (*N* = 7). In each panel, DIC is on the left and GFP::H2B/ GFP::TBB-2 is on the right. Below each panel is an enlargement showing the maximal size of GFP::TBB-2 at the centrosomal region, indicated by the white arrowheads.

DISCUSSION

The use of carbon-reinforced nanopipettes to penetrate the durable eggshells of single-celled *C. elegans* embryos has provided a new technique with which to examine a very specific developmental event: the earliest stage of polarity establishment. By injecting well-defined doses of drugs that target the microtubule or microfilament cytoskeleton, we found that CRNPs are exceptional tools to investigate the development of *C. elegans* embryos in a temporally controlled manner and that the procedure itself does not perturb early embryonic development.

There are a number of advantages of CRNPs over existing techniques for circumventing the robust permeability barrier to expose *C. elegans* embryos to small molecules. A common existing technique is pressure-permeabilization, or 'popping', of the eggshell. In order for embryos to survive this technique the eggshell must be fully formed prior to the application of pressure to the embryo thus limiting how early embryos can be experimentally manipulated. CRNP injection extends the window of time that is experimentally accessible. Each injection takes approximately 30 seconds from initial piercing of the embryo to the retrieval of the pipette, allowing for rapid experimental manipulation. A second, similar, method for embryo permeabilization is laser perforation of the eggshell [46]. Both methods rely on the diffusion of small molecules in the surrounding buffer into the embryo. The advantage of injection over this method is the ability to easily titrate the drug dosage. This can be difficult to do with the current diffusion-dependent methods as it is unclear whether the embryos equilibrate with the surrounding media or if a more complex drug diffusion process occurs. As we have shown (Fig. 5), CRNPs allow titration of the molecule concentration for the assessment of a range of phenotypes. A third method for permeabilizing the eggshell is to utilize RNAi to generate "leaky eggshells"[25,26]. Some proteins that, when depleted, result in permeabilized embryos have also

been implicated in embryo polarization and thus their knockdown may complicate studies of polarity establishment [37,47,48], reviewed by Johnston and Dennis [49]. The use of RNAi to create a permeable eggshell may also interfere with RNAi knockdown of additional targets, as combined RNAi can dilute depletion efficiency [50]. In principle, our CRNP technique could be used to introduce any number of drugs in combination with RNAi (Fig. 4.6). Direct injection with micropipettes also allows delivery of a wider range of molecules than does iontophoresis, which requires a current to move small, charged molecules into the cell [51]. CRNPs are much stronger than conventional glass micropipettes and their hydrophilic lining facilitates transfer of aqueous solutions into cells by pressure-driven injection.

Polarity establishment in *C. elegans* provided a precise time point in which to establish CRNPs as a viable tool for cell biology. The fine temporal control of injection by CRNPs, coupled with live cell imaging, permitted us to take a closer look at the very early developmental time in which polarity is established. Our experiments reinforce a required role for microfilaments in polarity establishment and suggest that astral microtubules are not sufficient to establish polarity in the absence of actomyosin-mediated cortical reorganization.

When microfilaments were disrupted immediately following meiosis II by injection of a high dosage of LatA (90 μM), PAR-2 was unable to accumulate at the cortex and instead localized to the centrosomes (Fig. 4.5), confirming that microfilaments are necessary for the initial establishment of the cortical PAR-2 domain [38]. Our examination of PAR-6 localization following LatA injection indicates that exclusion of PAR-2 from the cortex is most likely due to a failure to clear PAR-6 from the posterior cortex (Fig. 6 and 7). The ability of PAR-2 to stably

localize to the cortex in embryos depleted of PAR-6 by RNAi even after LatA treatment lends further support to mutual exclusion between anterior and posterior polarity proteins in models of polarity establishment. Additionally, these experiments demonstrate that microfilament depolymerization disturbs neither the ability of PAR proteins to bind the cortex, nor the ability of the anterior proteins to exclude PAR-2 from the cortex (Fig.4. 6 and 4.7). Consistent with our findings, uniform retention of PAR-6 or PAR-3 at the cortex has been observed when NMY-2 is compromised by RNAi depletion [8,52]. Our LatA experiments have shown that disruption of the microfilaments' ability to initiate PAR-6 clearing results in complete failure of PAR-2 to access the posterior cortex. This is consistent with models for polarity in which actomyosin flows transport PAR-3/PAR-6/PKC-3 to the anterior of the zygote to initiate their asymmetric localization, and the resulting nascent PAR-2 domain maintains that asymmetry [2]. However, the stronger effect of LatA on polarity establishment than that produced by *mlc-4* RNAi treatment [15,38,43] may suggest that actin microfilaments or actin-associated proteins direct polarity establishment by a means other than simply regulating actomyosin contractility.

The results of our LatA treatments do not support a model in which microtubules direct the self-organization of PAR asymmetry independently of actin dynamics in the *C. elegans* embryo. Other studies, using *mlc-4* RNAi treatment, have suggested that in the absence of actomyosin contractility, microtubules can facilitate cortical loading of PAR-2 by protecting PAR-2 from phosphorylation by PKC-3 [15,43]. However, we have found that when the actin cytoskeleton is severely disrupted by 90 μM LatA treatment, even fully intact microtubules are not sufficient for stable accumulation of PAR-2 at the cortex (Fig. 4.4). Although it is possible that at this concentration we are seeing off-target effects of the drug, these results suggest that microtubule-

directed polarity establishment in *C*. *elegans* requires intact microfilaments. This raises two possibilities: 1) that residual low levels of actomyosin contractility after *mlc-4* RNAi are sufficient to facilitate microtubule-dependent loading of PAR-2 or 2) that a role for actin filaments that is independent of myosin contractility is required for PAR-2 loading.

We anticipate that CRNP injection may find broad applications in future studies of *C*. *elegans* early embryonic development because of its ability to precisely target a specific developmental stage. Although our current application focuses on the single-cell *C*. *elegans* embryo, the sharp and strong CRNPs are capable of precise penetration through the eggshells of nematode embryos at any developmental stage and could also be applied for injection into other types of cells with tough coverings. With minimal modification to CRNPs, intracellular spatial control could also be achieved by using functionalized nanoparticles or liposomes to deliver drugs of interest [53]. Our injection method using CRNPs, which minimizes cellular damage while allowing precise manipulation, should be adaptable for a wide range of further applications in cell biology.

REFERENCES

1. Gönczy P, Rose LS (2005) Asymmetric cell division and axis formation in the embryo. In: Community TCeR, editor. WormBook: WormBook.
2. Munro E, Nance J, Priess JR (2004) Cortical flows powered by asymmetrical contraction transport PAR proteins to establish and maintain anterior-posterior polarity in the early *C. elegans* embryo. Developmental Cell 7: 413-424.
3. Cheeks RJ, Canman JC, Gabriel WN, Meyer N, Strome S, et al. (2004) *C. elegans* PAR proteins function by mobilizing and stabilizing asymmetrically localized protein complexes. Current Biology 14: 851-862.
4. Etemad-Moghadam B, Guo S, Kemphues K (1995) Asymmetrically distributed PAR-3 protein contributes to cell polarity and spindle alignment in early *C. elegans*. Cell 83: 743-752.
5. Hung TJ, Kemphues KJ (1999) PAR-6 is a conserved PDZ domain-containing protein that colocalizes with PAR-3 in Caenorhabditis elegans embryos. Development 126: 127-135.
6. Tabuse Y, Izumi Y, Piano F, Kemphues KJ, Miwa J, et al. (1998) Atypical protein kinase C cooperates with PAR-3 to establish embryonic polarity in Caenorhabditis elegans. Development 125: 3607-3614.
7. Boyd L, Guo S, Levitan D, Stinchcomb DT, Kemphues KJ (1996) PAR-2 is asymmetrically distributed and promotes association of P granules and PAR-1 with the cortex in *C. elegans* embryos. Development 122: 3075-3084.
8. Cuenca A, Schetter A, Aceto D, Kemphues K, Seydoux G (2003) Polarization of the *C. elegans* zygote proceeds via distinct establishment and maintenance phases. Development 130: 1255-1265.
9. Hao Y, Boyd L, Seydoux G (2006) Stabilization of cell polarity by the *C. elegans* RING protein PAR-2. Developmental Cell 10: 199-208.
10. Cowan CR, Hyman AA (2007) Acto-myosin reorganization and PAR polarity in *C. elegans*. Development 134: 1035-1043.
11. Nance J, Zallen JA (2011) Elaborating polarity: PAR proteins and the cytoskeleton. Development 138: 799-809.
12. Noatynska A, Gotta M (2012) Cell polarity and asymmetric cell division: the *C. elegans* early embryo. Essays in Biochemistry 53: 1-14.
13. Munro E, Bowerman B (2009) Cellular symmetry breaking during Caenorhabditis elegans development. Cold Spring Harbor Perspectives in Biology 1: a003400.
14. Wallenfang MR, Seydoux G (2000) Polarization of the anterior-posterior axis of *C. elegans* is a microtubule-directed process. Nature 408: 89-92.
15. Motegi F, Zonies S, Hao Y, Cuenca AA, Griffin E, et al. (2011) Microtubules induce self-organization of polarized PAR domains in Caenorhabditis elegans zygotes. Nature Cell Biology 13: 1361-1367.
16. Tsai MC, Ahringer J (2007) Microtubules are involved in anterior-posterior axis formation in *C. elegans* embryos. Journal of Cell Biology 179: 397-402.
17. O'Connell KF, Maxwell KN, White JG (2000) The *spd-2* gene Is required for polarization of the anteroposterior axis and formation of the sperm asters in the Caenorhabditis elegans zygote. Developmental Biology 222: 50-77.
18. Olson SK, Greenan G, Desai A, Müller-Reichert T, Oegema K (2012) Hierarchical assembly of the eggshell and permeability barrier in *C. elegans*. Journal of Cell Biology 198: 731-748.
19. Edgar LG (1995) Blastomere Culture and Analysis. Methods in Cell Biology 48: 303-321.
20. Chitwood BG, Chitwood MB (1974) Introduction to Nematoade. Baltimore, MD: University Park Press.
21. Strome S, Wood WB (1983) Generation of asymmetry and segregetion of germ-line granules in early *C. elegans* embryos. Cell 35: 15-25.

22. Hyman AA, White JG (1987) Determination of cell division axes in the early embryogenesis of Caenorhabditis elegans. Journal of Cell Biology 105: 2123-2135.
23. Hill D, Strome S (1990) Brief cytochalasin-induced disruption of microfilaments during a critical interval in 1-cell *C. elegans* embryos alters the partitioning of developmental instructions to the 2-cell embryo. Development 108: 159-172.
24. Lee JY, Goldstein B (2003) Mechanisms of cell positioning during *C. elegans* gastrulation. Development 130: 307-320.
25. Carvalho A, Olson SK, Gutierrez E, Zhang K, Noble LB, et al. (2011) Acute drug treatment in the early *C. elegans* embryo. PLOS One 6: e24656.
26. Goehring NW, Hoege C, Grill SW, Hyman AA (2011) PAR proteins diffuse freely across the anterior-posterior boundary in polarized *C. elegans* embryos. Journal of Cell Biology 193: 583-594.
27. Bossinger O, Schierenberg E (1992) Cell-cell communication in the embryo of Caenorhabditis elegans. Developmental Biology 151: 401-409.
28. Bossinger O, Schierenberg E (1996) Cell-cell communication in nematoad embryos: differences between Cephalobus spec. and Caenorhabditis elegans. Development Genes and Evolution 206: 25-34.
29. Zhang Y, Yu L (2008) Single-cell microinjection technology in cell biology. BioEssays 30: 606-610.
30. Zhang Y (2007) Microinjection technique and protocol to single cells.
31. Laffafian I, Hallette MB (1998) Lipid-assisted microinjection: intoducing material into the cytosol and membranes of small cells. Biophysical Journal 75: 2558-2563.
32. Schrlau MG, Falls EM, Ziober BL, Bau HH (2008) Carbon nanopipettes for cell probes and intracellular injection. Nanotechnology 19: 015101.
33. Schrlau M, Brailoiu E, Patel S, Gogotsi Y, Dun N, et al. (2008) Carbon nanopipettes characterize calcium release pathways in breast cancer cells. Nanotechnology 19: 325102.
34. Wood EJ (1994) Molecular probes: Handbook of fluorescent probes and research chemicals: By R P Haugland. Biochemical Education 22: 83-83.
35. Coué M, Brenner SL, Spector I, Korn ED (1987) Inhibition of actin polymerization by latrunculin A. FEBS Letters 213: 316-318.
36. Hird SN, White JG (1993) Cortical and cytoplasmic flow polarity in early embryonic cells of Caenorhabditis elegans. Journal of Cell Biology 121: 1343-1355.
37. Rappleye CA, Paredez AR, Smith CW, McDonald KL, Aroian RV (1999) The coronin-like protein POD-1 is required for anterior-posterior axis formation and cellular architecture in the nematode Caenorhabditis elegans. Genes & Development 13: 2838-2851.
38. Severson AF, Bowerman B (2003) Myosin and the PAR proteins polarize microfilament-dependent forces that shape and position mitotic spindles in Caenorhabditis elegans. Journal of Cell Biology 161: 21-26.
39. Schonegg S, Hyman AA (2006) CDC-42 and RHO-1 coordinate acto-myosin contractility and PAR protein localization during polarity establishment in *C. elegans* embryos. Development 133: 3507-3516.
40. Shelton C, Carter J, Ellis G, Bowerman B (1999) The nonmuscle myosin regulatory light chain gene mlc-4 is required for cytokinesis, anterior-posterior polarity, and body morphology during Caenorhabditis elegans embryogenesis. Journal of Cell Biology 146: 439-451.
41. Velarde N, Gunsalus KC, Piano F (2007) Diverse roles of actin in *C. elegans* early embryogenesis. Biomedical Central Developmental Biology 7.
42. Kirby C, Kusch M, Kemphues K (1990) Mutations in the par genes of Caenorhabditis elegans affect cytoplasmic reorganization during the first cell cyle. Developmental Biology 142: 203-215.
43. Zonies S, Motegi F, Hao Y, Seydoux G (2010) Symmetry breaking and polarization of the *C. elegans* zygote by the polarity protein PAR-2. Development 137: 1669-1677.

44. Watts J, B E-M, S G, Boyd L, BW D, et al. (1996) *par-6*, a gene involved in the establishment of asymmetry in early *C. elegans* embryos, mediates the asymmetric localization of PAR-3. Development 122: 3133-3140.
45. Goehring N, Trong P, Bois J, Chowdhury D, Nicola E, et al. (2011) Polarization of PAR proteins by advecitve triggering of a pattern-forming system. Science 334: 1137-1141.
46. Severson AF, Baillie D, Bowerman B (2002) A formin homology protein and a profilin are required for cytokinesis and Arp 2/3-independent assembly of cortical microfilaments in the early Caenorhabditis elegans embryogenesis. Current Biology 12: 2066-2075.
47. Tagawa A, Rappleye CA, Aroian RV (2001) *pod-2*, along with *pod-1*, defines a new class of genes required for polarity in the early Caenorhabditis elegans. Developmental Biology 233: 412-424.
48. Johnston WL, Kirzus A, Dennis JW (2006) The eggshell is required for meiotic fidenity, polar-body extrusion, and polarization of the *C. elegans* embryo. BioMed Central Biology 4.
49. Johnston WL, Dennis JW (2012) The eggshell in the *C. elegans* oocyte-to-embryo transition. Genesis 50: 333-349.
50. Gönczy P, Echeverri C, Oegema K, Coulson A, Jones SJ, et al. (2000) Functional genomic analysis of cell division in *C. elegans* using RNAi of genes on chromosome III. Nature 406: 331-336.
51. Stone T (1985) Microiontophoresis and pressure ejection. Chinchester: Wiley.
52. Guo S, Kemphues KJ (1996) A non-muscle myosin required for embryonic polarity in Caenorhabditis elegans. Nature 382: 455-458.
53. Wang X, Guo Z (2013) Targeting and delivery of platinum-based anticancer drugs. Chemical Society Reviews 42: 202-224.

CHAPTER 5

EXPERIMENTAL PERSPECTIVES

Implications for future studies

The convergence of *in vitro* and *in vivo* studies on DNA replication and its coordination with nucleosome inheritance is still a work in progress. *In vitro* work points towards distinct pathways for nascent and parental histone deposition and the possibility for a chaperone independent pathway of parental nucleosome inheritance. *In vivo* work has helped to characterize the chromatin landscape following DNA replication, but falls short of defining a mechanistic pathway due to the inherent complexity of the replication fork. As *in vivo* assays approach single-cell or single locus resolution and *in vitro* assays continue to mature in their ability to recapitulate DNA replication our understanding of the mechanisms that underlie epigenetic inheritance is rapidly growing.

***In vivo* studies**

In general, *in vivo* studies have focused on characterizing nascent chromatin following a deletion of a gene or treatment of cells with various replication-targeting drugs. Such studies have provided insight into the roles for specific proteins in forming and maintaining chromatin behind the replication fork. Studies that allow differentiation of parental and nascent histones provide a direct measurement of the heritable nucleosome components[1-4] and the overall partitioning of new and old histones between the daughter strands[5-9]. Measuring the position of old histones along the DNA with respect to their original position provides insight into the changes in chromatin organization that occur during S-phase[7]. Such studies have laid the ground work for additional exploration into how histone inheritance may be coordinated with a cell's transcriptional program and developmental trajectory.

Partitioning histones to the daughter strands

Early studies of nucleosome partitioning to daughter DNA strands showed that parental nucleosomes are divided approximately equally between the nascent DNA[5,6,8,9] giving rise to the hypothesis that histone modifications are then copied laterally to nearby nascent histones[10]. Such studies have been repeated using mini-chromosomes replicated by the SV40 system both in vivo and vitro, always producing the same results of equal distribution to the daughter DNA[11-15]. Such observations generally rules out a model where old and new histones are asymmetrically divided between the daughter chromosomes. However, such studies have not examined locus specific partitioning or if there is a local preference within replicons that may be driven by the differential processing of the leading and lagging strands.

Recently two special cases of asymmetric histone partitioning have been described indicating that there may be controllable pathways that may drive strand-specific histone partitioning. First is in the division of drosophila germline progenitor cells to give rise to a gonialblast cell and a progenitor cell[16]. Second is in the generation of bilateral neuron asymmetry in *C. elegans*[17]. Perhaps not surprisingly, both of these examples come from asymmetric cell divisions that are a hallmark of organismal development and stem cell divisions. In both of these divisions one cell retains its identity while the other becomes poised for differentiation. Since the genome is invariant in each cell the ability to differentiate (or self-renew) is dictated by changes to genome packaging.

In the drosophila male germline stem cell it has been observed that parental histones are retained in the stem cell and newly synthesized histone are localized to the chromosomes that end up in the daughter gonialblast that will eventually become the spermatids[16]. By setting up the genome for immediate changes to the transcriptional program the newly produced cell are poised for further differentiation. Such a mechanism could also underlie the second example of asymmetric cell division in *C. elegans*[17]. During neurogenesis the ABaraapa and ABaraapp cells which generate pairs, between the two cell, of identical cells except for the unpaired e3D epithelial cell from ABaraapa and the MI neuron from ABaraapp. Through a genetic screen to identify gene that transform MI into e3D, Bruce Stillman's group identified Caf1 as a required proteins in driving the asymmetric division suggesting that nucleosome segregation it a critical determinant for cell differentiation[17]. Although the partitioning of histones was not examined in these cells, asymmetric division of parental histones at genes that drive cellular differentiation could underlie the epigenetic determinates for this developmental event.

These two specific examples could be exceptions to the rule of random histone partitioning or they could point toward a more general trend where highly expressed genes may preferentially retain parental histones to ensure prompt resumption of gene transcription. This could be a feature within early development or at key asymmetric divisions. The partitioning of histones to either strand would directly impact how histone modifications were spread and therefore further research in the reestablishment of chromatin domains following DNA replication may illuminate what is feasible for nucleosome inheritance.

While seemingly a simple observation, it immediately raises some questions about how histones are targeted to a specific daughter DNA strand. One simple explanation, that holds true for gametogenesis in other organisms, is that during or immediately following DNA replication the histone modifications are removed from one strand. In this case, we can imagine a highly controlled feedback pathway that targets one DNA strand for histone-de-modification, perhaps acting through cohesion or mitotic spindle proteins that will ultimately dictate which daughter DNA end up in each cell. However, when new histones are tracked through a fluorescent protein tag it becomes clear that the mechanism is a literal partitioning of old and new histones[16,18]. In order for this to occur, there must be a way for the replication machinery to differentiate between the two strands of DNA to direct histone deposition and transfer. One possible mechanism is through the retention of PCNA and Okazaki fragment processing enzymes that would direct histone deposition to the lagging strand[19]. This possibility poses another conundrum because eukaryotic replication occurs bidirectional from multiple origins of replication. Bidirectional replication results in each daughter DNA strand being composed of both leading and lagging synthesized fragments of approximately 100 kbp [20,21]. In humans, this translates to approximately 500 – 2000 replicons per chromosome and with the average gene length being on the order of 8 kbp (longest is 37.7 kbp) each replicon would encompass multiple genes. Such heterogeneity along each daughter strand poses another logistical challenge in the differentiation between the two resulting chromosomes in a replication dependent manner. One possible solution can be postulated from the observation, in bacteria, that replication primarily occurs co-directionally along highly

transcribed genes[22] and that in eukaryotes there is at correlation between actively transcribed genes and replication timing suggesting that they are coordinated in some way[23-27]. In the case where replication is preferentially co-direction with transcription, the leading strand is the same as the coding strand and the lagging strand would be the template strand. Incorporating this observation into the model, we can then relax the requirement that the entire length of the chromosome have exclusively old or new histones as packaging, but instead limit this requirement to [highly] transcribed genes; potentially those that are especially important for the maintenance of cell identity.

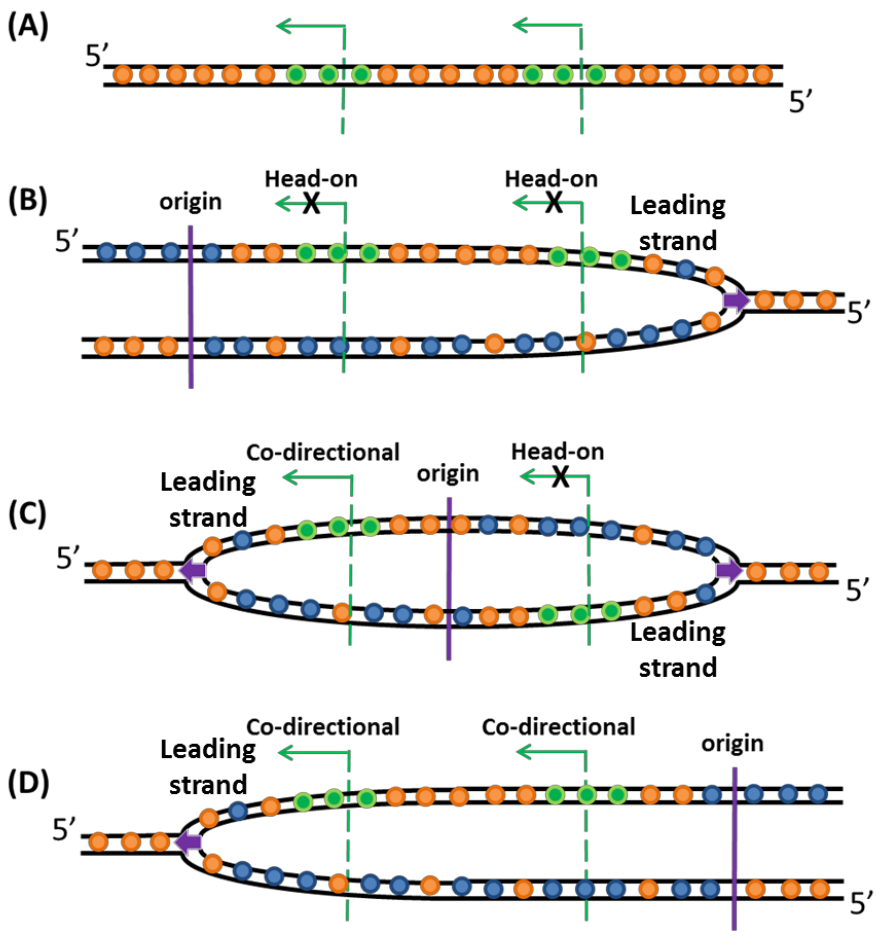

Figure 4.1 **(A)** The promoter-flanking nucleosomes (green) are play a direct role in facilitating active transcription through recruitment of histone remodelers and transcription machinery. Preferential partitioning of parental histones (green and orange) to the leading strand may inhibit or reinforce transcription activity depending on whether replication encountered the gene head-on **(B and C)** or co-directionally **(C and D)**.

It would be of particular interest to further investigate these asymmetric partitioning events with respect to replication origin position, timing, and directionality along the genome. Furthermore, a deeper understanding of how the replisome functions along the leading and lagging strand will provide insight into how one strand could be marked, either by the association of replication proteins, timing, or potentially a more subtle mechanism such as misincorporation of nucleotides.

On top of the basic mechanism for histone transfer and deposition, there is still the outstanding question of whether the positioning of histones behind the replication fork is a major component in epigenetic inheritance. Genome-wide studies have shown that parental histones are found to accumulate at the 5'-end of genes approximately 500 base pairs upstream of the original position[7]. While this would preserve the positioning of histone modifications within the region of the promoter, is begs the question of what stops the spread of histones into the 3' end of neighboring genes potentially disrupting transcription termination sites and facilitating aberrant read through transcription. At a more global level, large scale shifting of chromatin domain boarders could produce gross changes to the nuclear organization of the genome into topological associated domains.

The blurring of histone modification positions is most likely resolved through the action of chromatin remodelers following in the wake of DNA replication. How each of these events is coordinated will require the combination of genome-wide, single cell, and single molecule studies where each one can address a unique component in this extremely complicated system. As genome-wide studies become amenable to smaller sample sizes and single-cell sequencing becomes more robust the field will start to see a convergence in data between high-resolution single molecule experiments and single-cell genome-wide studies.

In vitro studies

To that end, *in vitro* reconstitution of DNA replication has recently become feasible now that the key components of the replisome have been identified and purified. Sequential

addition of accessory proteins, such as FACT and Asf-1 to the replication reactions have more clearly elucidated how these proteins may mediate replication through chromatin[28]. Imaging, with AFM or fluorescence microscopy is a logical next step for such experiments to further discern protein dynamics at the fork.

Additional mechanistic studies on individual components of the replisome, CMG helicase or the polymerases for instance, will also lend a deeper understanding to the functional abilities and limitation of these proteins and how they may contribute to the overall functionality of the replisome. The monitoring of short-lived replication intermediates and the possibility for trapping nucleosome transfer intermediates is much more feasible in a well-defined in vitro system. Similar studies have been carried out in the past to study the transit of RNA polymerase through a nucleosome, where the distribution of products and intermediates were imaged using AFM[29]. A similar study has the potential to shed light on how CMG helicase or the lagging strand polymerase may interact with a nucleosome. Although fluorescent localization studies have reduced special resolution, real-time analysis of protein dynamics along DNA or chromatin have been used to study polymerase recycling at the replication fork[30]. Such experiments have the potential for elucidating co-localization of proteins along nascent DNA in the wake of the replication fork, perhaps illuminating the mechanism that may differentiate leading and lagging strands and thus drive differential processing of the DNA[19].

Characterizing the exact content of nascent chromatin assembled in vitro is also possible utilizing *in vitro* methods, through the use of high-resolution DNA sequencing methods

as well as single molecule manipulation of replication products. The spacing and location of transferred nucleosomes can be very accurately measured via paired-end sequencing or DNA unzipping techniques[31-34], under both *in vivo* and *in vitro* conditions. In the absence of chromatin maturation pathways, such as remodelers and chaperones, this intermediate state of chromatin could be elucidated with high resolution. The effect of transcription factor binding on nucleosome positioning is of particular interest as there are *in vivo* studies suggesting that nucleosomes maintain canonical organization around transcription factor binding sites even in an absence of critical nucleosome remodelers[35,36]. In general, the quantification of reaction kinetics is made possible with *in vitro* reactions and these fundamental measurements will provide insight into how the system coordinates all of is components *in vivo*.

In conclusion, the reconstitution of eukaryotic replication will be essential to dissecting the underlying mechanisms responsible for the coordination of replication and re-chromatinization of the genome. Pairing the in vitro approached with single-cell manipulation has the potential to contextualize the in vitro findings with in the complexities of the cellular environment.

1. Xu, M. et al. Partitioning of histone H3-H4 tetramers during DNA rpelication-dependent chromatin assembly. *Science* **328**(2010).
2. Prior, C.P., Cantor, C.R., Johnson, E.M. & Allfrey, V.G. Incorporation of exogenous pyrene-labeled histone into Physarum chromatin: a system for studying changes in nucleosomes assembled in vivo. *Cell* **20**, 597-608 (1980).
3. Leffak, I.M., Grainger, R. & Weintraub, H. Conservative assembly and segregation of nucleosomal histones. *Cell* **12**, 837-45 (1977).
4. Jackson, V. Deposition of newly synthesized histones: hybrid nucleosomes are not tandemly arranged on daughter DNA strands. *Biochemistry* **27**, 2109-20 (1988).
5. Jackson, V., Granner, D.K. & Chalkley, R. Deposition of histones onto replicating chromosomes. *Proc Natl Acad Sci U S A* **72**, 4440-4 (1975).
6. Russev, G. & Hancock, R. Assembly of new histones into nucleosomes and their distribution in replicating chromatin. *Proc Natl Acad Sci U S A* **79**, 3143-7 (1982).
7. Radman-Livaja, M. & Rando, O.J. Nucleosome positioning: how is it established, and why does it matter? *Dev Biol* **339**, 258-66 (2010).
8. Seale, R.L. Studies on the mode of segregation of histone nu bodies during replication in HeLa cells. *Cell* **9**, 423-9 (1976).
9. Weintraub, H. Cooperative alignment of nu bodies during chromosome replication in the presence of cycloheximide. *Cell* **9**, 419-22 (1976).
10. Bannister, A.J. & Kouzarides, T. Regulation of chromatin by histone modifications. *Cell Res* **21**, 381-95 (2011).
11. Gasser, R., Koller, T. & Sogo, J.M. The stability of nucleosomes at the replication fork. *J Mol Biol* **258**, 224-39 (1996).
12. Herman, T.M., DePamphilis, M.L. & Wassarman, P.M. Structure of chromatin at deoxyribonucleic acid replication forks: location of the first nucleosomes on newly synthesized simian virus 40 deoxyribonucleic acid. *Biochemistry* **20**, 621-30 (1981).
13. Randall, S.K. & Kelly, T.J. The fate of parental nucleosomes during SV40 DNA replication. *J Biol Chem* **267**, 14259-65 (1992).
14. Sogo, J.M., Stahl, H., Koller, T. & Knippers, R. Structure of replicating simian virus 40 minichromosomes. The replication fork, core histone segregation and terminal structures. *J Mol Biol* **189**, 189-204 (1986).
15. Gruss, C., Wu, J., Koller, T. & Sogo, J.M. Disruption of the nucleosomes at the replication fork. *EMBO J* **12**, 4533-45 (1993).
16. Tran, V., Lim, C., Xie, J. & Chen, X. Asymmetric division of Drosophila male germline stem cell shows asymmetric histone distribution. *Science* **338**, 679-82 (2012).
17. Nakano, S., Stillman, B. & Horvitz, H.R. Replication-coupled chromatin assembly generates a neuronal bilateral asymmetry in C. elegans. *Cell* **147**, 1525-36 (2011).
18. Xie, J. et al. Histone H3 Threonine Phosphorylation Regulates Asymmetric Histone Inheritance in the Drosophila Male Germline. *Cell* **163**, 920-33 (2015).
19. Georgescu, R., Langston, L. & O'Donnell, M. A proposal: Evolution of PCNA's role as a marker of newly replicated DNA. *DNA Repair (Amst)* **29**, 4-15 (2015).

20. Sequeira-Mendes, J. et al. Transcription initiation activity sets replication origin efficiency in mammalian cells. *PLoS Genet* **5**, e1000446 (2009).
21. Anglana, M., Apiou, F., Bensimon, A. & Debatisse, M. Dynamics of DNA replication in mammalian somatic cells: Nucleotide pool modulates origin choice and interorigin spacing. *Cell* **114**, 385-394 (2003).
22. Merrikh, H., Zhang, Y., Grossman, A.D. & Wang, J.D. Replication-transcription conflicts in bacteria. *Nat Rev Microbiol* **10**, 449-58 (2012).
23. Hansen, R.S. et al. Sequencing newly replicated DNA reveals widespread plasticity in human replication timing. *Proc Natl Acad Sci U S A* **107**, 139-44 (2010).
24. Conti, C. et al. Replication fork velocities at adjacent replication origins are coordinately modified during DNA replication in human cells. *Mol Biol Cell* **18**, 3059-67 (2007).
25. Cadoret, J.C. et al. Genome-wide studies highlight indirect links between human replication origins and gene regulation. *Proc Natl Acad Sci U S A* **105**, 15837-42 (2008).
26. Hiratani, I. et al. Genome-wide dynamics of replication timing revealed by in vitro models of mouse embryogenesis. *Genome Res* **20**, 155-69 (2010).
27. Takebayashi, S. et al. Murine esBAF chromatin remodeling complex subunits BAF250a and Brg1 are necessary to maintain and reprogram pluripotency-specific replication timing of select replication domains. *Epigenetics Chromatin* **6**, 42 (2013).
28. Yeeles, J.T., Janska, A., Early, A. & Diffley, J.F. How the Eukaryotic Replisome Achieves Rapid and Efficient DNA Replication. *Mol Cell* **65**, 105-116 (2017).
29. Hodges, C., Bintu, L., Lubkowska, L., Kashlev, M. & Bustamante, C. Nucleosomal fluctuations govern the transcription dynamics of RNA polymerase II. *Science* **325**, 626-8 (2009).
30. Georgescu, R.E., Kurth, I. & O'Donnell, M.E. Single-molecule studies reveal the function of a third polymerase in the replisome. *Nat Struct Mol Biol* **19**, 113-6 (2011).
31. Zhang, Z. & Pugh, B.F. High-resolution genome-wide mapping of the primary structure of chromatin. *Cell* **144**, 175-86 (2011).
32. Brunelle, M., Rodrigue, S., Jacques, P.E. & Gevry, N. High-Resolution Genome-Wide Mapping of Nucleosome Positioning and Occupancy Level Using Paired-End Sequencing Technology. *Methods Mol Biol* **1528**, 229-243 (2017).
33. Koch, S.J., Shundrovsky, A., Jantzen, B.C. & Wang, M.D. Probing protein-DNA interactions by unzipping a single DNA double helix. *Biophys J* **83**, 1098-105 (2002).
34. Hall, M.A. et al. High-resolution dynamic mapping of histone-DNA interactions in a nucleosome. *Nat Struct Mol Biol* **16**, 124-9 (2009).
35. Ramachandran, S. & Henikoff, S. Transcriptional Regulators Compete with Nucleosomes Post-replication. *Cell* **165**, 580-92 (2016).
36. Yadav, T. & Whitehouse, I. Replication-Coupled Nucleosome Assembly and Positioning by ATP-Dependent Chromatin-Remodeling Enzymes. *Cell Rep* (2016).